



Universiteit
Leiden
The Netherlands

Insights into microtubule catastrophes: the effect of end-binding proteins and force

Kalisch, S.M.J.

Citation

Kalisch, S. M. J. (2023, December 13). *Insights into microtubule catastrophes: the effect of end-binding proteins and force*. Retrieved from <https://hdl.handle.net/1887/3673428>

Version: Publisher's Version

License: [Licence agreement concerning inclusion of doctoral thesis in the Institutional Repository of the University of Leiden](#)

Downloaded from: <https://hdl.handle.net/1887/3673428>

Note: To cite this publication please use the final published version (if applicable).

Insights into microtubule catastrophes

The effect of end-binding proteins and force

Proefschrift

ter verkrijging van
de graad van doctor aan de Universiteit Leiden,
op gezag van rector magnificus prof. dr. ir. H. Bijl,
volgens besluit van het college voor promoties
te verdedigen op woensdag 13 december 2023
klokke 12:30 uur

door

Svenja-Marei Julia Kalisch

geboren te Oldenburg (Oldb), Duitsland

Promotor:

Prof. dr. A.M. Dogterom (Technical University Delft and Leiden University)

Promotiecommissie:

Prof. dr. J. Aarts

Prof. dr. E.R. Eliel

Prof. dr. T. Schmidt

Prof. dr. G. Koenderink (Technical University Delft)

Prof. dr. E. Peterman (Free University, Amsterdam)

Prof. dr. T. Surrey (Center for Genomic Regulation, Barcelona, Spain)

© 2023 by Svenja-Marei Kalisch. All rights reserved.

Nederlandse titel: Inzichten in microtubule catastrofes. Het effect van eindbindende eiwitten en kracht.

The work described in this thesis was performed at the FOM Institute for Atomic and Molecular Physics (AMOLF) in Amsterdam, The Netherlands. This work is part of the research programme of the 'Stichting voor Fundamenteel Onderzoek der Materie' (FOM), which is financially supported by the 'Nederlandse Organisatie voor Wetenschappelijk Onderzoek' (NWO).

A digital version of this thesis can be obtained from <http://ub.leidenuniv.nl/>.

The flip book images in the footnote stem from microtubule simulations performed by Florian Huber. Those microtubules consist of black GTP/GDP-Pi-tubulin and grey GDP-tubulin (see also chapter 7).



Introduction

Each cell contains a mechanical framework vital for cellular processes such as vesicular transport and cell division. This framework, called the cytoskeleton, is very dynamic and constantly reorganises to adapt to changing cellular needs. Proper regulation is therefore crucial and is ensured partly by forces that originate from the assembly and disassembly of cytoskeletal filaments. Forces often arise from the interaction of filaments with structural components within the cell, such as the cell boundary. The rearrangement of the cell interior is further aided by the biochemical machinery directly modulating the dynamics of cytoskeletal filaments. In this thesis, we examined the dynamic regulation of one of these filaments, the microtubules. Specifically we were interested in the combined effect of force and proteins binding specifically to the microtubule's ends. For our *in vitro* experiments we used total-internal-reflection-fluorescence microscopy and a high resolution optical tweezers approach including force-feedback.

1.1 Cellular organisation

Life is very diverse. There are innumerable different organisms and until today new ones are being discovered. Yet, when looking at one organism, let's say a spider, we see a very complex creature in itself. It has glassy eyes, a fang, often soft hair, glands extruding silk and rigid legs which, due to the absence of muscles in most cases are moved by internal pressure changes [Parry and Brown, 1959, Barnes et al., 2001]. But if you think about it: the amazing part is that the spider is basically composed of one type of building block: the cell. Consequently, there must be many different types of cells, ranging from lung cells to extract oxygen, brain cells to transmit signals and photoreceptor cells to measure light intensities. Though cells have a lot of different shapes, sizes and functions, their internal organisation and structure has much in common. For example, cells comprise, among others, a nucleus containing the hereditary information in the form of DNA (the chromosomes), a cell membrane to separate and protect it from its surrounding and a scaffolding of filaments, named the cytoskeleton, to give it structure and aid internal organisation [Alberts et al., 2002].

The cytoskeleton is composed of three different types of filaments: actin filaments, intermediate filaments and microtubules (MTs). MTs are relatively stiff and are therefore well suitable to provide support to the cell. On the other hand, MTs are very dynamic filaments that can extend and reduce their length modulating their many functions. During cell

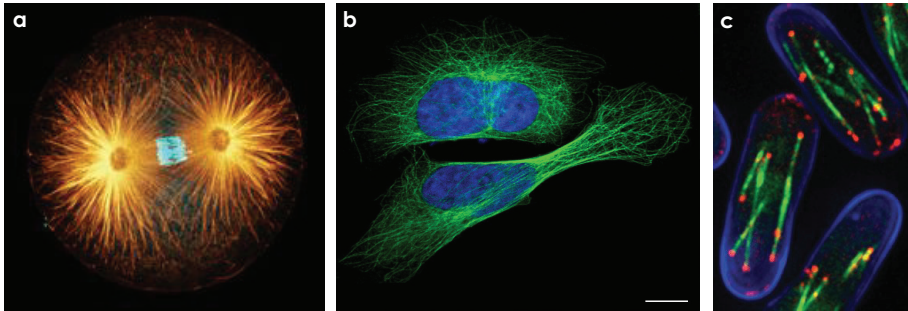


Figure 1.1: MTs in the cell. **a.** Microtubules are fixed and stained in sand dollar zygotes (urchin egg) during mitosis. The MT plus ends are connected to the chromosomes in order to pull them apart before cell division. Image obtained from [web, a]. **b.** Microtubules are stained in human cells. Scale bar represents 10 μm . Image obtained from [web, c]. **c.** The Clip-170 homologue tip1 (red) localises to the plus ends of MTs (green) in fission yeast cells (blue). Image taken from [web, b].

division, MTs originating from the centrosome (the main MT organising centre) connect to filaments at the cell cortex (actin) and to the chromosomes, see figure 1.1a. Molecular motors, attached to the cell cortex and to MTs, can then pull towards the cell periphery while other MTs assist the chromosome separation by decreasing their length [Alberts et al., 2002]. But MTs can also act as intracellular "highways". Motor proteins can walk on them or bind and rebind to move vesicles and organelles through the cell. There are motor proteins which walk from the cell centre to the periphery and others which follow the opposite direction. In non-dividing, migrating cells MTs furthermore have a key role in cellular organisation leading to directed movement. Finally, the combination of even other proteins and MTs can together form complex structures called flagella and cilia used by cells to swim [McIntosh and McDonald, 1989, Burakov et al., 2002, Vallee and Stehman, 2005, Yeaman et al., 1999, Lye and McIntosh, 1987, Vale, 1985].

All structures such as organelles, filaments, proteins and membrane compartments in the cell need space. However, cells are small and – very crowded. How is it possible that a cell can perform its task with so much precision though there is considerably little free space? The answer is: tight spatial regulation. To fulfil its various tasks, which even alter during the cell cycle, the dynamic elongation and shrinking phases by MTs and the affinity of proteins need to be carefully organised. How this functions in detail is an intriguing question and an on-going topic in research.

Also this thesis focuses on MT regulation. More specifically it looks at MT regulation by a set of proteins in combination with mechanical cues. But let us first take a closer look at MTs.

1.2 Microtubules (MTs)

1.2.1 Microtubule structure

Microtubules are composed of the protein subunit tubulin which shows little variation at the amino-acid level between different organisms. This hints at evolutionary conservation arising from important biological functions. Tubulin forms an 8 nm long dimer composed

of an α - and a β -monomer. A microtubule grows in two phases, nucleation and elongation. It usually nucleates from a template which is in cells primarily a centrosome [Kellogg et al., 1994], but can also be an axoneme and *in vitro* a short stabilised MT. Afterwards, the MT elongates by the head-to-tail association of tubulin dimers [Amos and Klug, 1974] or possibly short oligomers [Kerssemakers et al., 2006]. Tubulin assembles into the MT in linear protofilaments which bind laterally to form a hollow cylindrical tube of 25 nm diameter, as shown in figure 1.2a. Microtubules nucleated by centrosomes and axonemes have usually 13 protofilaments but in general, the protofilament number has been seen to vary between 9 to 17, even within the same microtubule [Chretien and Wade, 1991, Chretien et al., 1992]. Adjacent protofilaments are bound with a pitch of 1.5 times the length of a dimer. Therefore, neighbouring monomers follow a helical path where β - β monomers meet each other, constituting the so-called B-lattice. After one turn around the MT, due to the pitch between protofilaments, an α - is adjacent to a β -monomer, which is named the seam and forms an A-lattice structure [Mandelkow et al., 1986].

Though α - and β -monomers are similar at the amino acid level, they have structural and functional differences. This polarity of the tubulin dimer also gives rise to polarity of the MT. The microtubule grows faster at the end exposing its β -monomer (referred to as plus end). The other slower growing end, exposing its α -monomer, is called the minus end [Allen and Borisy, 1974]. In the cell, however, the minus end is usually connected to the centrosome or other nucleating structure and is therefore static. The plus end, on the other hand, can explore intracellular space. Microtubule polarity serves different functions, from giving directionality to motor proteins following the MT, to formation of protein gradients or local accumulation at MT ends [Browning et al., 2003].

Due to its architecture and relative thickness, the MT is relatively rigid. The persistence length l_p , a measure of stiffness, is in the order of millimeters and can hence span a significant fraction of the cell diameter (10-50 μm). As a result, MTs serve as a framework for the cell and can transport signals over its whole length. Note however, that the stiffness of a MT is not a universal number but can vary depending on MT lifetime and polymerisation rate (shorter and fast growing MTs are less stiff [Janson and Dogterom, 2004, Pampaloni et al., 2006]), drugs (taxol-stabilised MTs are less stiff [Felgner et al., 1996]), or microtubule-associated proteins [Mickey and Howard, 1995, Felgner et al., 1996, Felgner et al., 1997, Sandblad et al., 2006].

1.2.2 Microtubules are dynamic

MTs are dynamic structures becoming apparent by the constantly varying length over the life of a MT. By the assembly and disassembly of their subunit tubulin MTs can remain in alternating, prolonged states of slow growth and rapid shrinkage (see fig 1.2b.). The abrupt switch from the assembling to the disassembling state is called catastrophe while the reverse, more infrequent event is termed rescue [Desai and Mitchison, 1997]. This intrinsic mechanism of switching between different states, termed "dynamic instability" by Mitchison and Kirschner in 1984 [Mitchison and Kirschner, 1984a], can be described by four parameters: the growth speed (*in vitro* typically in the order of 1-5 $\mu\text{m}/\text{min}$), the shrinkage speed (approximately 10-50 $\mu\text{m}/\text{min}$), the time the MT spends in a growing state until catastrophe, the catastrophe time, and, the rescue time describing the duration of a shrinking phase until rescue. An example of these processes is presented in figure 1.2e.

As the MT never reaches a steady-state length, dynamic instability is in fact a non-equilibrium process. As such it needs to be driven which results from nucleotide

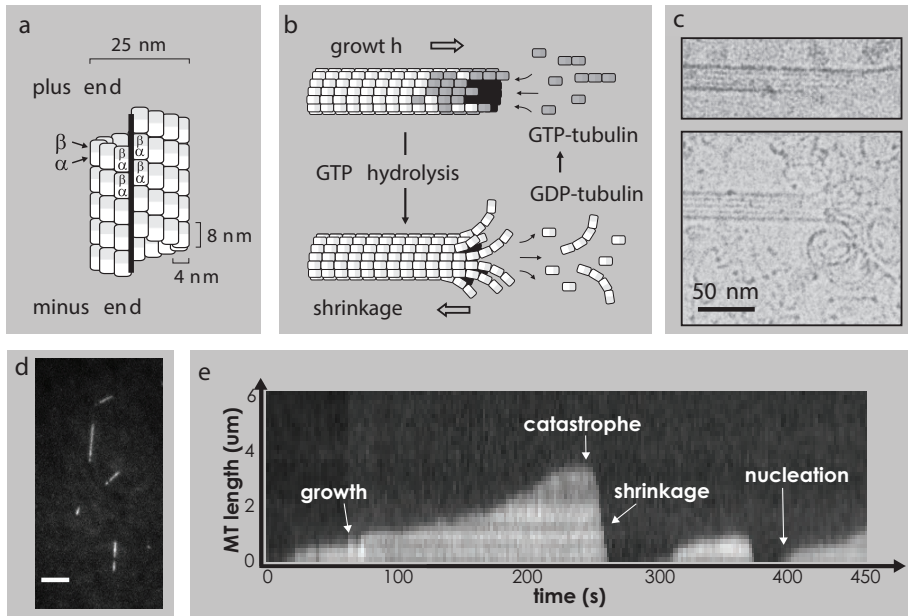


Figure 1.2: MT structure and dynamics. **a.** A MT is formed by an array of laterally bound protofilaments each composed of α - β tubulin dimers. The polarity on the dimer evokes polarity of the MT. Its ends are called plus and minus end. The major part of the MT forms a B-lattice where an α -monomer is adjacent to a β -monomer. An exception is the "seam" (indicated by the thick black line), where monomers of the same type are next to each other. **b.** MTs elongate by the addition of GTP-tubulin. In the lattice the GTP hydrolysis into GDP giving rise to mechanical strain within the lattice. Eventually, this leads to rapid de-polymerisation of the MT. In solution, the GDP is replaced by a GTP nucleotide. **c.** *top.* Electron microscopy image of a growing MT which suggests the existence of sheet-like structures which later close into a tubular shape. *below.* A shrinking MT, characterised by its protofilaments peeling off. Images adapted from [Mandelkow et al., 1991] and [Munteanu, 2008]. **d.** TIRF-M image of fluorescently labelled rhodamine-MTs. The seed, a short stabilised MT serving as nucleation template, labelled with tubulin-HiLite635 is not visible. Clearly visible are both growing plus ends and (on average shorter) minus ends. Scale bar 5 μm . **e.** A space-time plot (kymograph) of the lower MT presents "dynamic instability". MTs alternate between phases of slow growth and rapid shrinkage where the transition is called catastrophe. Before undergoing catastrophe MTs often display a stalling or slow-growth phase. The reverse transition is termed rescue (not shown) as rescues are rarely seen *in vitro*. MTs were nucleated from a seed (not shown).

hydrolysis. MTs grown in the presence of the non-hydrolysable nucleotide GMPCPP only elongate [Hyman et al., 1992] whereas MTs grown in the presence of the hydrolysable guanosine-5-triphosphate (GTP) display the typical dynamic instability pattern. Roughly this works as follows: every tubulin dimer associates to the MT with a guanosine-5-triphosphate (GTP) bound to its β -tubulin monomer [Carlier et al., 1984] (see fig 1.2b.). Once bound in the MT lattice the nucleotide hydrolyses, after a short delay, into the GDP-state. During the shrinkage phase the tubulin falls off from the MT where, in solution, the GDP is replaced by a fresh GTP nucleotide [Desai and Mitchison, 1997].

Does GTP hydrolysis have a role other than providing energy for dynamic instability? In fact, the nucleotide state of tubulin goes along with a specific tubulin conformation. GTP hydrolysis provokes a conformational change of the tubulin dimer from an almost straight to a kinked state [Wang and Nogales, 2005]. But since the GDP-dimer is constrained in the MT lattice it cannot recuperate its preferential shape. This bending energy remains therefore in the MT lattice as mechanical strain [Caplow et al., 1994]. It is only liberated when the MT shrinks, where its protofilaments peel outward in a curved fashion [Chretien et al., 1995, Mandelkow et al., 1991] which is a driving force for the rapid depolymerisation (see fig 1.2c.). The fact that the MT protofilaments hold together in a growing MT without immediate release of this energy is thought to be ensured by a MT "cap". Theoretical efforts have shown that only one to two layers of GTP-bound tubulin or even a few incomplete GTP-tubulin rings can stabilise the cap [Janosi et al., 2002, Molodtsov et al., 2005a]. However, whether such a cap is enough to prevent the MT from de-polymerisation still needs to be clarified. Another scenario for the MT cap comes from other experimental results suggesting a difference between a cap in the GTP nucleotide state than the (much larger) size of the tubulin cap mimicking a "GTP-conformational", straight state [Maurer et al., 2012] (we will come back to this in more detail in chapter 3.3, page 33).

Similarly, it is still unclear how the MT gets its tubular shape during growth. There are several models. One, derived from electron microscope images, envisions tubulin dimers to bind first longitudinally into protofilaments which then hold together to form a sheet like structure (see fig 1.2c.). This sheet would then close at the seam [Wang and Nogales, 2005, Wang et al., 2005]. Other models imagine MTs to grow as a tube where the terminal GTP-dimers' association fluctuates resulting in very dynamic and fast "growth" and "shrinkage" pattern [VanBuren et al., 2005, Schek et al., 2007, Margolin et al., 2012]. An agreement on these details is still missing.

How does the MT transition between its different dynamic states? One possibility are GTP-tubulin remnants in an otherwise GDP-lattice being thought responsible for MT rescues [Dimitrov et al., 2008]. Yet, how the MT transitions from a growing state to a period of disassembly is not clear. More specific, for long it has been questioned whether catastrophe is a stochastic process with first order kinetics. This implies that the catastrophe time is independent of the microtubule age. It also means that catastrophe is a one-step process and that events are independent. While some literature regarded catastrophes as randomly distributed and thus first-order events [Hill, 1984, Mitchison and Kirschner, 1987, Dogterom and Leibler, 1993, Flyvbjerg et al., 1994, Howard, 2001, Phillips R., 2008], others showed evidence of catastrophe being a multi-step process [Odde et al., 1995, Odde et al., 1996, Stepanova et al., 2010, Gardner et al., 2011b]. Nonetheless, all efforts so far could only suggest on the nature of the catastrophe process.

1.2.3 Microtubule catastrophes

During the last ten-odd years the view on MT catastrophes has widened without coming to a clear consensus. Originally, the "standard" GTP cap model implicates that tubulin dimers not yet hydrolyzed into a GDP state are responsible for the stability of the MT tip. Thus, it has been commonly accepted that the size of the GTP cap is an indicator for MT stability. However, recent experimental, theoretical and computational models, especially those with microtubule-associated proteins, challenge the simplicity of this model [Duellberg et al., 2016a, Duellberg et al., 2016b, Bowne-Anderson et al., 2015]. As mentioned before, a differentiation has been made between the region of EB-binding and the smaller cap necessary for stability. Researchers suggest a minimal end density threshold: for a catastrophe to occur the GTP cap has to decrease in size until the critical density is reached [Duellberg et al., 2016a]. Several catastrophe concepts have been proposed.

Many experiments have confirmed during the last years that short MTs are more stable against catastrophe than longer ones, in other words, the time a MT is growing, the MT lifetime, has an influence on its stability. This created the aforementioned concept of "MT age" and with it the idea of catastrophe being a multi-step "defect" accumulation process [Gardner et al., 2011b, Gardner et al., 2013, Bowne-Anderson et al., 2013, Coombes et al., 2013, Zakharov et al., 2015, Bowne-Anderson et al., 2015]. These defects could be the formation of cracks [Flyvbjerg et al., 1996, Li and Kolomeisky, 2014, Margolin et al., 2012] or protofilaments unable to bind new dimers. GTP tubulin from solution is thought improbable to associate to protofilaments with a terminal GDP-tubulin, thus rendering the MT instable after several such protofilaments are formed [Gardner et al., 2011b, Gardner et al., 2013].

Another concept to influence catastrophe stems from binding of tubulin dimers from solution. Not all dimers permanently attach to the MT tip, with a certain probability a portion of them dissociates after a short binding period resulting in a nanoscale irregular growth pattern [Kerssemakers et al., 2006, Schek et al., 2007, Rickman et al., 2017, Gardner et al., 2011b]. These rapid growth fluctuations create a fast turnover at the tip and can create periods of critically short MT caps [Bowne-Anderson et al., 2015, Kok et al., 2021], switching the MT into the dissociation phase. We describe this effect in detail in chapter 7 on page 79.

Finally, during growth many conformational changes take place at the MT tip. It is still not completely clear how tubulin dimers associate to the MT and thus also under debate how the MT forms a tubular shape. Further experiments have revealed the MT end to become more and more tapered while it grows. Young MTs have thus more blunt tips while older MTs tend to have longer tapered ends up to a single protofilament. With that the sites of GTP-tubulin are effectively smeared out reducing the density of binding sites in the course of the MT lifetime and thus rendering older MTs more unstable [Duellberg et al., 2016b].

1.3 Microtubule end-binding proteins (EBs)

By employing dynamic instability MTs can fulfil a variety of functions in the cell [Desai and Mitchison, 1997]. The ability to adapt appropriately and rapidly to changing cellular needs stems from a precise regulation of the dynamic instability of MTs. *In vivo* MT regulation is ensured by a variety of proteins, sometimes in combination with other cues, for example forces. In this and the following section we discuss these MT regulators in more detail.

In the cell, MT dynamics and the MT network can be regulated by the biochemical machinery. Their mechanism of action has different manifestations: it can be globally in the whole cell but it can also be a local effect. As such, MT dynamics can be modulated

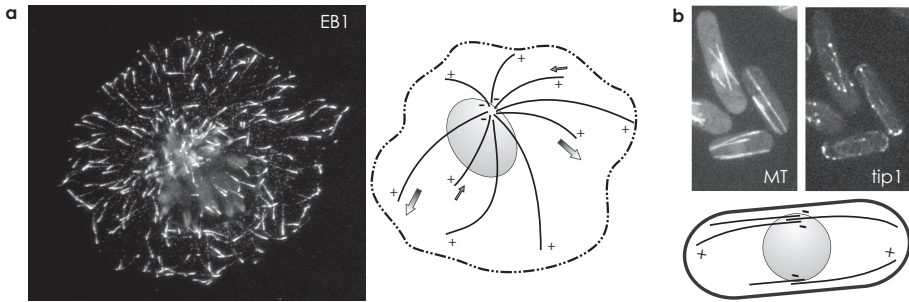


Figure 1.3: End-binding proteins in the cell. **a.** Mammalian end-binding 1 proteins (EB1) specifically bind to the growing ends of MTs in an interphase COS-7 cell. Clearly visible are the typical comets at the MT tips formed by EBs. Image courtesy of Anna Akhmanova. *right.* Schematic drawing in a comparable fibroblast cell. While the MT minus ends are connected to the nucleus the plus ends can explore intracellular space. EBs have high affinity for the growing plus ends directed towards the cell periphery. **b.** MT bundles composed of several MTs made up of tubulin-mCherry in fission yeast cells. The growing MT ends are bound by EBs, here tip1-GFP. Image courtesy of Christian Tischer. *below.* Schematic view of a fission yeast cell where the MT plus ends are growing towards the cell poles. Image taken from [Munteanu, 2008].

by MT length or age-dependent protein accumulations [Dogterom et al., 1996, Holy et al., 1997, Tischer et al., 2009], so that dynamics is different in the cytoplasm compared to at the boundaries where MTs are longer. Second, proteins can also be bound locally to intracellular structures such as the membrane and from there interact with MTs that transiently move into their vicinity [Mimori-Kiyosue et al., 2005]. A third possibility of locally regulating MT's state is the joint effort of proteins and forces which are generated when MTs grow against intracellular obstacles. We will look at MT force generation in more detail in section 1.4.

Numerous proteins binding specifically to MT ends (end-binding proteins, EBs) have been identified. Each class of proteins has specific functions, e.g. modulating the interaction of MTs with intracellular organelles (CLIP-170/CLIP150) [Perez et al., 1999, Arnal et al., 2004], stabilising MTs and attaching them to the cortex (CLASPs) [Akhmanova et al., 2001, Maiato et al., 2003, Lansbergen et al., 2006] assisting in tumor suppression in association with the MT (APC) [Mimori-Kiyosue et al., 2000]. Specifically, end-binding protein 1 (EB1), a highly conserved protein between different organisms, has been found to localise to centrosomes and to the MT ends [Mimori-Kiyosue et al., 2000, Akhmanova and Steinmetz, 2008], as shown in figure 1.3a. Importantly, it is targeting other MT-associated proteins to the MT plus end by recognising a structural SxIP-motif [Honnappa et al., 2009] and thereby modulating MT's dynamic state. As a consequence it regulates interactions with organelles, the kinetochore, the cortex and the nucleus. Due to the multitude of protein binding partners it is considered the core component of MT plus-end protein networks [Akhmanova and Steinmetz, 2008].

In fission yeast dynamic instability is mediated, among others, by the EB1-homologue mal3 [Busch and Brunner, 2004] (see fig 1.3b.). Its importance for the cell has been shown in mal3 depletion by RNA-mediated inhibition (RNAi) experiments leading to branched, bent and curved cells [Beinhauer et al., 1997]. The discovery that this was caused by very short MTs never reaching the cell poles suggested mal3 to be a prominent catastrophe regulator [Busch

and Brunner, 2004]. Another protein, closely associated with mal3 is the Clip170-homologue tip1. (An image of a fission yeast cell with fluorescent tip1 is presented in figure 1.1.c.) *In vivo* the deletion of tip1 also caused bent and branched cells and shortened MTs. Together with mal3, tip1 functions as a MT regulator suggested to prevent catastrophes at locations other than the cell poles [Brunner and Nurse, 2000a].

1.4 MTs and forces

Various experiments have shown that MTs can generate pulling and pushing forces [Dogterom and Yurke, 1997, Grishchuk et al., 2005]. Pulling forces can be created when a protein binds to the shrinking MT end and an intracellular structure. While the MT end is retracting, the protein, stationary located, pulls on its binding partner, thereby performing mechanical work [Inoue and Salmon, 1995, Dogterom et al., 2005]. This is for example the case in mitosis when proteins connect the MT end to the kinetochore of chromosomes [Maito et al., 2004]. Pushing forces, on the other hand, are used for positioning processes. There are many examples: placement of microtubule organising centres and organelles [Tran et al., 2001] or the central alignment of the nucleus [Tran et al., 2001, Foethke et al., 2009] or the spindle [Tolic-Norrelykke et al., 2004, Vogel et al., 2007] by microtubules pushing against the cell boundary. The interest in MT force generation and its diversity is shown by the variety of published experimental and theoretical work [Inoue and Salmon, 1995, Dogterom and Yurke, 1997, Mogilner and Oster, 1999, van Doorn et al., 2000, Stukalin and Kolomeisky, 2004, Janson et al., 2003, Janson and Dogterom, 2004]. Since this thesis deals specifically with pushing forces we want to give more insight into this topic in the following section.

How does a statically located filament generate a pushing force? First, thermodynamic calculations show that tubulin association to the MT gives rise to enough energy to create a significant force [Hill and Kirschner, 1982, Hill, 1987, van Doorn et al., 2000]. (This is a different energy than the one derived from GTP hydrolysis, which was explained above. GTP hydrolysis creates internal mechanical strain and is the driving force for rapid depolymerisation and pulling forces.) Further, a mechanistic way of force generation is given by the Brownian ratchet model [Peskin et al., 1993, Mogilner and Oster, 1999]. As presented in figure 1.4 the simplest model imagines the MT as a linear arrangement of tubulin dimers in contact with a mobile barrier. Though most of the time the MT is in close contact with the barrier, thermal fluctuations of the MT and the barrier occasionally open a small gap. If the space is transiently large enough a new tubulin dimer can be incorporated. As now the barrier cannot move back to its original position it is translated by the length of the dimer, resulting in work being performed. Since the space between barrier and MT end to insert a new tubulin dimer appears less often with increasing force, the MT reduces its growth speed. Therefore the Brownian ratchet model can explain the decaying force - growth speed relationship as shown in chapter 6 and [Dogterom and Yurke, 1997, Janson et al., 2003]. The compressive force experienced by the MT results in slight compression of the filament. When the barrier is static as is the case in our *in vitro* experiments, the applied force comes from MT compression only.

If MTs are long enough they can release the compressive force by buckling (the mechanism of buckling is presented in fig. 3.2c). A condition for buckling is the compressive force to overcome the critical buckling force $F_c \cong 20.19 \kappa L^{-2}$, where κ is the flexural rigidity and L the MT length [Gittes et al., 1996] assuming the nucleation site is clamped (i.e. not pivoting). Using the typical value for $\kappa=25 \text{ pN}\mu\text{m}^2$, a MT of length $1 \mu\text{m}$ will buckle at a force of $\sim 500 \text{ pN}$ while a MT longer than $20 \mu\text{m}$ needs only $\sim 1 \text{ pN}$.

If the MTs are too short to buckle they will eventually stop growth. The force necessary to

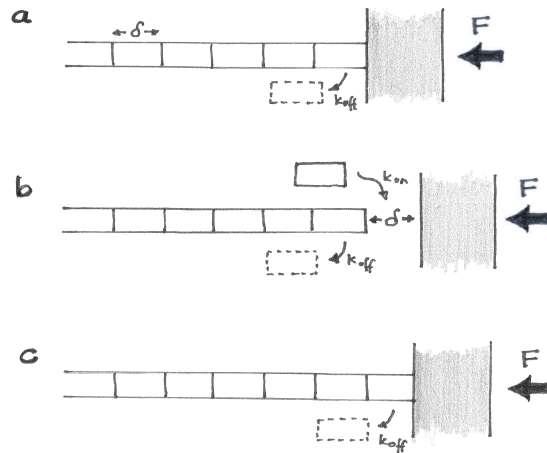


Figure 1.4: The Brownian ratchet model explains MT force generation. **a.** Schematic view of a "MT" just reaching a barrier to which a compressive force F is applied. **b.** Thermal motion creates transient gaps between the barrier and the MT end. If such a gap is large enough a tubulin dimer of length δ can bind to the MT end with rate k_{on} . **c.** The insertion of the tubulin dimer moved the barrier a distance δ and thus performed work. At all times a tubulin dimer can disassociate from the MT with rate k_{off} . Image adapted from [Dogterom et al., 2002].

prevent the new incorporation of tubulin subunits where only occasionally a dimer detaches from the MT is termed "stall force".

1.5 Thesis layout

Despite the wealth of experimental and theoretical information, it is not yet clear what is the combined effect of end-binding proteins (EBs) and forces on MT dynamics. The scope of this thesis is to obtain a more detailed understanding of the catastrophe process and the accompanying role of EBs and forces. We set out to tackle this problem with *in vitro* experiments. What the specific research questions are, how we approach them, and what insights we gain is shown below:

Chapter 2: Methods

- How do we create flow chambers with embedded micro-fabricated barriers to study the interaction of dynamic MTs with physical structures?
- How are the assays prepared?
- Describing the TIRF and optical tweezers setup

Chapter 3: Fluorescence intensity measurements of the end-binding protein mal3

why?

- How is the binding of mal3 to the MT end related to catastrophe?
- What influence do head-on forces have on this?

how?

- TIRF-M experiments of fluorescently labelled rhodamine-tubulin MTs and mal3-Alexa488.
- MTs interacting with micro-fabricated barriers.

what?

- Mal3 starts unbinding from the MTs on the order of 10 s before catastrophe.
- Barrier contact induces the loss of mal3 within an average of 10 s.

Chapter 4: The catastrophe process of free MTs

why?

- What is the nature of the catastrophe process?
- How is this process influenced by mal3 and the protein complex mal3-tea2-tip1?

how?

- TIRF-M experiments of MTs and EBs.
- Fit catastrophe times to several models and compare to simulations.

what?

- In the absence of EBs catastrophe is a two-step process.
- Before catastrophe mal3 starts unbinding from the MT.

Chapter 5: The catastrophe process of MTs under force

why?

- How is the catastrophe process in the absence and presence of EBs affected by head-on forces?

how?

- TIRF-M experiments of MTs and EBs with microfabricated barriers.
- Fit barrier-contact times of MTs having a catastrophe at a barrier with several distributions.

what?

- The catastrophe process is a multi-step process in the absence of EBs.
- The presence of EBs renders MTs under force a one-step process.

Chapter 6: Force velocity relationship of MTs with EBs

why?

- What is the force-velocity relationship of growing MTs under force, in the presence of EBs?

how?

- Measure polymerization dynamics of MTs with optical tweezers with force-feedback.

what?

- The effect of EBs on MT growth is limited by forces. For forces above 0.5 pN we cannot determine substantial influence on growth by EBs.

Chapter 7: EB3-informed dynamics of the MT cap during stalled growth

why?

- How do EBs inform MT dynamics during stalled growth?

how?

- TIRF-M experiments of MTs and EB3 growing against microfabricated barriers with an overhang.
- Monte Carlo Simulations of 1D MTs during growth and stalling.

what?

- Noisy growth, a single EB3-dependent hydrolysis rate and a density of GTP dimers at the MT tip are enough to reproduce a range of experimental outcomes.

Chapter 8: Discussion and outlook

- Remarks on catastrophe-describing distributions, other than the ones presented in chapter 4.
- Different concepts of MT catastrophe.
- Preliminary results of correlated dynamics at MT ends of mal3 and tip1.
- Possible additional research directions.

Micro-fabrication, sample preparation and imaging methods



Authors: Kalisch SMJ, Laan L, and Dogterom M

This chapter focuses on methods to study force generation by, and regulation of microtubules (MTs) that interact with growth-opposing barriers. We describe two *in vitro* assays that can be used to mimic MT interactions with the cell boundary. The essential components in each of our minimal systems are (functionalised) micro-fabricated barriers against which we grow MTs under different conditions. We describe in detail the different methods and assays necessary to realise these *in vitro* experiments.

2.1 Introduction

Microtubules (MTs) play an important role in cellular organisation. Through interactions with the cell's cortex pushing and/or pulling forces are generated that position various organelles in the cell [Adames and Cooper, 2000, Dogterom et al., 2005, Tolic-Norrelykke et al., 2005, Tran et al., 2001] or physically segregate the chromosomes in dividing cells. MTs are dynamic structures, possessing a property called "dynamic instability" [Mitchison and Kirschner, 1984a, Desai and Mitchison, 1997]. It refers to the intrinsic ability of MTs to rapidly switch between a growing and a shrinking state, events that are termed catastrophes and rescues [Fygenson et al., 1994]. *In vitro* the parameters of dynamic instability can be regulated by temperature or tubulin concentration [Gadde and Heald, 2004], but a cell cannot easily manipulate these parameters on a short time scale. Nevertheless, in cells the dynamic instability parameters are quite variable and different from *in vitro* experiments [Bieling et al., 2008]. Over the years it has become clear that cells exploit a large variety of proteins to regulate the parameters of dynamic instability both globally and locally to properly organise the MT cytoskeleton. Many studies have been published which describe the regulation of MT dynamics by MT associated proteins *in vitro* and *in vivo* [Bieling et al., 2007, Brouhard et al., 2008, Dixit et al., 2009, Honnappa et al., 2009, Kinoshita et al., 2001, Kinoshita et al., 2002, Komarova et al., 2009, Dogterom and Yurke, 1997]. On the other hand, the cell can also physically regulate MT dynamics. Several *in vitro* studies using micro-fabricated barriers have directly shown that forces regulate MT dynamics [Fygenson et al., 1997, Janson, 2002, Janson and Dogterom, 2004, Kerssemakers et al., 2003].

In order to understand the combined effect of force and microtubule associated proteins on MT dynamics carefully designed (*in vitro*) assays are necessary. Here we present two versions. In section 2.2 we study the global effect of proteins onto MTs under force using

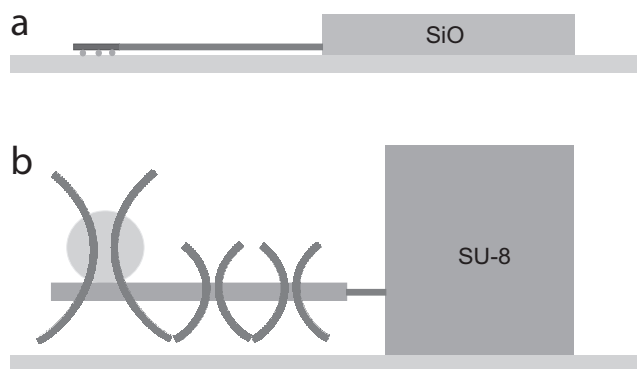


Figure 2.1: Cartoons of assays exploiting micro-fabricated structures (side views). **a.** MTs growing from stabilised MT seeds against glass (SiO) barriers. **b.** Axoneme-bead construct in an optical trap positioned against a barrier of SU-8 photo resist.

total-internal reflection fluorescence microscopy (TIRF). MTs grow against rigid glass barriers in the presence of freely floating end-binding proteins (EBs), a subclass of microtubule associated proteins only attaching to MT ends. In section 2.3 we explain an assay using an optical trap [Kerssemakers et al., 2006, Finer et al., 1994] which allows us to measure the magnitude of generated forces while EBs are present. Yet, this setup restricts us to the study of MT polymerisation under increasing force conditions. To get a more complete picture of MT force generation in the presence of EBs and the consequent regulation of MT dynamics by force the exertion of constant forces becomes necessary. We consequently extended our optical tweezers setup with a force-feedback algorithm [Simmons et al., 1996, Visscher et al., 1999, Schek et al., 2007, Moudjou and Bornens, 1994].

2.2 TIRF experiments

To study the effect of force on MT dynamics we use *glass barriers*. Optionally, end-binding proteins [Howard and Hyman, 2007] can be added to determine the combined effect of protein regulation and force. Glass barriers have the advantage of being transparent for light microscopy, being rigid to mimic bacterial cell walls, and can be blocked by standard microscope slide surface blocking protocols. Dynamic MTs are grown from surface-attached stabilised MT seeds (see 2.2.2) [Dogterom and Yurke, 1997, Janson et al., 2003]. These dynamic microtubules do not adhere to the glass surface and undergo dynamic instability. Since the seeds are randomly positioned only some microtubules reach the micro-fabricated barriers and, while keeping to grow, exert pushing forces (fig. 2.1).

2.2.1 Fabrication of glass barriers

Glass barriers are made of silicon monoxide (SiO) as follows (see also figure 2.2):

1. Clean coverslips in base piranha. Rinse them 3x with MilliQ and blow-dry. Coat them with $\sim 1.5 \mu\text{m}$ SiO under vacuum at evaporation rates of 2 \AA/s . Evaporation of SiO should not exceed rates of a few nm/s to prevent formation of big glass granules and to

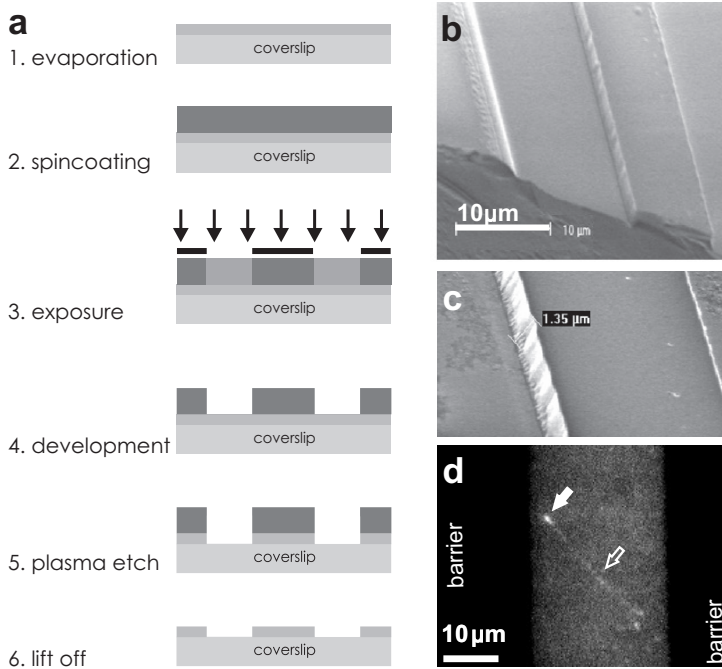


Figure 2.2: Fabrication process of glass barriers. **a.** Steps taken in the fabrication process as explained in the text. **b.** A low magnification scanning electron microscope (SEM) image of the glass-barriers. **c.** Higher magnification SEM image of the glass barriers with $\sim 1.5 \mu\text{m}$ height. **d.** Total internal reflection fluorescence (TIRF) image of fluorescently-labelled end-binding proteins tracking a MT +end (white arrow). The MT is grown from a stabilised seed (open arrow).

avoid strain on the evaporation machinery. We determine the thickness of evaporated material with a sensor in the vacuum chamber.

2. Evaporate the samples with hexamethyldisilazane (HMDS): pour $\sim 5\text{ml}$ HDMS into a glass beaker. Place it together with the samples into a desiccator for approx. 10 minutes. The HDMS forms a thin layer on the SiO to improve the adhesion of the next layer of photo resist.
3. Spin-coat S1813 photo resist on top for approx. 40 s at 1000 rpm. Soft-bake each slide at 115°C for 90 s on a hot plate.
4. Expose the slides to UV light through a chromium mask for 12 s. If the contact between sample and mask is not tight enough scattered UV-light exposes also part of the barrier resulting in slanted walls. Therefore ensure that the mask firmly touches the S1813 coating. Likewise, reflections from the sample holder below the coverslip can result in uneven barrier walls. We avoid this by placing the coverslip on black paper.
5. Post-exposure bake at 130°C for 30 minutes.
6. Develop the slides by swishing them in MF319 developer for one minute. Rinse them afterwards in MilliQ water and blow-dry with N_2 .

7. Plasma-etch the coverslips in a mixture of a CHF_3 -/ SF_6 -/Argon- plasma. We aim to etch through the evaporated layer of SiO ($1.5 \mu\text{m}$ high) which takes one hour. To remove possible contamination of the plasma on the glass, end the process with 15 minutes of exposure to oxygen plasma.
8. Remove the remaining photo resist by sonication in acetone for 5 minutes.

2.2.2 Assay of MTs growing against glass barriers

With the glass barriers we test the influence of microtubule pushing forces on MT dynamics [Fygenson et al., 1997, Kerssemakers et al., 2003]. For this assay the glass barriers need to be high ($\sim 1.5 \mu\text{m}$) and straight enough to prevent MTs from growing over them.

1. First, construct a flow cell by drawing two parallel lines of vacuum grease 4 mm apart on a clean microscope slide. Mount a coverslip containing barriers on top. This forms a cavity, with the microscope slide and the coverslip forming the bottom and top and the two grease lines the side walls. The open sides are used as inlet and outlet. To ensure a well defined volume flow in $7 \mu\text{l}$ of solution (here PLL-PEG-biotin, see below) and press the coverslip evenly down.
2. In between each of the following incubation steps rinse the sample with twice the flow cell volume of MRB80 by applying the solution at the inlet and at the same time absorbing solution with a filter paper at the outlet of the flow cell.
3. Block the glass surfaces with 0.2 mg/ml PLL-PEG-biotin by introducing it into the flow cell and incubating upside-down for 5 minutes. Rinse with $100 \mu\text{l}$ of MRB80. Form another blocking layer by incubation with 1 mg/ml κ -casein.
4. Activate the surface with a streptavidin mix (1 mg/ml streptavidin, 1 mg/ml κ -casein). Incubate the stabilised MT seeds for 5 minutes upside-down to let them adhere specifically via the streptavidin-biotin linkers.
5. Finally, introduce the tubulin mix and seal the chamber with valap.

2.2.3 TIRF setup

The sample was imaged in an inverted Ti-Nikon Eclipse microscope (Nikon, Tokyo, Japan) using total internal reflection fluorescence (TIRF) microscopy equipped with a 1.49 NA, 100x oil immersion objective. Single tiff-images were recorded using a Calypso 491 nm diode laser (Cobolt, Solna, Sweden), a Jive 561 nm diode laser (Cobolt) and a 635 nm "56 RCS-004" diode laser (Melles Griot, Albuquerque, NM, USA) imaged with a Roper Scientific Coolsnap HQ CCD-camera (Photometrics, Tucson, AZ, USA) and saved to disk with MetaMorph software (Molecular Devices, Sunnyvale, CA, USA), at frame rates between 0.2 and 5 s, at typical exposure times of 200-250 ms. After mounting the sample on the microscope stage imaging started after a 5 minute equilibration time. Imaging time was kept below 2 hours (average of 1 hour) at a constant temperature of $25 \pm 0.5^\circ\text{C}$ which was maintained by running heated/cooled water through a sleeve around the objective. Simultaneously, the water temperature was adjusted by Peltier elements to a temperature based on a sensor within the sleeve in proximity to the sample.

2.3 Optical trap experiments

Figure 2.1c shows a cartoon of a $7 \mu\text{m}$ -high *SU-8 barrier* used in optical trap experiments. In this experiment MT dynamics, as well as MT-based pushing and pulling forces can be

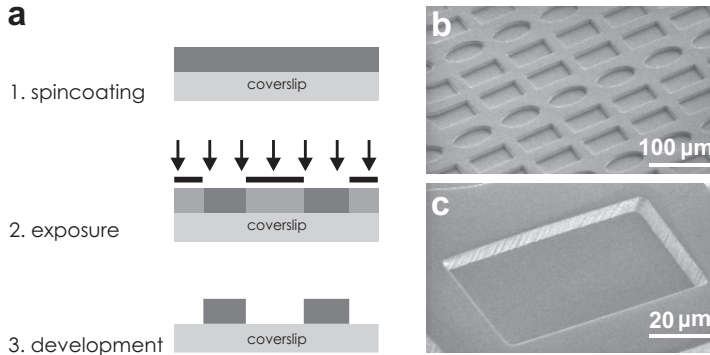


Figure 2.3: Fabrication process of SU-8 chambers. **a.** Steps taken in the fabrication process as explained in the text. **b.** A low magnification scanning electron microscope (SEM) image of the SU-8 chambers. **c.** Higher magnification SEM image of the SU-8 chambers.

measured [Kerssemakers et al., 2003, Kerssemakers et al., 2006, Laan et al., 2012]. MTs are grown from an axoneme attached to an optically trapped bead against a SU-8 photo resist barrier [Schek and Hunt, 2005].

2.3.1 Micro-fabricated barriers for optical trap experiments

To allow space for the trapped bead, and to minimise near-surface viscosity effects [Gittes and Schmidt, 1998] the barriers need to be high enough. The bead-axoneme construct is positioned approximately 4 bead radii ($\sim 4 \mu\text{m}$) above the bottom surface with an additional $3 \mu\text{m}$ barrier above to prevent the microtubules from growing over. We produce $7 \mu\text{m}$ high chambers of 40 by $80 \mu\text{m}$ separated by $20 \mu\text{m}$ -wide interspacers (fig. 2.3):

1. Spin-coat clean coverslips with SU-8 negative tone photoresist to produce a $7 \mu\text{m}$ -thick layer. We spin-coat 25 seconds at 1000 rpm. Softbake the slides 2 minutes at 65°C on a hot plate, then 2 minutes at 95°C .
2. Expose the coverslips with UV light through a mask. The mask contains the pattern to be transferred to the SU-8. We additionally use a Schott BG12 filter and expose for 32 s.
3. Post-exposure bake the samples one minute at 65°C and subsequently 2 minutes at 95°C .
4. Develop the coverslips with SU-8 developer by swishing them consecutively in three beakers:
 - developer: 90 seconds
 - developer to rinse: 20 seconds
 - 2-propanol to rinse
5. Blow-dry with N_2 and hardbake 10 minutes at 160°C on a hot plate.

2.3.2 Preparation of a flow cell

Experiments with optical tweezers offer high resolution and are therefore ideal for determination of molecular details. Moreover, with these experiments we can examine and exert pushing and pulling forces. The flow chamber is prepared as described below:

1. First, build a flow cell: glue a piece of parafilm onto a microscope slide by heating both on a hot plate. Cut a channel into the parafilm and stick a clean coverslip with micro-fabricated SU-8 chambers over the channel. Leave one side of the channel open to allow injection of solutions during the experiment. With more parafilm glue a piece of teflon tubing to the other end of the channel. The height of the tubing's end relative to the height of the flow cell's inlet determines the flow speed inside the flow cell and gives an easy and fast way to adjust the flow speed to the experiment.
2. Since proteins tend to non-specifically adhere to SU-8 the surfaces of the flow cell have to be blocked thoroughly. Start with flowing in a solution of 0.2 % agarose at 70°C. Pump out the agarose immediately by connecting a pump to the channel for a few minutes. Blocking the SU-8 flow cell surfaces can be enhanced by repeating the agarose incubation step.
3. Flow a 0.01 % Triton X-100 solution to prevent bubble formation in the flow cell. To reach constant and reproducible flow speeds it is important that the flow cell does not contain even tiny air bubbles. Flowing 0.01 % Triton X100 removes air bubbles and makes the flow cell's surfaces hydrophilic for MRB80 buffer.
4. Do a second blocking step by incubating the flow cell for 10 minutes with 0.1 mg/ml κ -casein.
5. Finally, rinse the flow cell with 100 μ l of MRB80. Degas the buffer before use by sonicating for five minutes. It reduces formation of air bubbles within the chamber.

2.3.3 Optical trap setup

The optical trap setup [Ashkin, 1970, Svoboda and Block, 1994] consists of an infrared trapping laser (1064 nm, Nd:YVO₄, Spectra-Physics, Irvine, CA, USA), which is focused into the sample by a 100x /1.3 NA oil immersion objective. The laser beam is time-shared using acousto-optical deflectors (AODs) (DTD-274HA6, IntraAction, Bellwood, IL, USA) to create a "key hole" trap consisting of a point trap and a line trap, as previously described [Kerssemakers et al., 2006, Finer et al., 1994]. A low-power red HeNe-laser with 633 nm wavelength (1125P, Uniphase, Barrington, NJ, USA) is superimposed after the AODs on the IR beam. Before or after every experiment, the red laser light is focused on a bead trapped in the point trap, and imaged onto a quadrant-photodiode for stiffness calibration. The stiffness of the point trap is then determined by analysis of the power-spectrum of the thermal fluctuations of the bead. Typically, trap stiffnesses in the range of 0.03-0.12 pN/nm are used.

2.3.4 Performing the experiments

To measure force generation during MT growth an bead-axoneme construct is assembled, positioned against a micro-fabricated barrier, and MT growth initiated by addition of tubulin to the buffer:

1. Flow axonemes and beads into the flow cell. First trap a bead in the point trap. Then locate a suitable axoneme. Later during the experiment the axoneme tip has to be at least 1 μ m away from the line trap to avoid light-induced MT depolymerisation.

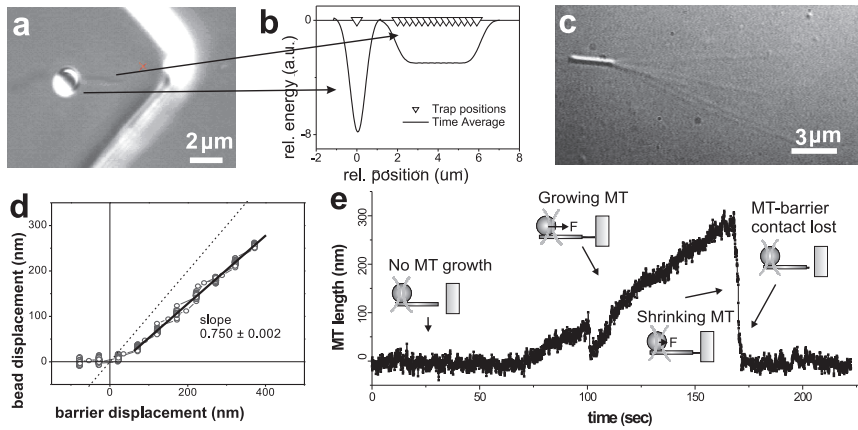


Figure 2.4: The optical trap experiment. **a.** Video-enhanced differential interference contrast (VE-DIC) image of a construct consisting of a bead, held in the optical trap, connected to an axoneme, positioned in front of a barrier. **b.** Time-shared laser position (open triangles) and potential well of the key-hole shaped optical trap. **c.** VE-DIC image of MTs growing from an axoneme. The number of MTs growing from the axoneme can be controlled by varying the tubulin concentration and the temperature [Laan et al., 2008]. **d.** Stiffness determination of the axoneme-bead construct. The wall displacement is plotted against the bead displacement. The axoneme-bead construct shows an initial soft regime of approximately 50 nm, followed by a linear regime. **e.** Graph with a typical dataset of MT length against time. Cartoons insets show the bead position relative to the trap position for different phases of the experiment.

Yet, too long axonemes are not as stably trapped and can move out of the line trap during MT growth. Axonemes with length of 4-6 μm are therefore ideal. To "catch" the axoneme move the bead close to it which will non-specifically attach both. Bring the axoneme into the line trap [Finer et al., 1994] and position this bead-axoneme construct in front of a barrier in one of the micro-fabricated chambers (fig. 2.4a-c).

2. The optical tweezers experiment is performed with the axoneme tip relatively close to the barrier to keep the MTs short (less than one μm). As the force necessary to buckle these short MTs is much higher than the force that is maximally applied with the optical trap we can exclude MT buckling. Furthermore, the MTs are forced to stay in 'end-on' contact with the barrier during the experiment.
3. Because the axoneme-bead construct is not infinitely stiff, the bead moves out of the trap centre a smaller distance than the MT grows. Since we measure the bead displacement and deduct from it the MT length change, we need to know the conversion factor between bead and MT tip displacement.
4. Therefore, measure this conversion factor by repeatedly pushing the barrier against the bead-axoneme construct and plot the subsequent bead displacement as a function of barrier displacement. As an example refer to Figure 5D, where after a first soft regime of approximately 50 nm, the conversion factor is constant over several hundreds of nanometers [Finer et al., 1994].

5. Rinse the chamber with MRB80 at high flow speed to remove left-over beads and axonemes. Avoid the loss of the trapped construct due to viscous drag by hiding it in the "lee" of a micro-fabricated barrier.
6. Trapping of a second bead can distort the signal or knock the construct out of the trap. Avoid this by staying close to the bottom surface.
7. Position the tip of the axoneme approximately 100 nm away from the barrier and add the tubulin mix (variable tubulin concentration, 1 mM GTP, 0.1 mg/ml κ -casein in MRB80) to trigger MT growth.
8. The flow speed has to be carefully adjusted such the tubulin mix really reach the bottom of the flow cell. When flow speeds are too high chemicals are flown out before they have diffused to the construct. Besides, it makes the experiment reproducible.
9. Figure 2.4e shows a typical dataset of MT growth. Initially there is no MT growth so that the bead is positioned in the centre of the point trap. Then the MT starts to grow and pushes the bead out of the trap centre. Eventually the MT undergoes a catastrophe, and while the MT shrinks the bead moves back to the trap centre.
10. We image axonemes and beads using VE-DIC microscopy. During the experiments, the image stream is digitised at 1 Hz and the position of the bead tracked online using a home-written cross-correlation routine for live monitoring. Afterwards, the recorded images are digitised at a frame rate of 25 Hz. This image stream is used to track the bead offline. The bead tracking is automated using home-written IDL software. The position of the bead is obtained with a sub-pixel resolution of 2-3 nm [Laan et al., 2008].
11. We could distinguish between plus- and minus-end growth because the plus-end is known to grow faster and to have more catastrophes [Fyngenson et al., 1994]. Occasionally we obtained measurements with much slower growth and no catastrophes, which we attributed to minus-ends.

2.3.5 Optical tweezers with force-feedback

With our optical tweezers setup we trap a bead which in turn is adhered to an axoneme. While its tip is pointing towards the SU-8 barriers also the MTs grow against it pushing the attached bead out of the trap centre. The restoring force of the trap pushes the bead back resulting in an increasing force on the MT. However, to elucidate the effect of force on MT dynamics it is more convenient to work with constant forces. This can be achieved with a force-feedback algorithm [Simmons et al., 1996, Visscher et al., 1999, Schek et al., 2007, Moudjou and Bornens, 1994] such that upon displacement of the bead from the trap centre the force-feedback algorithm reduces the force onto the MT by mechanically increasing the space between trap centre and barrier (fig. 2.5). In our setup this is achieved by translating the microscope stage, and with it the sample containing the barriers.

Before starting the algorithm the user defines a "reference point" which specifies the desired bead position relative to the trap centre. This relative distance defines the magnitude of the constant force and can be freely chosen. During an experiment with force-feedback the bead position is constantly monitored. This is achieved by focusing the red laser light on the bead trapped in the point trap and imaging it onto the quadrant-photodiode (QPD) as described in 2.3.3. The force-feedback algorithm compares the actual bead position calculated from the QPD signal to the reference point. If the bead is not at the reference point then the software directs the piezo actuators of the microscope stage to move until the bead is located there. The software is written in LabView (National Instruments, Austin, TX, USA)

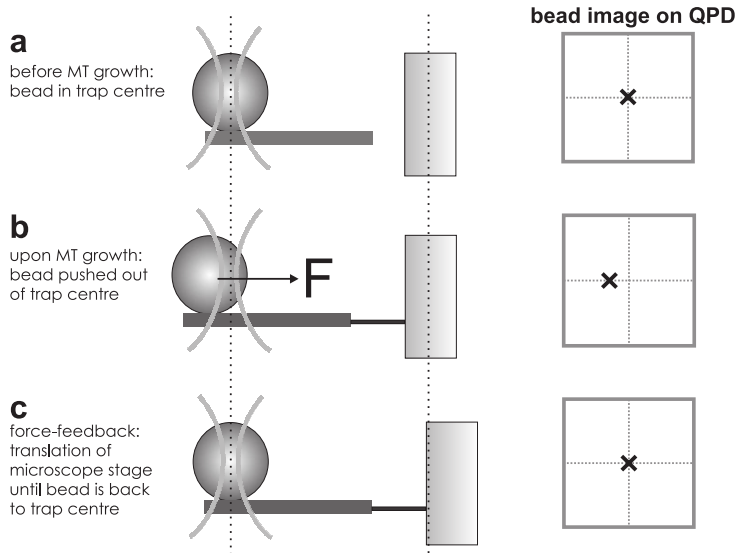


Figure 2.5: Optical tweezers with force-feedback. **a.** MT did not start growing, the bead is at the chosen starting point. **b.** Growing MT, the bead is pushed out of the trap centre. This is measured on the QPD. **c.** The force-feedback algorithm directs the microscope stage to move such that relative distance between the trap centre and the barrier increases so that the bead is back at its starting position.

and functions with a 10 Hz iteration rate, which is fast enough to track MTs growing with typical speeds of 1-5 $\mu\text{m}/\text{min}$.

After making the construct and determining the conversion factor between MT tip displacement and bead displacement (see 2.3.4) the experiment with force-feedback proceeds:

1. When working with QPD position detection (see 3.3.4.) it is best to start the experiment with the image in the centre of the QPD to stay within the linear regime of the QPD. Similarly, take into account that the piezo stage needs space to react.
2. Relate the QPD signal in volts to a signal in nanometers. For this move the trapped construct a known distance (e.g. 100 nm) by translating the laser trap. Plot the subsequent trap displacement as a function of QPD read-off. From a fit to the resulting line get the calibration factor.
3. Perform a trap stiffness calibration. This relates the QPD signal calibrated in nanometers to a force.
4. Choose the reference point by positioning the construct at the desired position.
5. Perform the experiment as described before 2.3.3. Note that due to the repositioning of the stage, MT growth does not result in bead displacement. Instead, MT growth or force can be obtained from the stage position.

Acknowledgements and further information

We thank Chris Rétif for his advice on micro-fabrication, Henk Bar for his help with micro-fabrication, Jacob W. J. Kerssemakers, E. Laura Munteanu, and Julien Husson for developing

and helping with the optical trap assay, Matt Footer (J. Theriot laboratory) for the axoneme purification. Financial support from "Human Frontiers Science Program" and "Marie Curie Early Stage Training" is gratefully acknowledged. This work is part of the research program of the "Stichting voor Fundamenteel Onderzoek der Materie (FOM)", which is financially supported by the "Nederlandse Organisatie voor Wetenschappelijk Onderzoek (NWO)".

This chapter was published in *Methods in Molecular Biology*, Springer Protocols [Kalisch et al., 2011].

Binding dynamics of the end-binding protein mal3

The dynamics of microtubules are essential for cell morphogenesis, intracellular motility and organisation processes and structuring organelles. Microtubule ends can alternate between periods of growth and shortening, processes modulated by end-binding proteins. Of special interest is the dynamics and mechanism of microtubule catastrophes, the transition from growth to shortening. To gain further insight into this process we study the binding dynamics of the fission yeast end-binding protein mal3 during microtubule catastrophes. Using total internal reflection fluorescence microscopy we confirm that mal3 binding to the microtubule starts decreasing, on average, several seconds before catastrophe. Since microtubule dynamics is also regulated by forces we compare our results to experiments where microtubules grow against rigid barriers in the presence of mal3. Here, we observe the loss of mal3 upon build-up of force. We explain our results with mal3's affinity for a specific nucleotide state of tubulin. Before catastrophe and under force this nucleotide state is altered leading to the loss of mal3 binding sites.

3.1 Introduction

Microtubules (MTs) are polar dynamic filaments essential for many cellular processes like cell growth, motility and division. Extension and shortening of MTs can generate pushing and pulling forces [Janson et al., 2003, Janson and Dogterom, 2004], deliver proteins to various destinations in the cell and allows microtubules to search intracellular space [Holy and Leibler, 1994].

MTs primarily turn over by the addition or loss of tubulin subunits at their ends. This leads to a behaviour called "dynamic instability" [Mitchison and Kirschner, 1984a, Mitchison and Kirschner, 1984b] where periods of MT growth transition to periods of rapid shortening. This switching is termed "catastrophe" whereas the transition back from disassembly to assembly is termed "rescue".

The cell can regulate MT dynamics in at least two different ways. One of them is the biochemical machinery consisting of, among others, proteins associating specifically with MT ends (end-binding proteins). End-binding 1 (EB1) protein, a highly conserved protein between different organisms, has been found to localise to centrosomes and to MT ends [Mimori-Kiyosue et al., 2000, Akhmanova and Steinmetz, 2008]. Further, it is targeting other MT-associated proteins to the MT plus end, thereby modulating MT's dynamic state. Due to the multitude of protein binding partners it is considered the core component of MT plus-end protein networks [Komarova et al., 2009]. In fission yeast dynamic instability

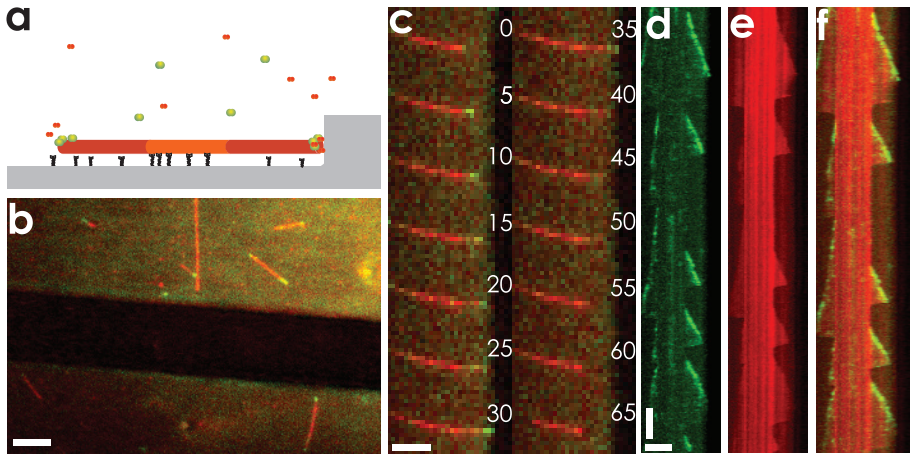


Figure 3.1: Assay of dynamic MTs in the presence of the end-binding protein mal3 and a force. **a.** Schematic setup: dynamic MTs (red) grow from stabilised surface-attached seeds (orange) against micro-fabricated barriers (grey) in the presence of the end-binding protein mal3-alexa488 (green). **b.** TIRF-image of rhodamine-tubulin MTs (red) and mal3-alexa488 (green). The black bar is the barrier imaged from the top. Scale bar is 4 μm . **c.** Time series of the lower right MT; numbers refer to the elapsed time in seconds. The MT reaches the barrier after 10 s, slides along the barrier, switches to shrinkage after 50 s and shrinks back to the seed. Scale bar shows 2 μm . **d.** Mal3-Alexa488 (green), **e.** rhodamine-tubulin (red) and **f.** colour-merge kymographs of the same MT. Horizontal scale bar is 4 μm , while the vertical one is 50 s.

is affected, among others, by the EB1-homologue mal3 [Busch and Brunner, 2004] which has been shown to increase microtubule growth speed and reduce the duration of the growing phase [Beinhauer et al., 1997, Brunner and Nurse, 2000b, Brunner and Nurse, 2000a, Tirnauer et al., 2002, Busch and Brunner, 2004, Bieling et al., 2007, Vitre et al., 2008]. It is therefore a prominent regulator of microtubule catastrophes.

Another way to regulate MT dynamics is by internal forces. The MT itself can generate pushing and pulling forces by assembling or disassembling while connecting to intracellular structures. On the other hand, the MT can also become subject to forces by motor proteins [Browning et al., 2003]. That forces influence dynamic instability has been predicted theoretically earlier and shown by *in vitro* microscopy experiments. MTs grown against glass barriers experience a compressive force which decreases their growth speed [Janson and Dogterom, 2004] and thereby the duration of the growing phase [Janson et al., 2003].

Despite theoretical and experimental efforts there has not been a consensus on the mechanism of catastrophe and the combined effect of end-binding proteins and force on the catastrophe process. Addressing these issues is the goal of this thesis and we begin by observing the binding dynamics of the end-binding protein mal3. We do so by using an *in vitro* assay where we monitor the intensity changes of fluorescently-labelled mal3 and fluorescent microtubules during catastrophe. For this we compare the results obtained for free microtubules and for microtubules growing against glass barriers where they generate compressive forces.

3.2 Results

Maurer et al. [Maurer et al., 2012] examined mal3 binding before, during and after catastrophes of free microtubules (MTs) *in vitro*. They realized that mal3, on average, begins dissociating from the MT several seconds before the MT starts shrinking. We wanted to examine how this is affected if the MT experiences a force. Previous work has shown that a force highly increases the likelihood for catastrophe [Dogterom and Yurke, 1997, Janson et al., 2003] which should be reflected in the attachment of mal3 to the MT. Since under force the period a MT stays in contact with the barrier is sometimes only a few seconds we wonder how this speed-up is reflected in the loss of mal3 from the MT tip.

To clarify these issues we used the following assay: MTs were nucleated *in vitro* from surface-attached stabilised MT seeds in the presence and absence of the end-binding protein mal3, as shown in figure 3.1. To check whether head-on forces change the behaviour of end-binding proteins we also looked at those MTs in contact with a barrier. For this purpose the glass surface contained micro-fabricated rigid barriers which allowed the generation of forces when MTs grew against them. The seeds were distributed at random such that only some of the dynamic MTs could reach the barriers. This allowed us to compare microtubule dynamics and protein binding in the absence and presence of forces.

3.2.1 MTs interact with the barriers in different ways

After dynamic MTs reached the barrier two scenarios emerged:

- MTs seeded close to the barrier while their tip was located stationary at the barrier experienced a strong length-dependent, growth-opposing force [Dogterom and Yurke, 1997]. When this force was high enough, they stopped growth and are therefore named "stalling MTs", see fig. 3.2a. In these cases we do not exclude the occurrence of buckling with low amplitude which was unable to detect by eye.
- MTs grew at the barrier while their tip was moving, see fig. 3.2b. The length increase resulted in bending and sliding along the barrier ("sliding MTs"), and hence minor forces.

A third option would be MT "buckling", i.e. growth with a fixed MT tip resulting in buckling of the MT, see fig. 3.2c. We did not observe buckling MTs in our experiments.

Since stalling MTs experience a constant and high force and therefore experience the largest effect of force on EB-binding we focused in our analysis only on these MTs. Sliding MTs, on the other hand, experience a force of changing magnitude and often go out of focus. Therefore we excluded phases of sliding MTs from our analysis.

3.2.2 Determining protein intensities at the ends of MTs

The microtubule seeds nucleated both microtubule plus and minus ends. For analysis we specifically chose MT plus ends as only they are dynamic *in vivo* (the minus ends are attached to microtubule-organising centres). We could select MT plus ends since they are characterised by faster assembly than minus ends and a more frequent transition to depolymerisation [Walker et al., 1988].

In the recorded tiff-stacks we drew a line along the length of the free MTs and the ones which were stalling at the barrier at some time during the recording. We determined the intensity along this line for each frame of the stack to obtain a space-time plot (kymograph), see fig. 3.3a. In those kymographs we traced the MT seed and the growing MT plus end by straight connected lines (from here on referred to as region-of-interests, ROIs). Each

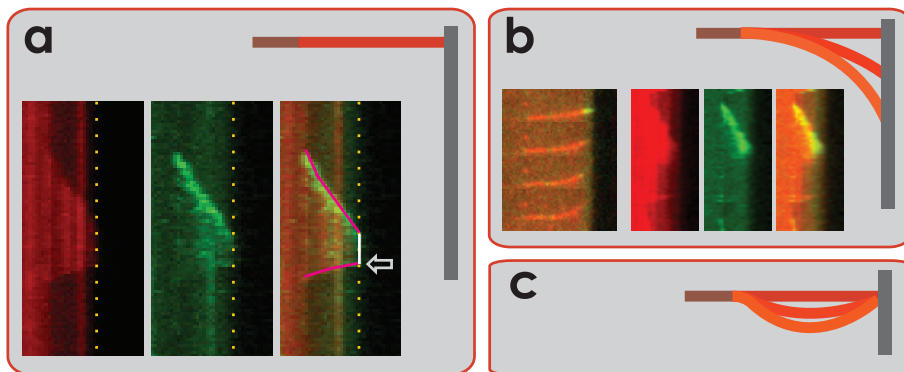


Figure 3.2: Types of MT-barrier interaction and their analysis. **a.** Schematic image of a stalling MT (red) grown from a surface attached seed (dark red) in contact with a barrier (grey). A MT is considered stalling if its length does not change while its tip is located stationary at a local barrier irregularity. *inset.* Kymographs showing rhodamine-tubulin (red), mal3-alexa488 (green) and a colour-merge. We analyse these MTs by tracking the MT tip by hand with straight lines (pink/white lines). Each straight line corresponds to growth at roughly constant speed. MTs growing against a barrier contain a free growth part (pink lines) and a barrier-contact part (white line). The barrier interface is indicated with a yellow dotted line. **b.** Schematic image of a sliding MT (red-orange). MTs are depicted in lighter shades of red when getting longer, for better view. A MT is considered sliding if it grows while its tip is sliding along the barrier. We do not analyse these MTs since they experience minor forces. *inset left.* Time-series of a MT reaching the barrier and then sliding upwards. The elapsed time between images is 10 s. *inset right.* Kymographs of the same sliding MT. The sliding is obvious from the temporary loss of signal from the rhodamine-tubulin channel. **c.** Schematic image of a buckling MT. MTs are considered buckling if they grow while their tip is remaining stationary at the barrier. The length increase results in buckling of the MT. We did not observe buckling MTs.

line corresponds to a period where the MT was growing with roughly constant speed, see fig.3.3b. Besides, we labelled each ROI as free or stalling at the barrier and recorded the times of catastrophes.

For our imaging we used a TIRF-microscope which functions by internal reflection of the excitation light at the sample surface. This light only excites fluorophores in the vicinity of the surface and therefore gives a clear signal without fluorescent noise from the background. However, at the barriers light is not perfectly internally reflected but strays into the sample where it excites fluorophores in the background. Therefore, contrast is decreased slightly in a 1-2 μm wide region along the barrier (see fig. 3.2b.). For this reason we also measured the tubulin intensity simultaneously with the mal3 intensity. We use it as a reference for the mal3 intensity: when at the barrier or due to defocusing the tubulin intensity decreased, we could correct for this in the mal3 signal.

Due to the decrease of contrast at the barrier and since the background intensity is never perfectly homogeneous in a sample careful background subtraction is necessary. Consequently, we made the background subtraction in both the rhodamine-tubulin and the mal3-alexa488 channel position-dependent. Imagining the kymograph to be positioned such that time is vertical and space horizontal (as shown in the figures), we proceeded

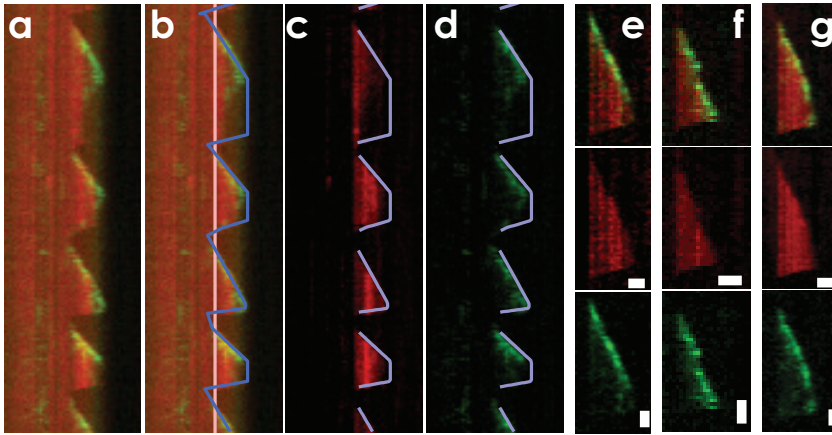


Figure 3.3: Determining protein intensities at the ends of MTs. **a.** Kymograph of a MT sliding and stalling repeatedly at the barrier. **b.** The same kymograph where straight lines (region-of-interests, ROIs) are fitted to the MT end (blue) and the seed (light pink). The ROI at the MT tip is shifted two pixels left and one to the right to cover the whole comet. **c.** The same kymograph is background subtracted and split into the rhodamine-tubulin and **d.** Mal3-Alexa488 channel. The blue ROIs show the rightmost intensity profile during periods of MT growth/shrinkage. **e.** Mal3 intensity often decreases several seconds before catastrophe, from top to bottom: colour merge, tubulin and mal3 channel. **f.** In other cases mal3 only dissociates from the MT tip at catastrophe. **g.** Occasionally, we observed a dim MT end before the MT underwent catastrophe several frames later. The mal3 intensity is only slightly decreased. Horizontal scale bars are 1.3 μm and vertical ones 16 s.

column-wise: the average intensity in each column of a predefined rectangle was subtracted from each column of the kymograph. Figure 3.3b-d. shows the rectangle for background subtraction and the resulting background subtracted rhodamine and mal3 channels.

We then determined the protein intensities along the ROIs tracing the MT end. Since these ROIs were drawn along the MT tip which is not necessarily the peak intensity of the comet, we shifted the ROIs two pixels left and one to the right. We did not shift the ROIs further since mostly the comet is not longer than four pixels. Subsequently we determined the maximum mal3 intensity of the four pixels and the rhodamine-tubulin intensity in the same pixel, or, we obtained the sum of the four pixels. Effectively that means that we obtained the peak intensity and the (integrated) comet intensity in a four-pixel region along the length of the MT. However, we did not take into account the intensity variation along the width of the MT. Our method works well as long as the MT does not go out of focus or fluctuates sideways in the tiff-stacks. However, since our MTs stayed mainly in focus, we believe the error due to fluctuations to be small.

A plot of mal3 and rhodamine-tubulin intensities is shown in figure 3.4. In this figure we also marked the time of catastrophes (by vertical lines) and times during which the MT was stalling or sliding along the barrier (grey or dark green bars, respectively). Obviously, during barrier contact the mal3 and tubulin intensity decreased which is not only an effect of the diminished absolute light intensity at the barrier, as we shall see later.

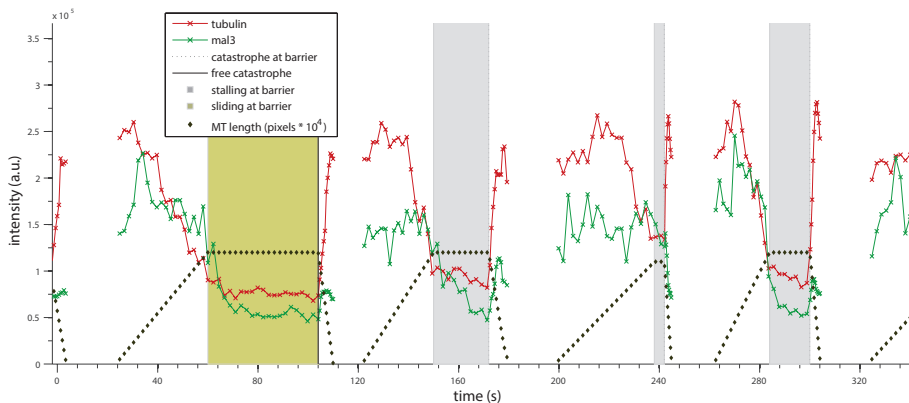


Figure 3.4: Fluorescence intensity at the ends of a MT. Maximum comet intensity of mal3 (green) and of tubulin (red) obtained from the background subtracted kymograph as shown in fig. 3.3c-d. Black vertical lines denote catastrophes while vertical bars correspond to stalling (grey) or sliding at barrier (light green). MT length as obtained from the line fit (brown) is shown.

3.2.3 The average mal3 intensity at the ends of free MTs

Before further analysis we normalised both the red and green signal. We first calculated the mean intensity of each rhodamine tubulin trace during periods of MT growth (no pausing). Second, we divided each intensity by this mean red intensity. We then aligned all the intensity traces obtained for free MTs with their catastrophes, as shown in figure 3.5a. At times before the vertical black line, the MT was growing or pausing such that the onset of shrinking is at time 0. After catastrophe we followed the intensity at the MT end until the MT shrank back to the seed or at most 16 frames.

To get an average mal3 intensity we proceeded time-wise: for each time point we determined the average intensity of all existing signals. Since not all MTs lived equally long, at times long before and long after catastrophe the number of averaged MTs is lower than right before catastrophe where we averaged over all the 115 traces. The resulting curves, obtained from the maximum intensity in the four pixel long region, can be seen in figure 3.5b. During growth we see the average mal3 comet peak intensity fluctuate slightly, reflecting the MT's intrinsic intensity fluctuations but also fluctuations between different MTs. Several seconds before catastrophe the mal3 intensity starts decreasing and reaches the lattice intensity 10-15 s after catastrophe. The average rhodamine-tubulin intensity at the MT tip is constant during the period of observation except around catastrophe (about 5 s before to 5 s after catastrophe). We see several possible reasons. First, we might not be tracing the MT tip correctly. We often see a short pausing phase before catastrophe which we might not have taken into account if the pause was shorter than three pixels. Second, the intensity of the MT tip is occasionally less bright before catastrophe. A possible reason could be the formation of an incomplete MT tip. For this note, that the tubulin intensity is, on average, higher after catastrophe than even during growth and during catastrophe (see figure 3.5b-d.). If the first reason would be correct, so if we would be tracing the background next to the MT tip we would of course also get a wrong information in the mal3 channel. To examine this we increased the number of profiles to six (3 left and 2 right of the original ROI-profile) and

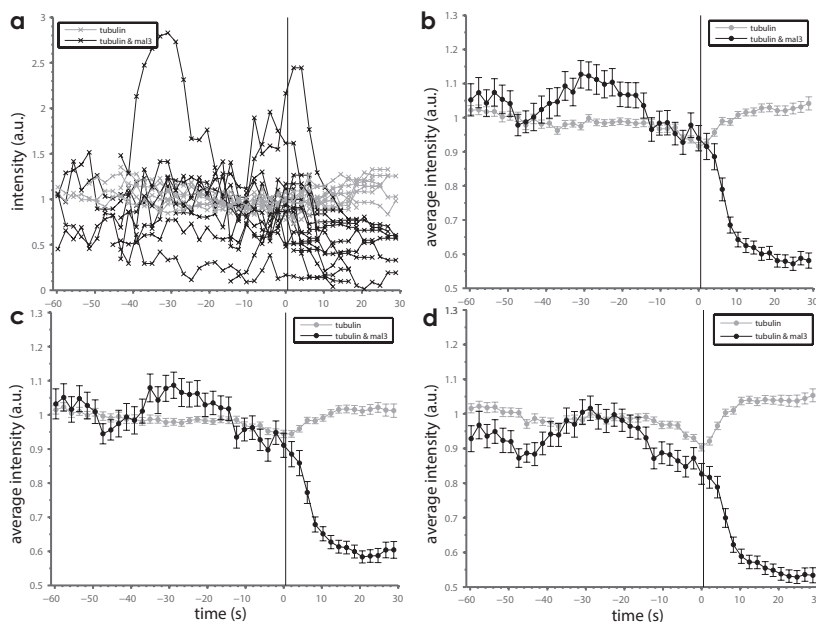


Figure 3.5: Protein intensities at MT ends during free growth. **a.** Rhodamine-tubulin (black) and mal3-Alexa488 intensity (grey) were measured at the ends of 115 freely growing MTs. Here, we show a selection of these traces each presenting the maximum intensity of a four pixel long line along the length of the MT comet. Each trace is normalised by its average rhodamine-tubulin intensity. All traces are aligned such that the MT length starts decreasing at time = 1 s. The catastrophe is denoted by the vertical black line. **b.** We then get the average rhodamine and mal3 intensity by taking the mean of all the intensities existing at a specific time. At times long before catastrophe and long after catastrophe we therefore average over fewer traces than at catastrophe. The error is the std. **c.** Analogously to **b.** we determined the maximum of a six pixel long line along the length of the MT comet. **d.** We also determined the sum of four pixels along the length of the MT comet.

analysed from then on analogously to described above. We see that in this case the dip in intensity during catastrophe is indeed diminished (see fig.3.5c). However, the mal3 intensity stays the same which speaks against wrongly tracing the MT tip. The decrease in rhodamine intensity must be therefore inherent to the MT.

Figure 3.5d. shows the total comet intensity (i.e. that the sum of the four pixels at the MT tip). Just as in figure 3.5b and c. the mal3 intensity decreases in the order of 10 s before catastrophe. The rhodamine-tubulin intensity also shows the dip during catastrophe confirming a decrease in intensity of the MT tip shortly before catastrophe.

3.2.4 The average mal3 intensity at the ends of MTs stalling at the barrier

To compare the binding behaviour of free MTs to MTs under force we also normalised and averaged the intensities obtained from MTs under force as described above. Here we aligned

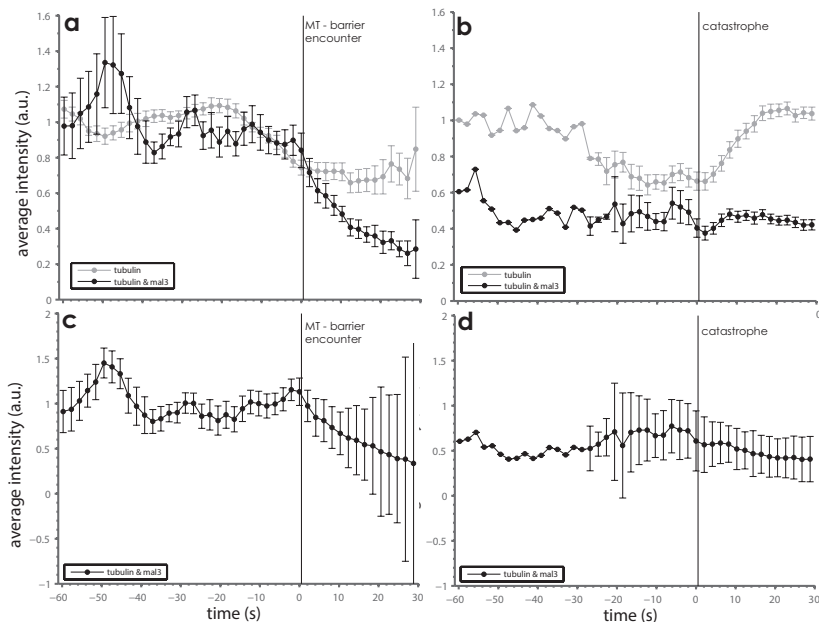


Figure 3.6: Average mal3 intensity at MT ends during stalling at the barrier. Average maximum intensities are obtained from a four pixel long region and analysed as mentioned for free MTs. **a-b.** Average maximum intensities aligned when MTs encountered the barrier or with their catastrophes, respectively. **c-d.** The absolute light intensity is lower at the barrier reflected in the decreasing tubulin signal. To cancel out this effect we divided, in these plots, the average mal3 by the average tubulin intensity. Errors are std.

the seventeen barrier-stalling events at the time the MT reached the barrier and at their catastrophes, as can be seen in figures 3.6a and b., respectively. As mentioned before, the tubulin intensity is a measure of the MT's absolute light intensity. Since the tubulin signal is less bright at the barrier also the mal3 intensity must be diminished. To compensate we divided the average mal3 by the average tubulin intensity. The resulting curves are shown in figure 3.6c and d., for MTs aligned with their barrier encounters and catastrophes, respectively. Figures 3.6a and c. show that for times $t < 0$ the MT intensity is noisy reflecting intrinsic fluctuations in fluorescent intensities during free growth. However, it is clear that the mal3 intensity drops as soon as the MT reaches the barrier. Figures 3.6b and d. show for times $t < 0$, MTs stalling at the barrier prior to catastrophe. We only observed one MT which stalled at the barrier longer than 30 s, therefore the trace between $t = -60$ s and $t = -30$ s is obtained from one single MT stalling at the barrier. The intensity fluctuations for $t < -30$ s hence reflect the intrinsic mal3 intensity variation. After catastrophe the average intensity decreases very slightly, however, we consider this as an ongoing decrease induced by the onset of force and not induced by the catastrophe.

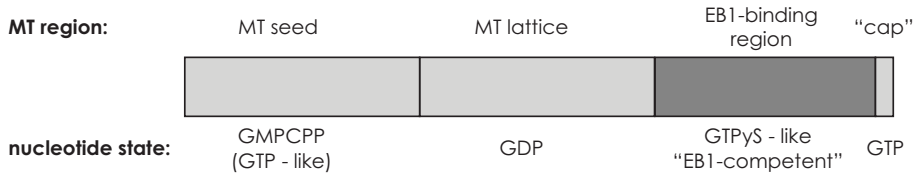


Figure 3.7: Different regions on the MT. Experiments have shown that EBs have very low affinity for the very tip of the MT (referred to as "cap") or the seed, both characterised by tubulin being in a GMPCPP (GTP-like) nucleotide state. Similarly, the MT lattice, in the GDP nucleotide state, is also not bound by EBs. But EB1/mal3 binds to a MT composed of GTP γ S-tubulin, a slowly hydrolysable GTP analogue with a modification of the γ -phosphate. It is similarly favourable for EB-binding as is GDP/BeF⁻-tubulin which mimics an early hydrolysis transition state [Carlier et al., 1989]. Further, EB1/mal3 binds to a region at the MT end (EB1-binding region) thus thought to be in a comparable state as GTP γ S or GDP/BeF⁻-tubulin [Maurer et al., 2011, Maurer et al., 2012]. We name this the "EB1-competent state".

3.3 Conclusions and discussion

By TIRF microscopy we have examined the effect of force on end-binding protein binding during MT catastrophe. We obtained the mal3 comet intensity of MTs growing freely in solution and those stalling at a barrier. More precisely, we determined the peak intensity and the sum of intensities from a four pixel region along the length of the MT. In general, we saw that the mal3 intensity decreases in some events even tens of seconds before catastrophe while in other cases it decreases only after the MT started shrinking. On average, therefore, the mal3 intensity starts decreasing several seconds before catastrophe (within our errorbars we estimate this to 10 ± 5 s) and gradually decreases until the lattice intensity is reached, on average approximately 15 s after catastrophe.

We thus reproduced data by Maurer et al. [Maurer et al., 2012] who also performed mal3 intensity measurements on free MTs. However, by fitting the mal3 comet and MT length with 2D and 1D functions, they could get more accurate information and determine the time of catastrophe more precisely. Compared to their results in our case the drop in intensity before catastrophe is not as obvious. This makes sense considering our method of analysis. Since we detect the catastrophe with a possible error of 1-2 time frames our intensity traces might be slightly misaligned with respect to each other. Further, we determine the peak and the total comet intensity separate from each other in a fixed-length manner disregarding possible variations in comet size. However, this does not influence our results a lot. It has been shown that the MT comet size (length) and the peak intensity depend on the mal3 concentration [Bieling et al., 2007, Munteanu, 2008]. In our concentration regime both the peak and comet length are similarly affected by catastrophe and therefore obtaining the maximum or sum of the four pixels gives us in both cases enough information. Nonetheless the experimental differences between [Maurer et al., 2012]'s and our efforts, both bring the same message across: mal3 intensity starts decreasing before catastrophe.

Maurer et al. [Maurer et al., 2012] also provided an explanation for mal3 unbinding before catastrophe. With a combination of TIRF-M and cryo-EM the authors showed that mal3/EB1 is positioned longitudinally between the α - β interdimer interface and laterally between two adjacent α - α or β - β tubulins. In this position it contacts also the H3-helix of β -tubulin which binds GTP nucleotides. Therefore, mal3/EB1 is ideally

positioned to sense the nucleotide state of tubulin. Moreover, mal3 binds to GTP γ S and GDP/BeF⁻ (mimicking an early GTP hydrolysis state) but not to GMPCPP-MTs though the latter is mimicking the GTP hydrolysis state of GTP-MTs [Hyman et al., 1992]. This is indicative of mal3 rather binding to a nucleotide state induced by GTP hydrolysis than to the GTP-tubulin itself. We refer to this state as "EB1-competent" which, together with other MT regions and corresponding nucleotide states, are visualised in figure 3.7. The difference between a GTP nucleotide state and the one induced by GTP-hydrolysis (EB1-competent state) would also explain the discrepancy between the long mal3 comet with hundreds of binding sites [Bieling et al., 2007, Bieling et al., 2008, Dixit et al., 2009] versus the GTP cap of only several GTP-tubulins [Caplow and Shanks, 1996, Drechsel and Kirschner, 1994]. The fact that EB intensity decreases before catastrophe is originating from two possible reasons: either catastrophe is caused by unbinding of mal3 or by a change in the nucleotide state of tubulin. The authors argue that the former scenario is unlikely since *in vitro* an increase in mal3 concentration and thus bound mal3 increases the catastrophe probability. Therefore, a change in the nucleotide state of tubulin (from the EB1-competent state to the GDP nucleotide state) must be triggering catastrophe. This change in nucleotide state is accompanied by the loss of mal3. In conclusion, the mal3 binding region can be seen as a protective zone of the MT against depolymerisation. If it is lost, the MT is prone to catastrophe.

Further, the authors found that the mal3 decoration time of the MT plus end decreases with increasing mal3-concentration which is indicative of mal3 destroying its own binding site [Maurer et al., 2011]. In this way, mal3 might be promoting the GTPase activity of an α -tubulin monomer for an α -monomer of the one below it in the lattice [Nogales, 2000].

When MTs encounter a barrier and thus experience a compressive force we saw that mal3 dissociates from the MT, on average, within 10-20 s after barrier contact. Our results show further that upon a catastrophe during barrier-stalling the loss of mal3 is minor, presumably since most mal3 already dissociated at the build-up of forces. Taking into account the results of Maurer et al. [Maurer et al., 2011, Maurer et al., 2012], we can also here assume that a nucleotide change from the EB1-competent to the GDP state triggered the loss of mal3. The loss of this stabilising cap then induced the advance to catastrophe. Therefore, our barrier data shows that a growth-opposing force leads to the transformation of the tubulins in the EB1-competent state. Whether this happens by preventing growth of the EB binding region and what this means for the catastrophe process remains to be elucidated. We will discuss it in the following chapters.

3.4 Methods

Sample preparation. Barriers made of SiO (glass) were micro-fabricated on glass cover slips as described in chapter 2.2.1. Afterwards the cover slips were rinsed with iso-propanol and then rinsed 3x with MilliQ. A flowchamber was assembled by parallely gluing two strips of parafilm between a microscope slide and a coverslip (Merck, Darmstadt, Germany). The flow chamber was functionalised and passivated with a 0.2 mg/ml mix of biotin-PLL-PEG and PLL-PEG (SurfaceSolutions, Switzerland). Residual non-specific binding sites were blocked with 0.5 mg/ml κ -casein and 1 % F-127. Stabilised, fluorescently labelled MT seeds (containing 12 % fluorescent tubulin and 18 % biotin tubulin) were attached by means of a biotin-streptavidin linker. Microtubule growth was initiated by adding MRB80 buffer (80 mM K-PIPES pH 6.8, 50 mM KCl, 4 mM MgCl₂, 1 mM GTP, 1 mM EGTA, 10 mM 2-mercaptoethanol), 0.5 mg/ml κ -casein, an oxygen scavenger system (20 mM glucose,

200 $\mu\text{g/ml}$ glucose-oxidase, 400 $\mu\text{g/ml}$ catalase), 15 μM tubulin of which 5 % was labelled with rhodamine (Cytoskeleton, Denver, CO, USA) and 200 nM mal3-alexa488 (purified as described in [Bieling et al., 2007]). Unless stated otherwise, chemical reagents were obtained from Sigma-Aldrich (Saint-Louis, MO, USA).

Imaging method. The sample was imaged in an inverted Ti-Nikon Eclipse microscope (Nikon, Tokyo, Japan) using total internal reflection fluorescence (TIRF) microscopy equipped with a 1.49 NA, 100x oil immersion objective. Single tiff-images were recorded using a Calypso 491 nm diode laser (Cobolt, Solna, Sweden) and a Jive 561 nm diode laser (Cobolt) imaged with a Roper Scientific Coolsnap HQ CCD-camera (Photometrics, Tucson, AZ, USA) and saved to disk with MetaMorph software (Molecular Devices, Sunnyvale, CA, USA), at time-lapse intervals of 2 s, at typical exposure times of 200-250 ms. After mounting the sample on the microscope stage imaging started after a 5 minute equilibration time. Imaging time was kept below 2 hours (average of 1 hour) at a constant temperature of $25 \pm 0.5^\circ\text{C}$ which was maintained by running heated/cooled water through a sleeve around the objective. Simultaneously, the water temperature was adjusted by Peltier elements to a temperature based on a sensor within the sleeve in proximity to the sample.

Data analysis. Tiff-stacks were background-subtracted and bleach-corrected (macro developed by J. Rietdorf, EMBL Heidelberg, Germany) in Fiji (based on ImageJ which was developed by Wayne Rasband, NIH in Bethesda, MD, USA). Growth trajectories of single MTs were displayed in kymographs where straight lines were fitted to each growth or shrinkage phase by hand/mouse. A phase was defined as continuous growth or shrinkage at constant speed. Coordinates of the line fits were processed in Matlab (Mathworks, Natick, MA, USA) by a custom-made software to determine and average fluorescent protein intensities in the kymographs. This software used the Matlab function *improfile* which obtains the intensity along a predefined ROI-line in approximately pixel-sized intervals.

Acknowledgements

We are grateful for the help and advice with the micro-fabrication received from Chris Rétif and Hans Zeilemaker. Further, we thank Peter Bieling and Thomas Surrey for help with the protein purification of mal3 and Roland Dries for help with the imaging. The work presented in this chapter was carried out as part of the EU Program AMOCROSS, as part of a "VICI" grant provided by the "Nederlandse Organisatie voor Wetenschappelijk Onderzoek (NWO)" and as part of the research program of the "Stichting voor Fundamenteel Onderzoek der Materie (FOM)", which is financially supported by the "Nederlandse Organisatie voor Wetenschappelijk Onderzoek (NWO)".

4

How do end-binding proteins affect microtubule dynamics?

A key question in understanding microtubule dynamics is how the microtubule evolves to catastrophe, the transition from assembly to rapid disassembly. Experimental and theoretical efforts provided a range of different mechanisms sometimes supplemented with the results obtained from microtubule regulation by end-binding proteins. To clarify this problem we investigate microtubule dynamics *in vitro* in the absence and presence of end-binding proteins. Using total internal reflection fluorescence microscopy we confirm that the protein complex, consisting of mal3, tea2 and tip1, enhances the MT growth speed and induces catastrophes. We demonstrate that both in the absence and presence of the end-binding proteins catastrophe can be described by a two-step process. Further, we provide evidence that the catastrophe times can be fitted with a gamma and a sequential-step exponential distribution but also with parallel-step exponential distributions. We reason that a catastrophe evolves with a long-timescale step which is followed or accompanied by a shorter step.

4.1 Introduction

For long it has been questioned whether catastrophe is a stochastic process with first order kinetics. This would imply that catastrophe time is independent of the microtubule (MT) age. It would also mean that catastrophe is a one-step process and that events are independent. While some literature regarded catastrophes as randomly distributed and thus first-order events [Hill, 1984, Mitchison and Kirschner, 1987, Dogterom and Leibler, 1993, Flyvbjerg et al., 1994, Howard, 2001, Phillips R., 2008], other literature showed evidence of catastrophe being a multi-step process [Odde et al., 1995, Odde et al., 1996, Stepanova et al., 2010, Gardner et al., 2011b]. These publications provide a range of explanations for catastrophe, the most prominent originating from GTP hydrolysis [Maurer et al., 2012].

As we have shown in chapter 3 MT ends have emerged as dynamic regulatory sites which are bound and modulated by end-binding proteins (EBs). Research has focused on the effect of EB1 (or its homologue mal3), but the observation of other EBs (possibly joint with EB1) might lead to different results.

In order to get a better understanding of the catastrophe process of MTs and

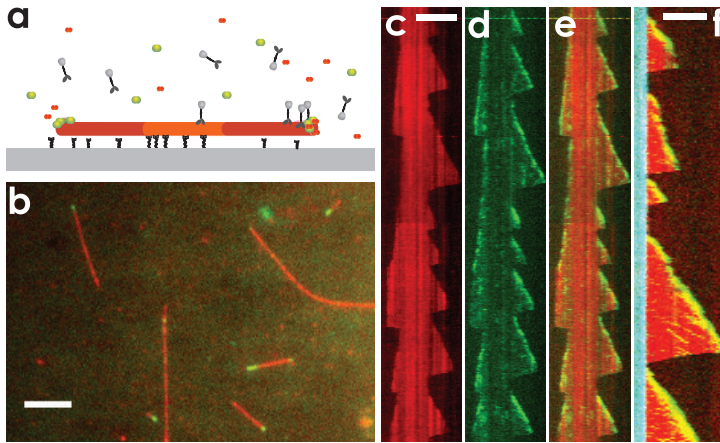


Figure 4.1: Assay of dynamic MTs in the presence of end-binding proteins. **a.** Schematic setup: dynamic MTs (red) grow from stabilised surface-attached seeds (orange), optionally in the presence of end-binding proteins mal3-alexa488 (green) (and tea2 and tip1 (black/gray)). **b.** TIRF-image of MTs (red) and mal3 (green). **c-e.** Kymographs of the rhodamine-tubulin channel, mal3-alexa488 channel and a colour merge (from left to right). **f.** Kymograph of a (red) MT grown from a blue seed in the presence of unlabelled mal3 and tip1 and green-fluorescent tea2-alexa488. The successful end-tracking proves the functionality of all three proteins, since tea2 end-tracks only in the presence of both tip1 and mal3 [Bieling et al., 2007]. All scale bar are 5 μm long.

the accompanying role of (individual) end-binding proteins (EBs) we examine dynamic microtubules *in vitro*. The MTs are grown in the presence of tubulin alone, tubulin together with the end-binding protein mal3, or together with mal3, tea2 [Browning et al., 2000, Browning et al., 2003] and the Clip170-homologue, tip1 [Brunner and Nurse, 2000b]. All three proteins are necessary for the correct functioning of tip1 [Bieling et al., 2007]. One function of tip1 has been elucidated in tip1 deletion cells where an increased catastrophe frequency resulted in shortened MTs and misshaped cells [Busch et al., 2004]. In detail the protein complex functions by mal3 associating to the MT lattice with weak affinity but preferentially to the growing MT ends. There it exchanges rapidly and mediates loading of the complex tea2-tip1 which *in vivo* support the transport of growth factors to the growing cell poles. Only when together can tip1 and tea2 move towards and bind to MT's growing plus end where they accumulate [Bieling et al., 2007].

4.2 Results

The stochastic switching of an intact growing microtubule (MT) to a disassembling shrinking MT remains a puzzling subject. With our experiments we want to investigate how a MT transitions to catastrophe. In particular, we want to know whether a

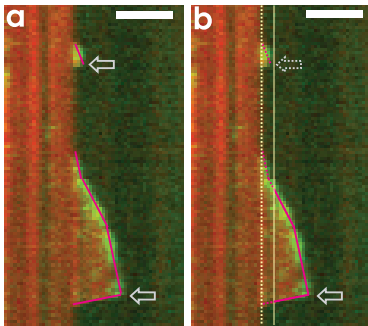


Figure 4.2: Determining MT growth times and MT lengths from kymographs. **a.** The MT tip was tracked by hand with straight (pink) lines. Each straight line corresponds to growth at constant speed. Transition to shrinkage, termed catastrophe, is indicated with open arrows. Short growth excursions (upper MT) were only counted if they had a signal of 3-by-3 pixels. Longer growth excursions (lower MT) were usually composed of several phases at different constant speeds, here of three growth and one shrinkage phase.

Using basic geometry ideas we determined for each line the corresponding growth or shrinkage time (vertical part of the line) and MT length (horizontal part, see text). **b.** The same kymograph as in **a.** where the seed tip is indicated with a yellow dotted line. The seed is artificially elongated until its tip ends at the yellow continuous line, all events left of it are discarded (indicated by pink dotted lines and arrow). Only the remaining part of the growth excursions (continuous lines and arrow) are taken for analysis in the same method as described in **a.** Scale bars represent 3 μm .

catastrophe is a random process or can be better described by a multistep process. Finally we want to gain deeper insight into the nature of the sub-step(s).

4.2.1 Assay to examine microtubule dynamics in the presence of end-binding proteins

In order to address our research questions we grow dynamic MTs from surface-attached stabilised seeds in three conditions. The ambient buffer contained either:

- tubulin
- tubulin and mal3 or
- tubulin and the three EBs, mal3, tea2 and tip1 (referred to as "mal3-tea2-tip1"), where the latter is shown in figure 4.1a. MTs nucleated from both minus and plus ends of the seed, but for analysis we specifically chose the plus ends. *In vivo* the minus ends are attached to microtubule-organising centres or centrosomes and thus only MT plus ends are relevant in cells. We could differentiate MT plus ends since they assemble faster than minus ends [Allen and Borisy, 1974] and transition more frequently to depolymerisation [Walker et al., 1988].

From the recorded time-lapse TIRF images we created kymographs (space-time plots) for the individual MTs (see fig. 4.1c-e). In these kymographs we tracked the MT ends by hand where we assigned a straight line to a continuous growth or shrinkage phase, for an example see fig. 4.2a. Considering a right-angled triangle where the tracking line is the hypotenuse we could determine MT growth time (vertical side of the triangle) and MT length (horizontal side). From these parameters we could calculate MT growth speed and catastrophe times.

Since only mal3 was fluorescently labelled we could not observe the functionality of tip1 directly. Therefore, we also did experiments with unlabelled mal3 and tip1 and

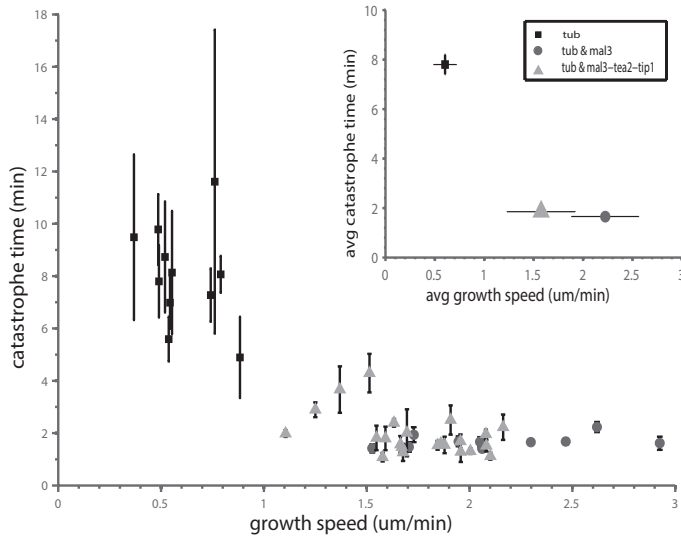


Figure 4.3: End-binding proteins reduce catastrophe time and increase growth speed of free MTs. Each data point represents an average weighted growth speed and catastrophe time per sample. Samples were of three types of conditions: tubulin alone, optionally with the addition of mal3 or of mal3-tea2-tip1. For simplicity we assumed here that catastrophes are random events which allowed us to calculate catastrophe time as the sum of observed growth times per sample over the sum of observed catastrophes. Error of the catastrophe time is \sqrt{N} , where N is the number of observed catastrophes per sample. **inset.** To determine the average growth speed per experimental condition we pooled all growth speeds together and weighted each by their growth duration. The error is the weighted standard deviation. The average catastrophe time was calculated as the sum of all observed growth times from the independent samples over the sum of all observed catastrophes. The error is $\sqrt{N_{\text{tot}}}$, where N_{tot} is the total number of catastrophes per experimental condition.

labelled tea2-Alexa488. Under these conditions tea2 end-tracked well (see fig. 4.1f) ensuring the activity of mal3 and tip1 [Bieling et al., 2007].

4.2.2 MTs are more dynamic with EBs

For simplicity we first assumed that catastrophes are randomly distributed, and therefore neither MT growth time ("MT age") nor MT length would influence the catastrophe time. Thus, it did not matter whether a growth event started at the seed or after a rescue and whether it ended with a catastrophe. As a result we determined a catastrophe time per sample τ_c as the sum of all observed growth events in all kymographs of that sample divided by the total number of observed catastrophes. Figure 4.3 shows these catastrophe times τ_c and growth speeds per sample. The different symbols correspond to the three different protein conditions. Compared to the case of pure tubulin, in the presence of the end-binding protein mal3 MTs become more dynamic. Catastrophe times are reduced and growth speeds are

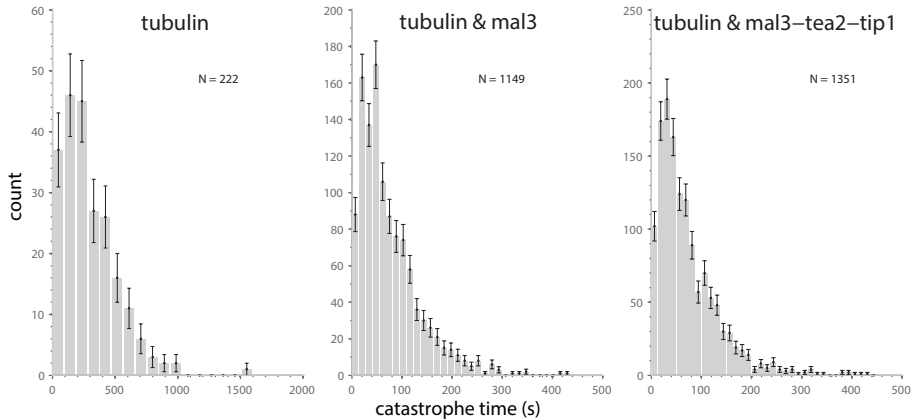


Figure 4.4: Histograms of catastrophes times. N refers to the number of complete growth events from MT nucleation until transition to shrinkage.

increased, agreeing with previous *in vitro* results [Munteanu, 2008, Maurer et al., 2011] (for EB1 [Vitre et al., 2008]). In the presence of mal3, tea2 and tip1 the increase in growth speed and decrease in catastrophe time is almost as strong. The slightly shorter catastrophe time compared to the presence of only mal3 indicates that tip1/tea2 give a slight protection against free catastrophes as shown previously [Munteanu, 2008] and *in vivo* [Brunner and Nurse, 2000b].

4.2.3 Insights into the catastrophe process

As mentioned above, with our work we want to determine whether a catastrophe is a single or multi-step process. Since in the latter case MT age and MT length influences the catastrophe time we now regard only events starting at the seed and ending with a catastrophe. In general, the kinetics underlying a catastrophe can be determined from the catastrophe time distribution. We therefore plot histograms of catastrophe times with objectively determined bin size [Freedman and Diaconis, 1981], see fig. 4.4. Comparing the distributions in the presence of EBs and their absence, the most obvious difference lies in the longer time scale in the tubulin case reflecting the catastrophe-promoting effect of EBs (as mentioned above). To quantify the catastrophe kinetics we fitted the catastrophe times with three different distributions:

- The exponential distribution (fig. 4.5a) is characteristic for first-order transition kinetics and has been assumed to be the prevailing model of catastrophes. In this case an intact MT transitions with rate $k = \tau^{-1}$ to a shortening state.
- The gamma distribution has been used to describe multi-step reactions [Rice, 1995, Floyd et al., 2010, Gardner et al., 2011b]. It represents a non-first order process with several irreversible random steps n where each step happens with an equal characteristic rate k . The probability-density function (pdf) of the gamma

distribution describing catastrophes:

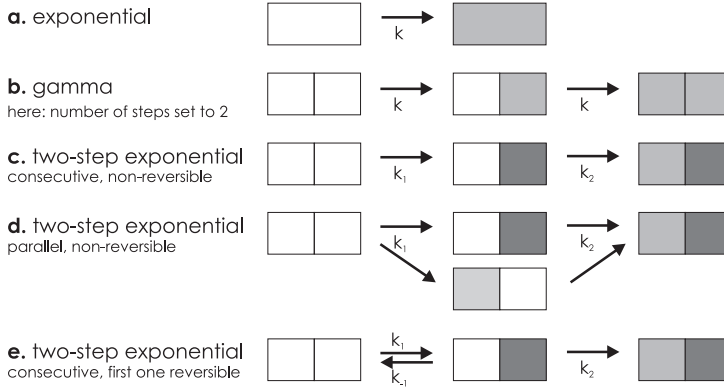


Figure 4.5: Schematic of different catastrophe models. Catastrophes can be described by different models. Here a grey box denotes the accumulation of a catastrophe promoting event. If all boxes are grey the MT transitions to catastrophe. **a.** Catastrophes as stochastic events without memory of the assembly. **b.** Catastrophe happens in several steps where each step is the same and has the same rate. **c.** Two steps are assumed with each a different rate and possibly of different nature. **d.** The two steps can happen in parallel **e.** or one of them can be reversible. The last model was for simplicity not considered for our data. However, we include the special case k_1/k_{-1} which reduces to the distribution described by *a.*

distribution is defined as:

$$f(t) = \frac{k^n t^{n-1} e^{-kt}}{\Gamma(n)}, \quad (4.1)$$

where $\Gamma(n)$ is the gamma function. Figure 4.5b shows a gamma process with only two steps, yet in general the gamma distribution represents processes with a number of steps ranging to infinity. (Actually, the exponential is a special case of a gamma distribution with one step.)

- Multiple reactions are also described by a combination of exponentials [Atkins, 1979, Floyd et al., 2010]. Assuming consecutive and non-reversible steps the reaction is described by a "two-step exponential distribution" (fig. 4.5c) [Zhou and Zhuang, 2007]:

$$f(t) = \frac{k_1 k_2}{k_1 - k_2} (e^{-k_2 t} - e^{-k_1 t}), \quad (4.2)$$

where k_1 and k_2 are the rate constants. This distribution restricts the number of steps to two. On the other hand it allows them to happen with different time scales and thus to be of different nature. Unfortunately, it cannot determine the order of the steps, so k_1 and k_2 are interchangeable.

- If the steps are independent but all necessary to complete the reaction two possibilities emerge:

If the rates k_1 and k_2 are different and in total two steps are allowed we will refer to this distribution as "parallel two-step exponential distribution" (fig. 4.5d). The probability to complete the reaction up to time t is (the cumulative distribution function (cdf)):

$$F(t) = (1 - e^{-k_1 t}) (1 - e^{-k_2 t}). \quad (4.3)$$

- If the rates k are the same and the number of steps n is not fixed the probability to complete the reaction up to time t is:

$$F(t) = (1 - e^{-kt})^n. \quad (4.4)$$

We call this "parallel multistep-exponential distribution". This function is very similar to the parallel two-step exponential distribution, but, similar to the gamma distribution, it describes processes with same rates and the number of steps as a fit parameter.

In all the above mentioned distributions we assumed the steps towards catastrophe to be irreversible: once a reaction took place it cannot be undone. Generally however, the catastrophe mechanism could comprise a reversible step. Figure 4.5e shows such a reaction where the first step is reversible. In this case the catastrophe process comprises a backward step, meaning the first catastrophe promoting event can be undone. Considering only the first step the combination of forward- and backward-exponential together would yield a peaked distribution. Practically, this would describe a reaction of a fixed time duration. Such a scenario can of course be envisaged as a possible mechanism of catastrophe. However, with our data we would not be able to differentiate such a distribution from a gamma or two-step exponential reaction. Further, with a third parameter we would try to extract more information from our data than is reasonable. Nevertheless, there are two limits which would simplify a distribution with a reversible step. First, if the back-reaction was small, so negligible, we would retrieve the two-step exponential. Second, if on the other hand, the back-reaction was as likely as the forward-reaction, the complete process would be dominated by the second step only. In this case the distribution would be an exponential again. Thus, both cases would not yield more information.

Figure 4.6a shows our data fitted with exponential, gamma and two-step exponential distributions. Obviously in none of the conditions does the exponential distribution fit our data well for short time scales. Those "missing" short-time events indicate that catastrophe is actually a process comprised of several steps. If catastrophe was a first-order process fitting with an exponential distribution would yield the same result as averaging over all (growth) events, as shown in figure 4.3. Clearly, when comparing the two times this is not the case, corroborating that catastrophe is not a one-step process.

The gamma distribution, representing processes with several steps, fits the data better and suggests catastrophe to be comprised of 1.5-1.8 steps (depending on the experimental condition). Since the gamma distribution gives the lower limit on the number of steps [Floyd et al., 2010] and physically only an integer number of steps

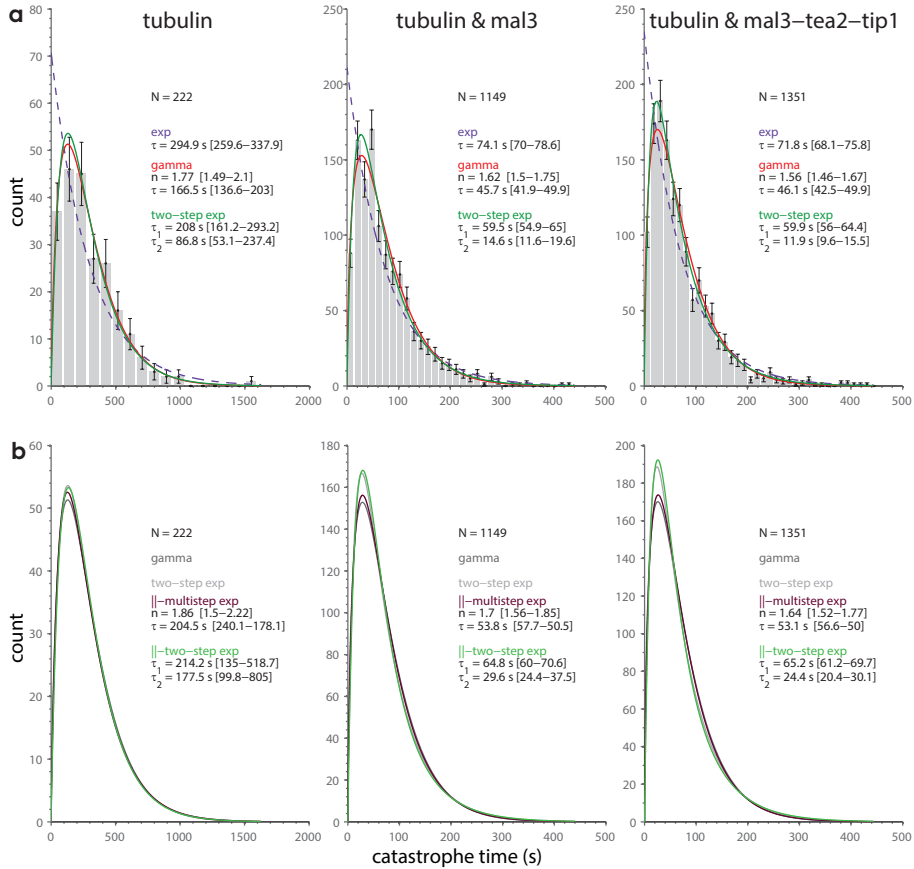


Figure 4.6: Distribution fitting of free catastrophes. Unbinned catastrophe times were fitted with **a.** exponential, gamma and two-sequential step exponential distributions (pdfs) or **b.** with parallel gamma and parallel two-step exponential distributions (pdfs). Histograms of catastrophe times (a.) and the fits are shown where the pdfs are scaled to match the histograms. N refers to the number of complete growth events from MT nucleation until catastrophe. The fit results are displayed in the figure with the 95% confidence intervals in square brackets.

makes sense we identify catastrophe to be a two step mechanism. The fact that our fits gives us an unnatural fraction of a step could be a result of measurement noise. On the other hand, it could indicate that the gamma distribution does not represent our data well. The fraction could be a sign that we do not have two steps of equal time scales and that therefore the imposition of equal rates would be wrong [Floyd et al., 2010].

We therefore also fitted with a sequential-step exponential distribution. Since the gamma distribution fit suggested two steps until catastrophe, we also choose a two-step exponential distribution. Clearly from figure 4.6a these fits are better than the simple exponential distribution for all experimental conditions. They suggest two steps occurring with a shorter and longer rate. As a test, we also fitted with a three-step-exponential distribution. Two of the estimated rates are very similar to the rates from two-step exponential fit, while the third rate is almost zero (data not shown). This is another evidence for the catastrophe mechanism being comprised of two steps.

Also the parallel multistep and parallel two-step exponential distributions fit the data well (fig. 4.6b). The parameter estimates are similar to the fits with the sequential step distributions, except that the time scales are a bit longer. In the parallel two-step exponential case the shorter time even doubled. This makes sense since when the transitions to intermediate states can proceed simultaneously, they can also take longer than if they proceeded sequentially.

4.2.4 The catastrophe mechanism based on information from the long times

It is important to notice that the important information in determining the type of distribution lies in the short time scales. However, these are experimentally hard to determine. Background noise, point-spread function of the microscope and digitisation of the image make it impossible to differentiate MTs shorter than 400 nm from the seed. Even when dynamic MTs and seeds each contain a different fluorophore we do not consider MTs shorter than ~480 nm (in a kymograph this corresponds to a fluorescent intensity of at least 3-by-3 pixels), refer to figure 4.2a. In the presence of EBs shorter events are easier to observe as the mal3 signal is comparably bright. Consequently, differentiation between the absence of a MT and a MT containing a mal3 comet is much easier than in the tubulin case. The lower limit for MTs is hence 320 nm (2-by-2 pixels). Nonetheless, also in this case short events can be faultily detected due to a spread of the signal caused by to the point-spread function of the microscope. Of course, difficulties in detecting the spatial extend of MTs makes it also difficult to define their temporal duration. If it is hard to determine whether a MT nucleated or not makes the exact time of nucleation unclear. In this case a newly nucleated MT can only unambiguously be determined if it has a certain length.

In conclusion, missing short events, more likely in the tubulin case, lower the first bin in the catastrophe time histograms. This results in a less steep rise of the distributions at the short time scales and in a shift towards seemingly more steps

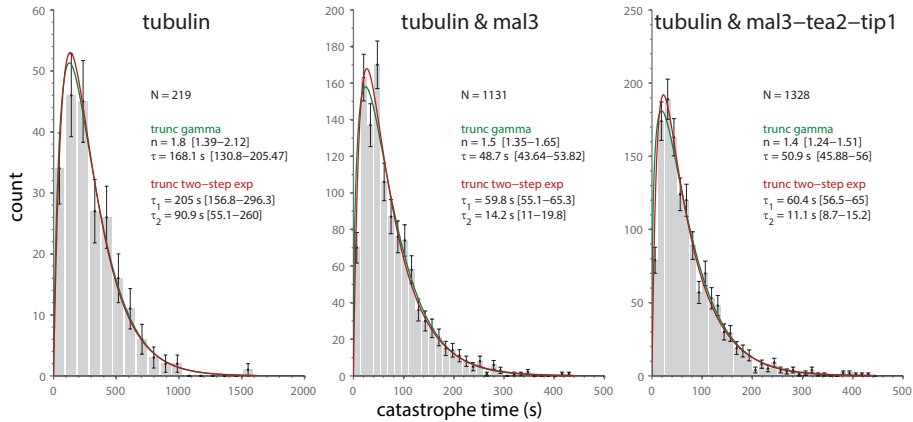


Figure 4.7: Truncated distribution fitting of free catastrophes. Histograms of catastrophe times lasting longer than $t_x=10$ s, 6 s and 6 s for the case with pure tubulin, with mal3 and with mal3-tea2-tip1, respectively (t_x as an example). The unbinned data was fitted with truncated gamma and truncated two-step exponential distributions (pdfs). N refers to the number of complete growth events from MT nucleation until catastrophe which last longer than the truncation limit. The pdfs are scaled to match the histograms. The fit results are displayed in the figure with the 95% confidence intervals in square brackets.

until catastrophe.

We therefore need a method which takes into account the possible error in determining short-term events. One possible method employs artificially elongating the seed. As illustrated in figure 4.2b we imagine the seed to be a little longer than it is in reality. If a MT nucleates from the real seed and does not grow longer than the "new" seed end, we discard this MT. However, if the MT reaches the new seed end, we consider this as MT "nucleation" and analyse the MT from then on. This "seed-elongation procedure" circumvents the problems we have with determining short events (as explained above) because the artificial short MTs have in reality long, easily observable signals. When plotting the new catastrophe times vs. seed elongation we see that we indeed have a higher number of short events (data not shown). This result is confirmed by fitting with the gamma distribution as the number of steps drops slightly, but does not go to one. Conclusively, this is an indication of an experimental error at the short times. On the other hand, it might obscure or delete a possible effect of MT nucleation from the seed which could influence the MT growth time or MT length of newly nucleated MTs. Besides, by discarding many MTs shorter than the artificial elongation we also "miss" the bias for short MTs. Conclusively, the seed-elongation procedure does not take into account a possible error with the short-time events, and we therefore do not regard it as an appropriate method.

An alternative method using the available information (including the short events)

and its putative error in detecting them will be presented as follows: In our case, catastrophe times are well defined except below a certain threshold t_x . Consequently, we can only reliably fit to the values above t_x . Discarding values below t_x we fit to the remaining data with a so-called left-truncated distribution: it is defined as the original pdf in the limits $[t_x, \infty)$, normalised to integrate to one. A left-truncated distribution is hence defined as [Johnson et al., 1994]:

$$f_{\text{truncated}}(t, t > t_x) = \frac{f(t)}{1 - F(t_x)}, \quad (4.5)$$

where $f(t)$ is the original pdf and $F(t_x)$ its cumulative distribution function (cdf) at t_x . For an example of fitting with truncated gamma and two-step exponential distributions see figure 4.6.

As we do not have an unambiguous way of fixing t_x in the first place, we varied t_x from 0 to 20 s in half-second steps. We choose this upper limit because we can safely exclude making errors in determining catastrophe times longer than 20 s. Besides, it is a long enough range to see trends in the fit parameters. For each t_x we discarded measured catastrophe times below t_x and fitted the remaining catastrophe times with left-truncated gamma and two-step exponential distributions. The resulting fit parameters are shown in figure 4.8. With the tubulin data we observe little jumps in the resulting fit parameters. They stem from a removal of one or several catastrophe times from the whole distribution. Thus, for $t_x < 10$ s not a single catastrophe time is discarded. The fact that the fit results change nonetheless is a result of the truncation.

In general, we do not detect significant changes in the fit parameters with the tubulin data. When the EBs are present the number of reaction steps goes slightly down, and of course with it, the time scale goes up. This is an evidence that we made an error in determining the short catastrophe times, albeit small. The times determined by the two-step exponential fit change less as the fit is less sensitive to short times.

A truncation t_x from 0 to 20 s is, however, a quite large range and discards at the lower limit too little and at the upper limit of 20 s more data than necessary. To decrease the range we choose a truncation parameter t_x based on a reasonable estimate for the error in determining short events. As mentioned before we could not determine MTs shorter than 3 pixels. With a time-lapse interval of, in average, 3 s with a standard deviation of 1 s we therefore limit the truncation parameter to 6-12 s. The average fit results for this interval can be found in table 4.1.

4.2.5 Simulating gamma and two-step exponential distributions

We proposed four possible mechanisms for catastrophes: multi-step reactions with same rates (gamma and parallel multistep exponential distribution) and two-step reactions with two different rates ((parallel) two-step exponential distribution). Which of the four distributions explains the data better? A priori we cannot make a differentiation. Consequently, to answer this question and to understand the accuracy of fits to the short time scales we simulated gamma and two-step exponential processes. We choose the parameters such that the distributions looked similar

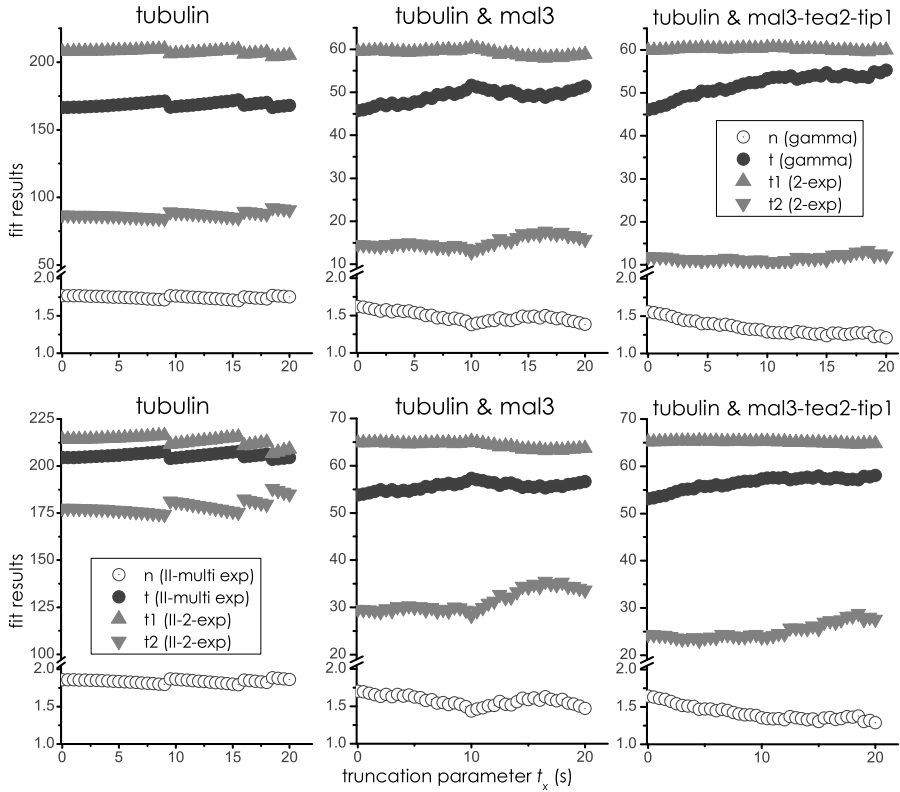


Figure 4.8: Catastrophes of free MTs corrected at short times: fit results. Due to the difficulty and possible error in detecting short events catastrophe times were discarded below a truncation threshold t_x . The remaining data was fitted with **a.** left-truncated gamma and two-step exponential distributions or with **b.** left-truncated parallel gamma and left-truncated parallel two-step distributions. Gamma distributions are more sensitive to the short events. The jumps in the case of pure tubulin happen when one or several complete catastrophe events were discarded. The most reasonable truncation interval is $t_x=6$ to 12 s corresponding to 3-4 pixels.

to our real data. For that reason we also choose the number of steps to be $n=1.5$, though a non-integer does not represent a "step". We generated $N=200, 1000$ or 10^4 random numbers from a gamma distribution and from the sum of two exponentials. After discarding numbers below t_x we fitted the remaining ones with truncated distributions. The truncation parameter t_x was varied between 0 to $t_x=20$ s in half-second steps (as explained above).

As shown in figure 4.9 with "only" 200 random numbers the truncation fits vary. The reason is that the remaining data after the truncation, so the tail of the distribution is still too noisy to retrieve always the same gamma distribution. With 10^4 numbers statistics improved so that, even after discarding a few numbers, the remaining tail of the distributions is much clearer. As a result, the truncation fits can more reliably find the underlying distribution and fit results vary less. (For better overview we do not show the confidence intervals. As expected, they decrease with improved statistics.) We can conclude that far more than 200 data points are needed to determine the number of steps and the time scales of a reaction reliably. Therefore, and that holds especially for the tubulin data with 222 catastrophe events, the averaging over fits in the truncation range $t_x=6$ to 12 s improves the reliability of fit results.

Also visible from figure 4.9, the results are influenced by the truncation, especially for $N=200$. Displaying bigger variations in the fits the gamma pdf is more sensitive to the truncation. Simultaneously it means that the gamma pdf is more sensitive to the crucial short times (especially when the data is generated from two-step exponentials). On the other hand, the two-step exponential cannot easily accommodate changes at the short times which is reflected by the little change of fit parameters during the range of truncations. Therefore we can say that it is less sensitive to the short times. Does the variation in fit parameters mean that the gamma distribution is not the adequate distribution to describe our data? Or does the lack of variation, or in other words, the lack of adaptivity in the two-step exponential case mean that

model	parameter	tubulin	tubulin & mal3	tubulin & mal3-tea2-tip1
gamma	\bar{n}	1.74 [1.42-2.06]	1.44 [1.27-1.62]	1.32 [1.17-1.48]
gamma	$\bar{\tau}$	169.1 [133.9-204.2]	50.1 [44.4-55.7]	52.4 [46.7-58.1]
2-exp	$\bar{\tau}_1$	208.2 [161.3-293.7]	59.8 [55.1-65.5]	60.4 [56.4-65.0]
2-exp	$\bar{\tau}_2$	86.6 [52.8-240.8]	14.0 [10.7-20.4]	11.0 [8.4-16.0]
-multi exp	\bar{n}	1.83 [1.45-2.22]	1.52 [1.31-1.73]	1.39 [1.21-1.58]
-multi exp	$\bar{\tau}$	206 [174.4-237.6]	56.3 [51.8-60.8]	56.9 [52.5-61.2]
-2-exp	$\bar{\tau}_1$	214.2 [85.8-342.6]	64.8 [59.4-70.2]	65.3 [61-69.5]
-2-exp	$\bar{\tau}_2$	177.5 [36.2-318.8]	29.7 [22.8-36.7]	24.1 [18.7-29.6]

Table 4.1: Effect of EBs on the catastrophe process. Catastrophe times were fitted with truncated gamma, truncated two-step exponential (2-exp), truncated parallel multistep exponential (||-multi exp) and truncated parallel two-step exponential (||-2-exp) distributions. Mean fit results are shown for truncations between $t_x=6-12$ pixels with 95% confidence interval in square brackets.

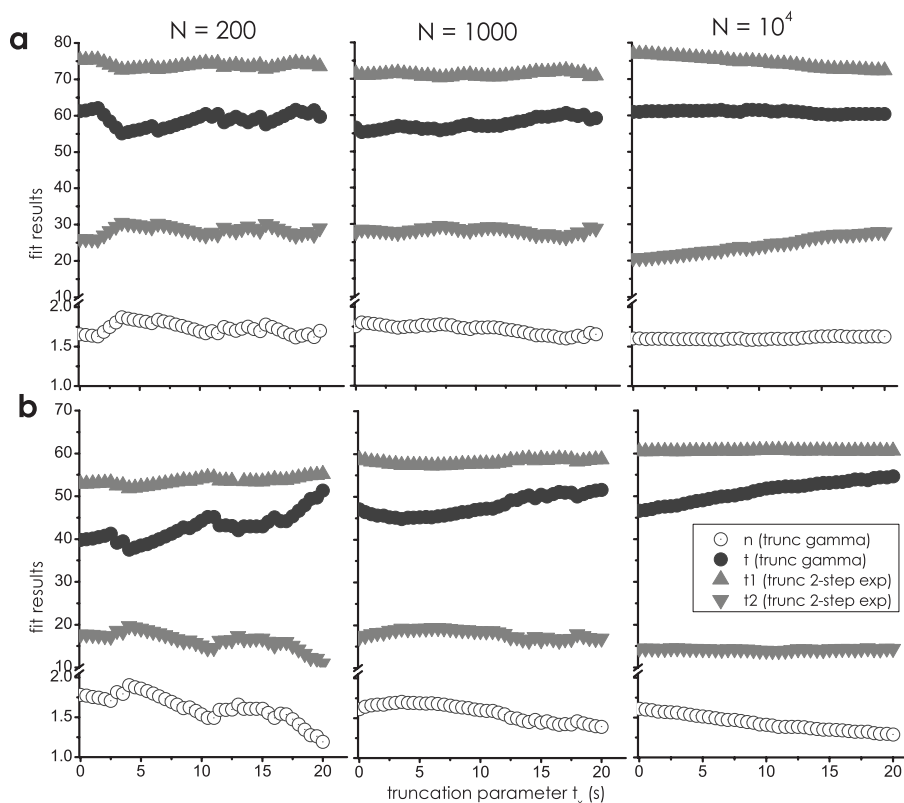


Figure 4.9: Fit results of simulated distributions. N random numbers were generated from **a.** a gamma distribution with $n=1.5$ and $\tau=60$ s or from **b.** a two-step exponential distribution with $\tau_1=15$ s and $\tau_2=60$ s. Afterwards the unbinned data was fitted with truncated gamma and two-step exponential distributions. Here, the fit results are shown.

it does not represent our data? No matter whether the random numbers are generated from a gamma or two-step exponential distribution we cannot clearly determine which fit is better, even with $N=10^4$. That means that in our case both gamma and two-step exponential distributions describe the data equally well.

In these simulations we focused only on the sequential-step reactions. However, since fitting with truncated distributions gave similar results for both sequential- and parallel-step reactions we believe to not gain more information by simulations with parallel-step reactions. Consequently, it means that we cannot differentiate whether our data is best described by parallel or sequential-step reactions.

4.3 Discussion

Our data provides insight into the events leading to a transition of MTs from assembly to disassembly. By TIRF microscopy we determined the duration MTs spend in a growing phase. To determine the underlying kinetics we fitted our data with different distributions. Since it is experimentally hard to correctly detect the short events we removed, before fitting, all data below a threshold t_x . Taking this into account, we fitted with probability density functions of truncated distributions whose total probability integrates to one between t_x and infinity. For MTs grown from pure tubulin the truncated gamma distribution suggests $n=1.7\pm 0.3$ (95% confidence interval (CI)) necessary "steps" until catastrophe. We also fitted with a two-sequential-step exponential which does not constrain the time constants between the steps to be of the same magnitude. It yielded timescales of ~ 200 s and ~ 90 s. Further, we allowed the steps until catastrophe to happen simultaneously. With both the parallel gamma and parallel two-step exponential distribution we obtained results similar to those from the sequential-step distributions (except that the shorter timescale of the two-step exponential distribution approximately doubled). Conclusively, we can say that we measure (maximum) two steps until catastrophe. Within our error bars we cannot differentiate whether our data is (parallel) gamma or two-step exponentially distributed.

Gardner et al. [Gardner et al., 2011b] previously measured catastrophe times of green-fluorescent MTs grown from red-fluorescent seeds using TIRF microscopy. This data was fitted with a gamma distribution. Contrary to our results, the authors found catastrophes to happen in two to three steps (depending on the tubulin concentration). Though using lower frame rates (10-20 s) and thus only counting events longer than 45 s they claim that they do not miss the short events. When they shift the fit distribution by 4.5 pixels (a method comparable to our "seed-shift" method) they still do not come close to an exponential function. Considering that their time scale for the completion of one step is in the order of a few hundred seconds, it seems indeed unlikely that the high number of steps is purely a results of missing short events. However, the authors only consider a gamma distribution. We can describe our data also with two-sequential-step exponential or parallel exponential distributions. Similarly, their data might also be represented by a two- or three-step exponential or by a parallel reaction scheme.

What then, tips the tip? If fitting with a gamma distribution is correct, we need two presumably similar processes with the same lifetimes. Gardner et al. [Gardner et al., 2011b] come up with different scenarios: the collection of two protofilaments lacking a GTP cap or the accumulation of structural "defects" like protofilament mismatch or protofilament number. Computational modelling by Margolin et al. [Margolin et al., 2012] showed that the probability for catastrophe is indeed increased if an uncapped protofilament is surrounded by capped long protruding protofilaments. However, it has not been shown that two or three such "gaps" induce the transition to shrinkage. Furthermore, the gamma distribution implies that the MT needs to "remember" the process until a catastrophe. Regarding the "gap" as one event leading to catastrophe it is hard to imagine how such an

uncapped protofilament would not bind a GTP-tubulin until the appearance of the second gap. Likely, changes in protofilament number have been recorded in the MT lattice but it did not seem to be a necessity for catastrophe [Chretien et al., 1992, Chretien et al., 1995].

The two-step exponential model can be realised by two different underlying processes. The MT could accumulate a "defect" which triggers the formation of another "defect" and consequently catastrophe. Those defects could be realised by two different processes, but they could also be of the same nature. Brun et al. [Brun et al., 2009] show in their theoretical paper where a two-step catastrophe after dilution is explained by the hydrolysis of two longitudinally but not laterally adjacent GTPs. In this case each hydrolysis is a sequential step and both steps are of the same nature. However, only after a sudden dilution does this model come up with waiting times in the catastrophe distribution. During growth, the simultaneous hydrolysis and arrival of new subunits produces a narrow peaked, almost exponential distribution and thus cannot explain our data.

To get a better understanding of the catastrophe process it is important to consider also MT catastrophes in the presence of mal3 (and tea2 and tip1). Fitting the EB-data with a gamma or a parallel multistep exponential distribution suggests ~ 1.4 steps until catastrophe with a catastrophe time of ~ 50 s. The (parallel) two-step distributions still yield a long and a short lifetime of ~ 60 s and 10-15 s, while the shorter timescale is approximately doubled with the parallel two-step exponential distribution.

Obviously, the main effect of the EBs is the reduction in catastrophe lifetimes (3-9x). As already mentioned in chapter 3 on page 33 and shown in figure 3.7, Maurer et al. [Maurer et al., 2011, Maurer et al., 2012] suggested EB1/mal3 to be a catastrophe-promoter. Based on their experimental data they concluded that mal3 destroys its own binding site by accelerating the nucleotide transformation of tubulin from an EB1-competent to a GDP-state. The latter state then is not only unfavourable for mal3 attachment but also prone to catastrophe.

The authors [Maurer et al., 2012] also saw that the mal3 intensity, on average, began decreasing linearly about 10 s before the MT switched to depolymerisation and reached the lattice intensity a few seconds after catastrophe. Presumably at this point the EB1-binding region on the MT was depolymerised. As shown in chapter 3 we did the same measurements and came to very similar conclusions. We observed the same decrease of mal3 intensity before the onset of catastrophe lasting in total approximately 20 s. The fact that mal3 disappears before catastrophe renders the EB-binding region a stabilising cap for MTs. Thus, the loss of this region seems to be connected to catastrophes. Since this process occurs only once (disregarding a reset/backward step) it hints at the two steps until catastrophe being of different nature. This makes the (parallel) two-step exponential reaction more likely than the one described by a gamma/multistep distribution. As mentioned, the mal3 intensity-measurements (chapter 3) showed us that the step prior to catastrophe is connected to the transformation of mal3 binding sites and the loss of mal3. We determined this step before catastrophe to be in the order of 20 s which agrees very well to the 15 s we measured for the short-timescale with the two-step exponential

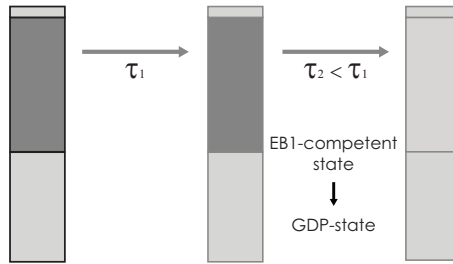


Figure 4.10: The MT transitions to catastrophe. **a.** An intact MT experiences a catastrophe-promoting event with a relatively long, random time scale. We do not know much about the nature of this event. **b.** The MT, now in an intermediate state, experiences the second catastrophe-promoting event after a random, but shorter time scale. The second event can occur sequential or simultaneous to the first step. It is connected to the nucleotide transition of tubulin from the EB1-competent state into the GDP-state which happens much faster than the step time τ_1 . If mal3 was present in the solution it disassociated here from the MT. **c.** After the accomplishment of two random steps the MT undergoes catastrophe and shrinks.

distribution. Also, the parallel two-step exponential comes close. Contrary, it does not agree with the fit results from the gamma/multistep distribution, once more making two processes occurring with the same rate unlikely. We thus envision the transition to catastrophe to occur with a long termed step which is followed or accompanied by a short-timescale step, see figure 4.10. At this moment we do not know much about the nature of the long-term step. During the short-timescale step the tubulin dimers in the MT tip transform from the EB1-competent state into the GDP-state which goes along with the loss of mal3 binding.

Finally, we want to remark on two topics which are though secondary to our research on the catastrophe process. First, it has been shown that *in vivo* a mal3-RNAi leads to shortened MTs indicating it as an essential factor in preventing cytoplasmic catastrophes [Busch and Brunner, 2004]. Our data shows an opposing effect: in the presence of mal3 free catastrophes occurred more often. Here, it is crucial to consider that with a mal3 deletion all associated binding partner loose or alter their function. This leaves the possibility of other factors than the three here-mentioned EBs to modulate catastrophes. Contrary, in our case, we really compare behaviour in the absence and presence of mal3.

Second, as shown in figure 4.3 and published previously [Komarova et al., 2009, Vitre et al., 2008, Katsuki et al., 2009], EBs do not only promote catastrophes but in general, affect dynamic instability parameters. For how they increase the net incorporation of tubulin subunits to the MT end different mechanisms can be imagined: (a) by copolymerisation of tubulin with mal3, (b) recruitment of tubulin to the MT by bound mal3, (c) by promoting the formation of lateral bonds between protofilaments, or (d) by promoting longitudinal bonds between tubulin dimers. Copolymerisation has not been favoured in the literature for two reasons. Gel filtration experiments revealed little interaction between tubulin and mal3 [Bieling

et al., 2007]. Furthermore, individual mal3 molecules turn over rapidly at the MT end while the overall mal3 decoration time at the MT end takes long [Bieling et al., 2007, Maurer et al., 2011]. Together with [Maurer et al., 2012] this is an indicator that mal3 recognises an existing tubulin configuration. Considering that mal3 needs four tubulin dimers to bind, it cannot bind to the terminal dimers [Maurer et al., 2012] making it difficult to envisage the second scenario as well. On the other hand, since longitudinal bonds are formed before lateral ones [VanBuren et al., 2002, Sept et al., 2003] and mal3 needs four tubulins to bind, it might stabilise MTs by stimulating the inter-protofilament connections. Besides, mal3 could direct the dynamic subunit attachment and detachment [Gardner et al., 2011a] to a rapid and stable addition of tubulin and thus faster growth.

4.4 Methods

The experiments described here are based on previous assays as described in section 2.2.2 on page 2.2.1ff.

Sample preparation. Glass cover slips were sonicated for 30 minutes in iso-propanol, then rinsed 3x in MilliQ, sonicated for 20 minutes in 1 M KOH and rinsed 3x with MilliQ. A flow-chamber was assembled by parallely gluing two strips of parafilm between a microscope slide and a coverslip (Merck, Darmstadt, Germany). The flow chamber was functionalised and passivated with a 0.2 mg/ml mix of biotin-PLL-PEG and PLL-PEG (SurfaceSolutions, Switzerland). Residual non-specific binding sites were blocked with 0.5 mg/ml κ -casein and 1 % F-127. Stabilised, fluorescently labelled MT seeds (containing 12 % fluorescent tubulin and 18 % biotin tubulin) were attached by means of a biotin-streptavidin linker. Microtubule growth was initiated by adding MRB80 buffer (80 mM K-PIPES pH 6.8, 50 mM KCl, 4 mM MgCl₂, 1 mM GTP, 1 mM EGTA, 10 mM 2-mercaptoethanol), 0.5 mg/ml κ -casein, an oxygen scavenger system (20 mM glucose, 200 μ g/ml glucose-oxidase, 400 μ g/ml catalase), 15 μ M tubulin of which 5-7 % was labelled with rhodamine, HiLyte488 or HiLyte647 (Cytoskeleton, Denver, CO, USA). Optionally, end-binding proteins (EBs) were added: either 200 nM mal3-Alexa488 alone or together with 8 nM tea2 and 50 nM tip1 (in the latter case also 2 mM ATP was added to the MRB80 buffer). EBs were purified as described in [Bieling et al., 2007]. Unless stated otherwise, chemical reagents were obtained from Sigma-Aldrich (Saint-Louis, MO, USA).

Imaging method. The sample was imaged in an inverted Ti-Nikon Eclipse microscope (Nikon, Tokyo, Japan) using total internal reflection fluorescence (TIRF) microscopy equipped with a 1.49 NA, 100x oil immersion objective. Single tiff-images were recorded using a Calypso 491 nm diode laser (Cobolt, Solna, Sweden), a Jive 561 nm diode laser (Cobolt) and a 635 nm "56 RCS-004" diode laser (Melles Griot, Albuquerque, NM, USA) imaged with a Roper Scientific Coolsnap HQ CCD-camera (Photometrics, Tucson, AZ, USA) and saved to disk with MetaMorph software (Molecular Devices, Sunnyvale, CA, USA), at time-lapse intervals between 0.2 and 5 s, at typical exposure times of 200-250 ms. After mounting the sample on the microscope stage imaging started after a 5 minute equilibration time. Imaging time was kept below 2 hours (average of 1 hour) at a constant temperature of $25 \pm 0.5^\circ\text{C}$ which was maintained by running heated/cooled water through a sleeve around the objective. Simultaneously, the water temperature was adjusted by Peltier elements to a

temperature based on a sensor within the sleeve in proximity to the sample.

Data analysis. Tiff-stacks were background-subtracted and bleach-corrected (macro developed by J. Rietdorf, EMBL Heidelberg, Germany) in Fiji (based on ImageJ which was developed by Wayne Rasband, NIH in Bethesda, MD, USA). Growth trajectories of single MTs were displayed in kymographs where straight lines were fitted to each growth or shrinkage phase by hand/mouse. A phase was defined as continuous growth or shrinkage at constant speed. Free growth and shrinkage was differentiated by angle of the line fit. Coordinates of the line fits were processed in Matlab (Mathworks, Natick, NA, USA) by a custom-made software to determine dynamic instability parameters per sample. Average polymerisation speeds were defined as the average over all events weighted with the time span of the individual event:

$$v_{\text{sample}} = \frac{\sum v_i t_i}{\sum t_i} \quad (4.6)$$

The error was the weighted standard deviation which reflects the intrinsic variations of dynamic instability [Gildersleeve et al., 1992]:

$$\sigma_{\text{sample}} = \sqrt{\frac{n}{n-1} \frac{\sum (v_i - v_{\text{sample}})^2 t_i}{\sum t_i}} \quad (4.7)$$

where i denotes an individual event, v_i the speed (growth or shrinkage) of the event i , t_i is the time spanned by the event i , and n stands for the total number of events per sample.

For each sample, between 3-100 MTs were analysed. Samples with identical experimental conditions were grouped into a "dataset". In this case we pooled all speeds together and weighted each with its duration, analogously to equations 4.6 and 4.7.

For section 4.2.2 the catastrophe time was calculated by dividing the total time a microtubule spent in a growing (pausing) phase by the total number of observed catastrophes. The catastrophe rate was the inverse of the catastrophe time.

Fitting. All unbinned data was pooled together for each experimental condition and was used for distribution fitting. The distribution parameters were estimated and the corresponding confidence intervals given by using the maximum likelihood statistics toolbox of Matlab. The exponential distribution was fitted using the *expfit* function, for the gamma distribution we used the *gamfit* function, while all other distributions were fitted with custom functions.

Simulations. Stochastic processes were simulated in Matlab (Mathworks) in two ways. Either random numbers were generated from a gamma distribution with the number of steps n and the time constant τ set to a specific value. Otherwise they were generated from the sum of two exponential distributions with each a fixed time constant τ_1 and τ_2 . The total number of events was $N=200, 1000$ or 10^4 .

Acknowledgements

We thank Peter Bieling and Thomas Surrey for help with the protein purification of mal3, tea2 and tip1, Roland Dries for help with the imaging and Magdalena Preciado-Lopez for discussions. The work presented in this chapter was carried out as part of the EU Program AMOCROSS, as part of a "VICI" grant provided by the "Nederlandse Organisatie voor Wetenschappelijk Onderzoek (NWO)" and as

part of the research program of the "Stichting voor Fundamenteel Onderzoek der Materie (FOM)", which is financially supported by the "Nederlandse Organisatie voor Wetenschappelijk Onderzoek (NWO).

The effect of force and end-binding proteins on microtubule catastrophes



The dynamics of microtubules are crucial for their biological function. In chapters 3-4 we showed that microtubules are regulated by the end-binding proteins mal3, tea2 and tip1, as well as by forces generated when microtubules grow against cellular obstacles. However, it is unclear whether end-binding proteins qualitatively or quantitatively change the way microtubules respond to force. We therefore investigate microtubules, *in vitro*, in the presence of the end-binding protein complex mal3, tea2, tip1. Head-on forces are achieved by growing the microtubules against micro-fabricated barriers. Using total internal reflection fluorescence microscopy we show that catastrophes occur 5-10 times more frequently in the presence of the protein complex (or mal3 alone) than in its absence. In addition, the distribution of catastrophe times for stalled MTs is strongly peaked for pure tubulin, whereas it is exponentially distributed in the presence of end-binding proteins.

5.1 Introduction

The assembly of tubulin subunits into a microtubule (MT) provides energy [Hill, 1987]. When MTs polymerise against cellular objects they can therefore exert pushing forces [Hotani and Miyamoto, 1990, Fygenon et al., 1997, Inoue and Salmon, 1995, Janson et al., 2003]. This has been demonstrated, for example, on the nuclear positioning in *S.pombe* cells by MTs pushing against both cell ends [Tran et al., 2001]. On the other hand, the microtubule (MT) can generate pulling forces [Mitchison, 1988, Lombillo et al., 1995, Grishchuk et al., 2005] which has been shown during spindle positioning in mitosis [McIntosh and Pfarr, 1991, Barton and Goldstein, 1996, Tran et al., 1997]. That forces are not only used for directly organising the cell interior but also as a regulatory effect was evident from several experiments. *In vitro* MT growth against micro-fabricated barriers reduced the growth speed and increased the catastrophe frequency [Dogterom and Yurke, 1997, Janson et al., 2003, Janson and Dogterom, 2004]. Later, Tischer et al. [Tischer et al., 2009] examined the spatial dependence of MT dynamics in fission yeast cells. The authors provided evidence that MT growth speed and catastrophe time are reduced by compressive forces at the cell pole.

Still, however, little is known about the combined effect of end-binding proteins and forces. To shed light on this we use an *in vitro* assay where MTs grow against

glass barriers generating compressive forces. The MT growth buffer can be completed with the end-binding protein mal3 alone or with the combination of mal3, tea2 and tip1.

5.2 Results

We have shown in chapter 4 that we see catastrophe as a two-step process. In combination with our results from chapter 3, where we determined the disappearance of the EB-binding region as a prerequisite for catastrophe, we conclude that catastrophe is composed of a slow step followed or accompanied by a second short-term step. In chapter 3 we also examined the mal3 attachment to MTs under force and learned that mal3 unbinds when the MT encounters a barrier. What does that mean for the catastrophe process? Janson et al. [Janson and Dogterom, 2004] saw that the catastrophe time distribution for force-loaded MTs in the presence of tubulin is peaked hinting at the mechanism being altered. Whether this is the same in the presence of EBs is a question we want to address in this chapter.

We tackle this problem with an assay very similar to the one described in the previous chapters: From surface-attached stabilised seeds dynamic MTs were nucleated in three conditions: in the presence of

- tubulin
- tubulin and mal3 or
- tubulin and the three EBs, mal3, tea2 and tip1 (referred to as "mal3-tea2-tip1")

As shown in figure 3.1a-b. the microtubule seeds were, occasionally, positioned such that a dynamic MT could reach the micro-fabricated rigid barriers where they experienced compressive forces. Since only some of the MTs grew against the barriers we could compare the dynamic instability parameters of free MTs to MTs under force. (For the effect of end-binding proteins on free MTs refer to chapter 4).

5.2.1 MTs under force

In figure 3.2 and section 3.2.1 we introduced the types of barrier interactions. We observed two types: "stalling MTs" and "sliding MTs". To decrease the influence of growth speed on catastrophes we only looked at stalling MTs. Furthermore, we are interested in MTs under high load which is the case with stalling MTs. Yet, since the exact magnitude of force was unknown we could only estimate it by plotting MT length when reaching the barrier. As shown in fig. 5.1 all MTs are in the same range of distance to the barrier and thus experience forces of like magnitude. MTs in the presence of tubulin grew slower and switched to shrinkage before they reached too distant barriers (5 μm away). MTs in the presence of mal3 or mal3-tea2-tip1 grew longer and therefore reached barriers further than 6 μm away.

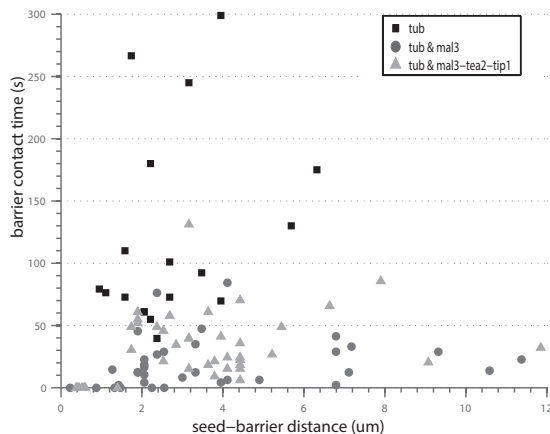


Figure 5.1: Seed-barrier distance for stalling MTs. The length of a stalling, non-buckling dynamic MT indicates the exerted force. The shorter the MT, the higher the force, since longer MTs can release force by buckling [Gittes et al., 1996].

5.2.2 Catastrophe time distributions for MTs under force

For each MT that stalled at the barrier we created kymographs (space-time plots) from the recorded time-lapse TIRF images (see fig. 3.1d-f). In these kymographs we tracked the MT end by hand, where we assigned a straight line to a continuous growth or shrinkage phase, as shown in figure 3.2a. MTs stalling at the barrier contained a free growth part and a barrier-contact part. To avoid confusion we refer to the catastrophe time for MTs under force as "barrier-contact time". We define this as the time spanned from establishment of barrier contact until catastrophe (see white vertical line in figure 3.2a.).

We plot the barrier-contact times as cumulative distribution functions (cdf) (see fig. 5.2) which does not involve binning and therefore shows every measurement. In general, the cumulative distribution at time t indicates the probability of transition to catastrophe in the time span $0 - t$. To determine the mechanism of MT catastrophes under force we fitted the experimental data with two distributions, see also figure 4.5 and pages 41ff.:

- The gamma distribution represents multi-step reactions and has been used to describe MT catastrophes [Rice, 1995, Floyd et al., 2010, Gardner et al., 2011b]. It represents a process with multiple steps n where each step happens with an equal characteristic rate $k = \tau^{-1}$. Its cumulative distribution function (cdf) displays a lag phase at the origin.
- The exponential distribution describes a first-order processes implying that catastrophe does not depend on the MT's history. The exponential distribution describes the catastrophe of an intact MT with rate k . The exponential is a special case of a gamma distribution with one step. Exponential cdfs are characterised by a linear slope at the origin.

Looking at figure 5.2 it is clear that the exponential distribution does not fit the tubulin data well. Considering especially the offset at the short times we can discard the barrier contact times to be composed of one step, as shown previously [Janson et al., 2003]. This suggests that multiple steps are necessary until catastrophe. Indeed, a fit with a gamma function reveals approximately three necessary steps

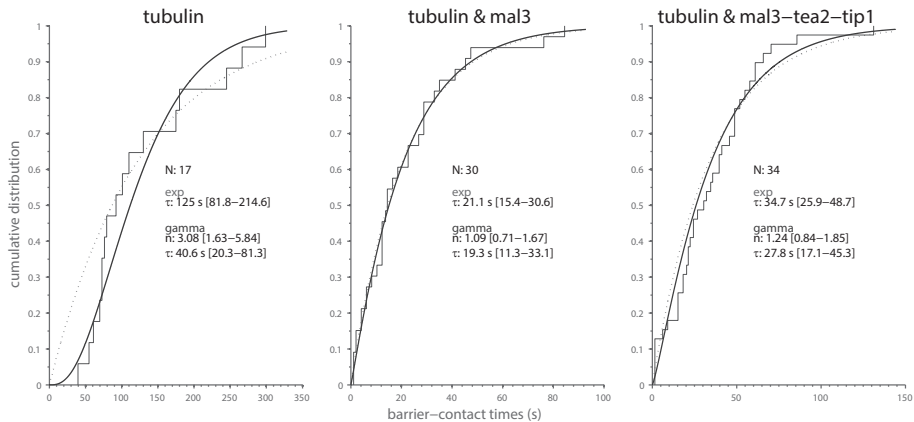


Figure 5.2: Histograms of barrier-contact times and fit results. Barrier-contact times are fitted with an exponential (dotted line) and a gamma distribution (continuous line). Fit results are displayed in the figure with 95% confidence intervals in square brackets. In the presence of EBs, some MTs underwent a catastrophe in between reaching the barrier and recording of the next frame. We assigned here, as an example, to those events a barrier-contact time of 1/2 the average time-lapse interval.

until catastrophe with a time per step of ~ 40 s. For comparison, when fitting catastrophe times of free MTs with a truncated gamma distribution (see chapter 4) we only found 1.7 ± 0.3 steps, but a time scale of 169 ± 35 s (with 95% confidence intervals). Nevertheless, to be certain about the exact number of steps and the exact timescale for catastrophes under force we would need better statistics. Therefore our main conclusion should be that a catastrophe at the barrier is a process involving several intermediate steps and that this process is faster than the catastrophe process of free MTs.

Free MTs in the presence of end-binding proteins (EBs) transition significantly faster to a shortening state as published previously [Munteanu, 2008, Vitre et al., 2008, Maurer et al., 2011] and shown in section 4.2.3. This raises the question: how do EBs change the catastrophe mechanism of MTs under force? We therefore repeated the experiments with dynamic MTs under force, now in the presence of the end-binding proteins mal3, tea2, tip1 or in the presence of mal3 alone.

In the presence of EBs MTs occasionally underwent a catastrophe when reaching the barrier (referred to as "immediate" events). In these cases it was experimentally hard to determine whether the MT touched the barrier or not. The reason is that TIRF microscopy is not very reliable in terms of absolute fluorescent intensity due to reflections at the barrier. Consequently, we could not clearly determine the bulk-barrier interface (± 1 pixel). This improved when a MT stalled or repeatedly underwent a catastrophe at the barrier. To determine which of these MTs are unjustly considered to touch the barrier we calculated the catastrophe probability of each of these MTs. We first assumed that these MTs are free. Considering

model	parameter	tubulin	tubulin & mal3	tubulin & mal3-tea2-tip1
exp	τ_{lb}	/	21.0 [15.3-30.5]	34.5 [25.8-48.5]
	τ_{ub}	/	21.2 [15.5-30.7]	34.8 [26.1-49]
gamma	n_{lb}	3.08 [1.63-5.84]	0.88 [0.58-1.34]	0.89 [0.61-1.32]
	n_{ub}	3.08 [1.63-5.84]	1.21 [0.79-1.87]	1.5 [1-2.24]
	τ_{lb}	40.6 [20.3-81.3]	23.9 [13.7-41.6]	38.6 [23.2-64.2]
	τ_{ub}	40.6 [20.3-81.3]	17.5 [10.3-29.7]	23.3 [14.4-37.5]

Table 5.1: Effect of EBs on the catastrophe process. When MTs underwent a catastrophe after reaching the barrier and before the next image was recorded we did not know the exact barrier-contact time. In this case we could only give an upper bound (average framerate) and lower bound (1/10 of the average framerate). We then fitted the barrier-contact times with exponential and gamma distributions. Here we show the fit parameters where lb refers to lower and ub to upper bound and the 95% confidence interval in square brackets. (The results of fitting catastrophe times of free MTs are presented on page 47).

only their age we then calculated the catastrophe probability in the interval [MT age \pm the time the MT needs to grow one pixel]. For this we used the truncated gamma distribution and the corresponding parameter estimates determined for free MTs (see p. 47). It turns out that the probability for catastrophe is so small that essentially all the events are considered to happen at the barrier.

Overall, we only observe stalling and sliding MTs at the barrier. However, if a MT undergoes a catastrophe as soon as it reaches the barrier we do not know whether we should count it into the stalling or sliding group. It would be wrong to consider all these "immediate" catastrophe events a priori as stalling. We therefore calculated the fraction of "real" stalling versus "real" sliding MTs and then added the same fraction of immediate catastrophe events to the stalling group.

Having settled on the total number of stalling MTs we still do not know the barrier-contact times of the short events. Similarly to the case of free MTs it is experimentally hard to correctly detect the short events. Since we do not know exactly the barrier-contact time we can only determine an upper (the average framerate) and lower bound where the latter should tend towards zero and was set for computational reasons to 1/10 of the average framerate. Figure 5.2 (middle and right) shows the cumulative distribution plot of barrier-events where the immediate events are set to half the average framerate, as an example. In contrast to the fit for pure tubulin, these fits display a linear slope for very short times and thus are characteristic for a first-order process. Indeed, the gamma function reveals a single step until catastrophe with an approximately 3-times shorter time scale than for free MTs.

We did not fit the barrier-contact times with other distributions since the number of events is too low to allow for interpretation from different models. On the other hand, we consider it very likely that other distributions will also suggest (approximately) one step for the process. The physical interpretations would in

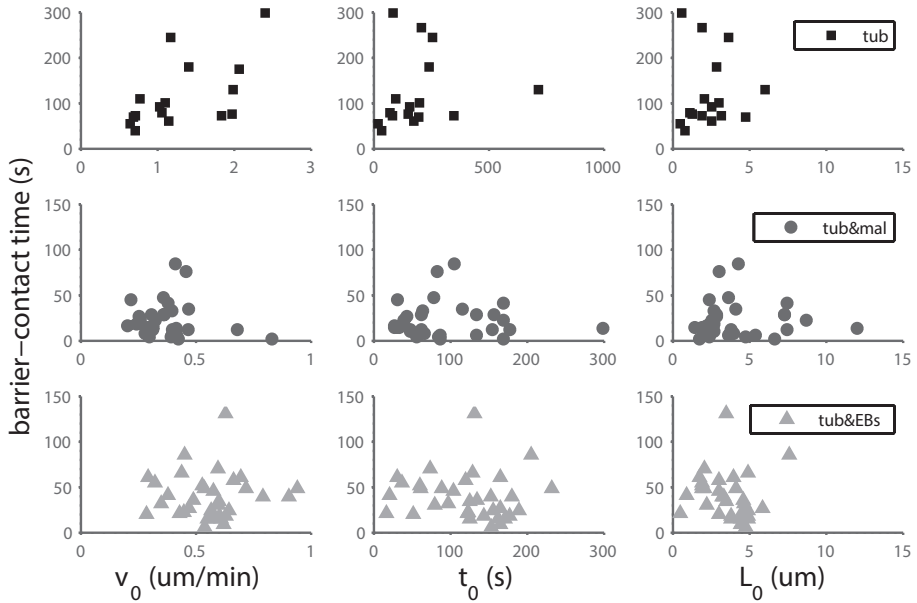


Figure 5.3: Dependence of barrier-contact times on MT parameters before reaching the barrier. Each point represents an individual stalling event for the three experimental conditions of pure tubulin (upper row), tubulin & mal3 (middle row) and tubulin & mal3-tea2-tip1 (lower row). **left column.** Barrier-contact times are plotted versus growth speed v_0 at which MT approached the barrier, **middle column.** versus MT "age" t_0 and **right column.** MT length L_0 when reaching the barrier.

this case be the same.

We showed in chapter 4 that the catastrophe time of free MTs is dependent on their growth time (their age). In our analysis of barrier-contact times we did not take into account the time the MT was growing freely. Contrary, we considered the MT upon reaching the barrier to have no age. That is because we think that the free catastrophes and barrier-contact times could be seen as two independent processes. Indeed, the time until catastrophe at the barrier is much shorter than for free MTs making the former the dominant step. Therefore, we assume not to have a big influence of MT age on barrier-contact times. Further, a plot of MT growth time vs. barrier-contact time did not show a correlation, see figure 5.3. Neither did we recognise an influence of MT length or pre-barrier growth speed on barrier-contact times, as shown previously [Janson and Dogterom, 2004].

5.3 Discussion

Our data provides insight into the events leading to a transition of MTs under force from growth and stalling to a shortening state. By TIRF microscopy we determined the duration MTs spend in contact with a barrier. To get a better insight into the catastrophe process we fitted our data with exponential and gamma distributions. MTs grown in the presence of tubulin alone evolved in at least two independent steps before the onset of shrinking. This is not unexpected: the same peaked distribution after reaching the barrier has been shown before [Janson and Dogterom, 2004]. Janson et al. [Janson, 2002, Janson et al., 2003] showed that catastrophe time depends on the tubulin on-rate which can be decreased by both force and tubulin concentration. We can thus assume that also here the force decreases the growth speed of MTs under force. Specifically, we do not have a good explanation for the strongly peaked distribution of catastrophe times at this moment. To understand how force affects the catastrophe process of MTs grown from pure tubulin further experiments are hence necessary.

In the presence of a force and of mal3 or mal3-tea2-tip1, both the exponential and the gamma distribution fit well, where the latter suggests 0.8-1.5 necessary steps until catastrophe (error margin as we cannot precisely determine the catastrophe time of the very short events, see above). This makes catastrophe under force in the presence of EBs effectively a Poissonian process. Our findings of free MTs in the presence of EBs show that catastrophe happens in two steps with a step of ~60 s followed up or accompanied by a shorter step of ~15 s or 20-30 s, respectively (see section 4.2.4). We reasoned that the shorter step must be defined by the random occurrence of the tubulin transformational change. As presented in figure 4.10 on page 53 this change comprises the nucleotide change from the EB1-competent state into the for mal3 unfavoured GDP-state. The duration of this step agrees very well with the time scale obtained from the fit of barrier-contact times. Therefore, we believe that the single step under force in the presence of EBs also comprehends the nucleotide transformation. Consequently, the first step, observed only for free MTs, must be so much shortened under force and with EBs that it appears to happen immediately. In the case of free MTs, the accomplishment of the first step puts MTs into a state where they could catastrophe after one more (the second random) destabilizing event. The omission of this first step in the case of force-loaded MTs renders them directly after barrier contact "ready" for catastrophe.

Previous publications reported that catastrophe occurred more often at the cell periphery than in the cytoplasm [Komarova et al., 2002, Brunner and Nurse, 2000b, Drummond and Cross, 2000, Tran et al., 2001]. More specifically, the mal3 and tip1 RNAis by Brunner and Busch [Brunner and Nurse, 2000b, Busch and Brunner, 2004] might suggest that tip1 protects against the small forces at the cell periphery (not at the cell ends). Yet, this does not agree with our data. Within errorbars it seems rather that tip1 gives a slight protection against catastrophes both on free and loaded MTs. The difference between *in vitro* and *in vivo* results most probably stems from other, yet presently unknown, binding partners of EB1

in vivo [Komarova et al., 2009].

5.4 Methods

Sample preparation. Barriers made of SiO (glass) were micro-fabricated on glass cover slips as described in chapter 2.2.1. Afterwards the cover slips were rinsed with iso-propanol and then rinsed 3x with MilliQ. A flowchamber was assembled by parallelly gluing two strips of parafilm between a microscope slide and a coverslip (Merck, Darmstadt, Germany). The flow chamber was functionalised and passivated with a 0.2 mg/ml mix of biotin-PLL-PEG and PLL-PEG (SurfaceSolutions, Switzerland). Residual non-specific binding sites were blocked with 0.5 mg/ml κ -casein and 1 % F-127. Stabilised, fluorescently labelled MT seeds (containing 12 % fluorescent tubulin and 18 % biotin tubulin) were attached by means of a biotin-streptavidin linker. Microtubule growth was initiated by adding MRB80 buffer (80 mM K-PIPES pH 6.8, 50 mM KCl, 4 mM MgCl₂, 1 mM GTP, 1 mM EGTA, 10 mM 2-mercaptoethanol), 0.5 mg/ml κ -casein, an oxygen scavenger system (20 mM glucose, 200 μ g/ml glucose-oxidase, 400 ug/ml catalase), 15 μ M tubulin of which 5-7 % was labelled with rhodamine, HiLyte488 or HiLyte647 (Cytoskeleton, Denver, CO, USA). Optionally, end-binding proteins (EBs) were added: either 200 nM mal3-Alexa488 alone or together with 8 nM tea2 and 50 nM tip1 (in the latter case also 2 mM ATP was added to the MRB80 buffer). EBs were purified as described in [Bieling et al., 2007]. Unless stated otherwise, chemical reagents were obtained from Sigma-Aldrich (Saint-Louis, MO, USA).

Imaging method. The sample was imaged in an inverted Ti-Nikon Eclipse microscope (Nikon, Tokyo, Japan) using total internal reflection fluorescence (TIRF) microscopy equipped with a 1.49 NA, 100x oil immersion objective. Single tiff-images were recorded using a Calypso 491 nm diode laser (Cobolt, Solna, Sweden), a Jive 561 nm diode laser (Cobolt) and a 635 nm "56 RCS-004" diode laser (Melles Griot, Albuquerque, NM, USA) imaged with a Roper Scientific Coolsnap HQ CCD-camera (Photometrics, Tucson, AZ, USA) and saved to disk with MetaMorph software (Molecular Devices, Sunnyvale, CA, USA), at time-lapse intervals between 0.2 and 5 s, at typical exposure times of 200-250 ms. After mounting the sample on the microscope stage imaging started after a 5 minute equilibration time. Imaging time was kept below 2 hours (average of 1 hour) at a constant temperature of $25 \pm 0.5^\circ\text{C}$ which was maintained by running heated/cooled water through a sleeve around the objective. Simultaneously, the water temperature was adjusted by Peltier elements to a temperature based on a sensor within the sleeve in proximity to the sample.

Data analysis. Tiff-stacks were background-subtracted and bleach-corrected (macro developed by J. Rietdorf, EMBL Heidelberg, Germany) in Fiji (based on ImageJ which was developed by Wayne Rasband, NIH in Bethesda, MD, USA). Growth trajectories of single MTs were displayed in kymographs where straight lines were fitted to each growth or shrinkage phase by hand/mouse. A phase was defined as continuous growth or shrinkage at constant speed. We define the barrier-contact time as the time spanned from reaching the barrier until catastrophe. Coordinates of the line fits were processed in Matlab (Mathworks, Natick, MA, USA) by a custom-made software to determine dynamic instability parameters per sample.

Fitting. All unbinned data was pooled together for each experimental condition and was used for distribution fitting. The distribution parameters were estimated and the corres-

ponding confidence intervals given by using the maximum likelihood statistics toolbox of Matlab. The exponential distribution was fitted using the *exffit* function and for the gamma distribution we used the *gamfit* function.

Acknowledgements

We are grateful for the help and advice with the micro-fabrication received from Chris Rétif and Hans Zeilemaker. Further, we thank Peter Bieling and Thomas Surrey for help with the protein purification of *mal3*, *tea2* and *tip1*. We highly appreciate the help of Roland Dries with the imaging. The work presented in this chapter was carried out as part of the EU Program AMOCROSS, as part of a "VICI" grant provided by the "Nederlandse Organisatie voor Wetenschappelijk Onderzoek (NWO)" and as part of the research program of the "Stichting voor Fundamenteel Onderzoek der Materie (FOM)", which is financially supported by the "Nederlandse Organisatie voor Wetenschappelijk Onderzoek (NWO)".

The force–growth speed relationship of microtubules in the presence of end-binding proteins



In chapter 5 we measured the catastrophe time of microtubules under force. In those experiments we lacked information about the growth speed which has been shown to influence the microtubule lifetime. Here, we want to get a closer insight into the mechanism underlying catastrophe and its relation to the microtubule growth speed. For this we use an optical tweezers approach which allows us to measure force generation with high temporal and spatial resolution. By combining this *in vitro* assay with force-feedback we can measure at predefined constant loads. During an experiment, microtubules, nucleated from trapped bead-axoneme templates, are directed against rigid barriers in the absence or presence of the fission yeast end-binding proteins *mal3*, *tea2* and *tip1*. Our data shows that microtubule growth speed decreases with an increasing force both in the absence and presence of the end-binding proteins. Surprisingly, we find that the growth speed-force relationship looks alike in the two cases. We explain this with a loss of end-binding proteins with the onset of force and a subsequent MT growth characterised by the absence of proteins.

6.1 Introduction

The regulating effect of force was demonstrated *in vivo* in animal cells where the catastrophe frequency of microtubules (MTs) was increased at the cell's cortex [Komarova et al., 2002, Mimori-Kiyosue et al., 2005]. An explanation for an increased catastrophe frequency under force was provided by imaging of *in vitro* microtubules grown from pure tubulin against rigid barriers [Janson and Dogterom, 2004]. Growth under force resulted in buckling microtubules whose shape gave information about the generated force and the growth speed. By careful analysis, combined with data obtained from free MTs in different tubulin concentrations, the authors identified a linear scaling of catastrophe time with microtubule growth speed. Conclusively, the microtubule can increase the probability to catastrophe by a reduced on-rate of tubulin subunits, by force or by tubulin concentration.

We have shown in the previous chapters that end-binding proteins (EBs) increase the catastrophe frequency of microtubules. Under force this catastrophe mechanism was accelerated in comparison to freely grown MTs and was altered with respect to force-loaded MTs grown from pure tubulin. Here, we wonder whether this

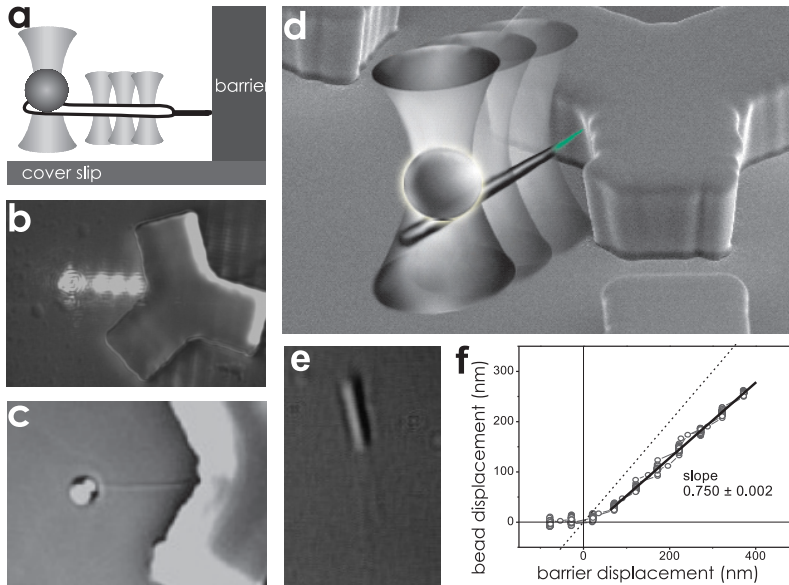


Figure 6.1: The optical tweezers setup. **a.** An axoneme (bundle of MTs, white with black outline) is attached to a trapped bead. By using a time-shared "keyhole" trap where the laser scans a line and traps the bead with higher frequency than the axoneme we can direct the axoneme against a micro-fabricated rigid barrier. Upon nucleation and growth of a MT (black), the bead is pushed out of the trap. We can measure this displacement and calculate a force from it. **b.** Top view DIC-image of the laser positions (white circles) and triangular star-shaped barriers. **c.** Top-view DIC-image of the bead-axoneme construct positioned in front of a barrier. **d.** Side view (artistic and DIC) of the trapped construct directed against a barrier. **e.** High-resolution DIC image of two MTs growing from an axoneme. **f.** When the barriers are pushed against the axoneme, the bead displacement shows an initial "soft" regime of about 50 nm (see also fig. 2.4 on p.21). Afterwards, the bead displacement is linearly dependent on barrier displacement where we chose constructs with a proportionality constant of 0.3-0.5.

has something to do with a decreased tubulin on-rate.

Force generation at high resolution, the magnitude of both pushing and pulling forces and the growth speed has been measured simultaneously in various optical tweezers experiments [Kersemakers et al., 2006, Charlebois et al., 2010, Laan et al., 2012]. Here, we want to use this method to get a deeper insight into the structural and dynamic influence of forces on MT regulation by end-binding proteins. MTs are assembling against micro-fabricated barriers, and, by linking them to trapped beads, we can determine MT length changes with nanometer resolution. We examine the MTs in the presence of the fission yeast end-binding proteins mal3, tea2 and tip1.

6.2 Results

We expect that force also reduces the tubulin on-rate for MTs grown in the presence of EBs. With our experiments we want to examine how far the scaling of the force-growth speed relationship can come up for the differences observed in the catastrophe times between MTs grown in the absence and presence of EBs (see chapter 5). We hope that our results help us in quantitative understanding of the catastrophe process.

We examined force generation of dynamic MTs grown from pure tubulin, optionally in the presence of the end-binding proteins mal3, tea2 and tip1. We used a technique previously described [Kersemakers et al., 2003, Kersemakers et al., 2006, Schek and Hunt, 2005] where we direct dynamic MTs against a barrier and measure their growth with near nanometer resolution (see also chapter 2.3). In detail, an axoneme, a natural bundle of polarity-aligned MTs, is non-specifically attached to a bead. Both bead and axoneme are trapped with a time-shared optical trap where the laser scans a line along the axoneme and bead and traps the bead with higher frequency than the axoneme. As a consequence the bead experiences a 'stronger' trap and we describe the resulting pattern as "keyhole" trap. With this pattern we can easily manoeuvre the whole construct without rotation. As can be seen in figure 6.1a-d., we position the bead-axoneme construct such that one end of the axoneme points towards a micro-fabricated barrier. MT growth is then initiated by the addition of tubulin to the ambient buffer. The length increase of the MT results in pushing the axoneme and attached bead a proportional distance away from the barrier. By recording the bead position with video enhanced differential interference contrast (VE-DIC) microscopy and a live tracking routine we can determine the bead displacement with high spatial and temporal resolution. Further, we can calculate the generated force from the bead displacement.

To obtain quantitative values for MT length and force we need to know two proportionality constants. First, we measure the position fluctuations of a trapped bead (without axoneme) from which we determine the so-called trap stiffness κ [Neuman and Block, 2004]. Since the optical trap works analogously to a spring, the length displacement ΔL exerts a pushing force F onto the MT with $F = \kappa \Delta L$, where κ is the trap stiffness (Hooke's law).

The second constant stems from the non-specific attachment of axoneme to bead. We determine it by moving the barrier stepwise a known distance towards the axoneme without the presence of tubulin and thus without MTs growing from the axoneme. Meanwhile, we measure the corresponding bead displacement. Upon barrier contact the axoneme-bead attachment displays an initial "soft" regime of ~ 50 nm, where axoneme displacement hardly moves the bead (see fig 6.1f). This is followed by a linear regime in which we measure. The difference of barrier movement versus bead displacement gives us the proportionality constant. Constructs were chosen such that it was kept between $\frac{1}{3}$ - $\frac{1}{2}$.

Since we do not want the MTs to release force by buckling we keep the MTs short ($< 1 \mu\text{m}$). This is achieved by positioning the axoneme in contact with the barriers before adding tubulin and by choosing high trap stiffness.

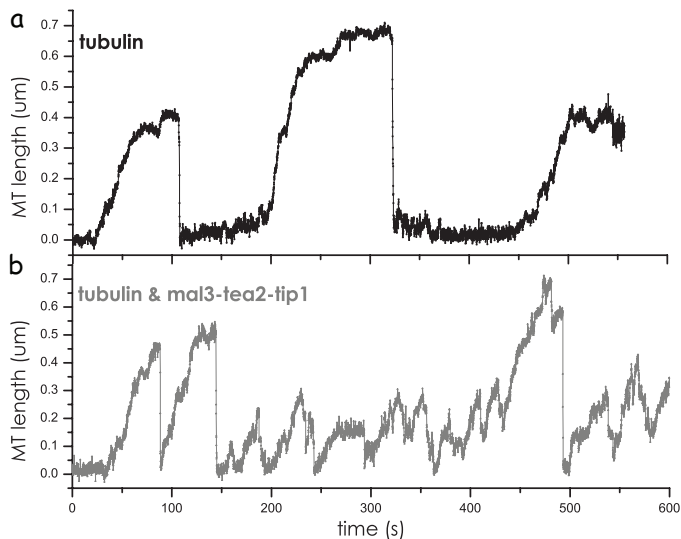


Figure 6.2: MT growth traces obtained with optical tweezers. MTs are grown from a bead-axoneme construct against a rigid barrier. MT growth results in displacement of the trapped bead from which we can deduce the MT length. Here, MT length is plotted over time in the presence of **a.** tubulin alone (black) or in the presence of **b.** tubulin with mal3, tea2 and tip1 (grey). When EBs are present MTs are more dynamic and in generally do not grow as long. This example shows twice the nucleation of a single MT after which only MT bundles are nucleated.

A priori we do not know the directionality of the axoneme. Yet, since MT plus ends assemble faster than minus ends and transition more frequently to depolymerisation [Walker et al., 1988] we could distinguish MT plus end growth. Furthermore, apparent rescues, though extremely rare under our conditions, and shrinkage in several steps were signs of multiple MTs. In general, the number of MTs nucleating from an axoneme can be set by the temperature and tubulin concentration. Since MT nucleation under force in the presence of EBs was difficult, we facilitated nucleation by a high tubulin concentration (we use $25 \mu\text{M}$ tubulin but due to dilution in the chamber we estimate the tubulin concentration to be $20 \mu\text{M}$) and temperature. This resulted occasionally in the growth of MT bundles which we analysed separately from growth traces with single MTs.

6.2.1 MT growth trajectories are more dynamic in the presence of EBs

Figure 6.2a shows a typical MT growth trace. A MT is nucleated from the axoneme and grows against the barrier. As the MT gets longer the restoring force of the bead increases resulting in an increasing force onto the MT. Since force decreases MT growth speed MTs often pause before they undergo catastrophe.

Obviously from figure 6.2b when adding EBs (mal3, tea2 and tip1) MTs become

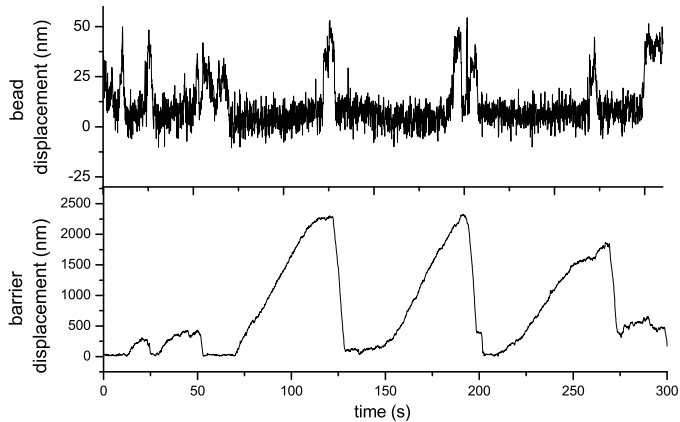


Figure 6.3: MT growth trajectory obtained with optical tweezers with force-feedback. a. Bead displacement as measured with the QPD during an experiment in the presence of mal3, tea2 and tip1 and a force of $F=1.5\text{pN}$. The bead position and force was kept (nearly) constant except during MT shrinkage phases when the force-feedback algorithm could not keep up with the fast bead displacement. **b.** To compensate for MT growth and to keep the bead at a constant position the barriers were displacement by the motorised piezo stage. The displacement is therefore proportional to MT length.

more dynamic. They initiate growth more often, have more catastrophes, transition to depolymerisation quite abruptly lacking a slow-growth regime before catastrophe and in general, do not grow as long. Since force is proportional to MT length, and thus a growing MT experiences an increasing force, it is an indication that MTs in the presence of EBs cannot bear forces as high as with pure tubulin. In this example we first see the nucleation of two long single MTs which is followed by the nucleation of MT bundles which do not always all shrink back to the axoneme before new ones are nucleated.

6.2.2 MT growth trajectories at constant force

Since MTs with EBs were quite sensitive to forces we also did experiments with force-clamped optical tweezers. In this case we could keep the force onto the MT constant and choose the force to be of low magnitude. Force-clamping is achieved by monitoring the bead position relative to the trap centre during the experiment. If their distance to each other increases due to MT growth we translate the barriers an equal distance in the opposite direction, as shown in figure 2.5 on page 23. As a result the bead is maintained (almost) continuously at a fixed distance to the trap centre. Since bead displacement is proportional to force we can this way achieve constant forces. The barriers are part of the sample flow chamber which is positioned on the microscope stage. Therefore, a translation of the microscope stage achieved by piezo actuators moves the barriers and maintains bead position.

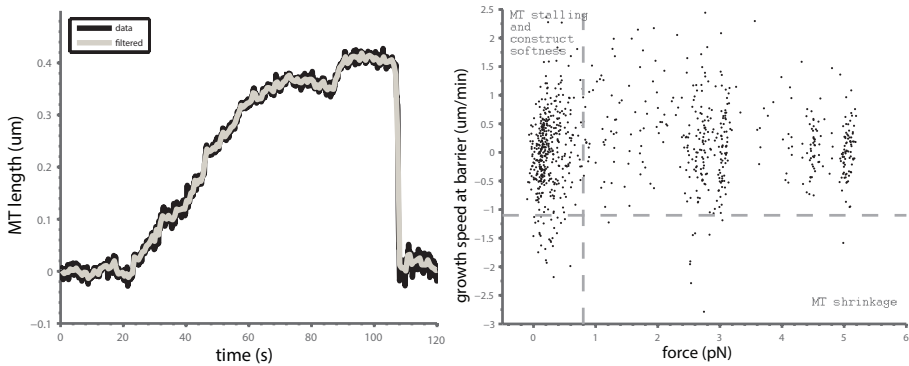


Figure 6.4: Filtering optical tweezers data obtained without force-feedback. a. Growth event of a MT of pure tubulin (second event in fig. 6.2a.), averaged with a fixed-size window of 0.8 s. **b.** For each interval we determine the average MT growth time and length and calculate the corresponding growth speed and force (using the trap stiffness). MT growth phases are selected by filtering out data below a certain growth speed and force (see text for more details).

Figure 6.3 shows MT growth trajectories obtained with force-feedback in the presence of EBs. The upper panel shows the bead position obtained with the QPD. It is a measure of the algorithm's ability to keep the bead at a constant position. In this case, the bead position is indeed (almost) constant except during MT shrinkage phases when the algorithm could not keep up with the fast change of the bead position. Since we are only interested in the MT growth phases this poses no problem.

The lower panel shows the displacement of the stage position which compensates for MT growth. This example shows a typical growth trajectory with five nucleation events of single or multiple MTs. A drawback of the force-feedback algorithm is that it measures with lower temporal resolution as the algorithm needs calculation and piezo actuation time.

6.2.3 Filtering growth speed and force data

To quantify the raw data obtained without force-feedback we first smoothed out short-term fluctuations by fixed-window averaging (typically 1 s windows). For an example see figure 6.4a which shows the raw and averaged data. We then selected MT growth traces below a certain length for two reasons: First, the QPD has a measurement range in which the signal in volts is proportional to a distance in meters. Above that range (in total $\sim 1.2 \mu\text{m}$) we cannot reliably convert volts to distance. Second, MTs which are too long could be buckling. We therefore analyse only MTs shorter than $1.5 \mu\text{m}$ where we can assume the absence of buckling. When applying force-feedback the bead position is nearly constant and does not exceed the linear range of the QPD. Therefore, in this case only the latter criterion

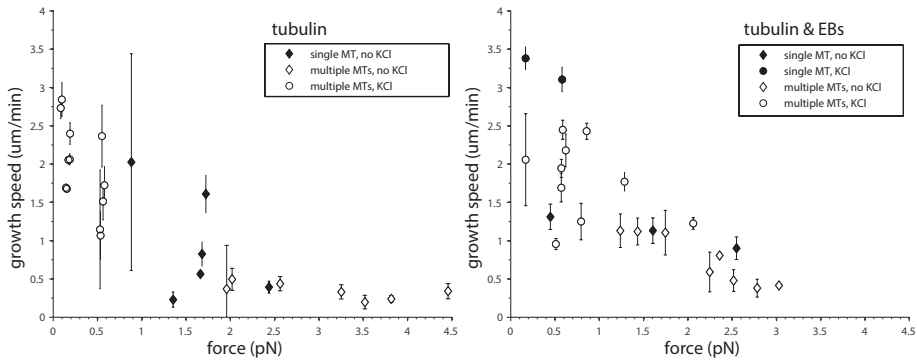


Figure 6.5: Forces decrease MT growth speed. Average growth speed and average force for MTs grown in different conditions (left in pure tubulin, right in presence of tubulin and mal3, tea2 and tip1; open symbols: multiple MTs, black symbols: single MTs; diamonds: no added salt, circles: 50 mM KCl added). Growth speeds decrease with an increasing force, both in the absence and presence of EBs. Surprisingly, both graphs are similar eliminating an effect of EBs on growth speeds under forces higher than 0.5 pN.

is of importance.

For each window we then determined the average MT growth speed, length and force as shown, as an example, in figure 6.4b. To exclusively select MT growth phases (and not shrinkage) we discarded growth speeds below a certain threshold, usually at $-1 \mu\text{m}/\text{min}$. We did not put the threshold at zero since also during growth the MT has very brief shortening excursions. Similarly, we excluded data below forces of $\sim 0.8 \text{ pN}$ which we assigned to Brownian motion of the construct before a MT-barrier contact was made. Another reason is the initial "soft" regime of the axoneme-bead construct after barrier contact was established, as explained above and shown in fig. 6.1f. The magnitude of both thresholds was determined from growth speed and force histograms and verified by eye. The remaining data was divided into force intervals of equal magnitude and for each interval the mean growth speed \bar{v}_g and mean force \bar{F} determined.

Please note that figure 6.4 presents data obtained without force-feedback. When analysing force-feedback data we proceeded analogously to the method described so far. We separately analysed the stage displacement for speeds and the bead displacement (so the QPD signal) for forces, also by window-averaging and thresholding (data not shown). Though the force was aimed to be constant it varied in a narrow range due to the processing time of the algorithm.

6.2.4 Force-growth speed relationship of optical trap data

Figure 6.5 shows the average growth speed and average force obtained from binned MT data during growth excursions. It is obvious that in the absence and presence of EBs MT growth speed decreases with an increasing force. This result has also been

shown before in our lab for MTs of pure tubulin [Dogterom and Yurke, 1997, Janson and Dogterom, 2004]. Nevertheless, since experiments were done at different conditions (single versus multiple MTs, without extra salt or with 50 mM KCl) we cannot combine the data to get more quantitative results.

Using TIRF microscopy we have examined stalling MTs in contact with a barrier (see chapter 5 on page 57ff). When comparing MTs in the presence and absence of mal3, tea2 and tip1 we saw that with EBs the catastrophe rate of MTs was increased. Janson et al. showed that for MTs grown in the presence of pure tubulin an increased catastrophe rate is the result of a reduced growth speed [Janson and Dogterom, 2004]. If the same relationship held in the presence of EBs, then we estimate the increased catastrophe rate with EBs to be combined with a reduced growth speed as well. Conclusively, we expected a faster decay of growth speeds with force in the presence of EBs than in their absence. Due to the different conditions we cannot directly compare the datasets in the absence and the presence of EBs. However, we know that multiple MTs can share a generated force and thus grow also at higher forces than a single MT can. Therefore, growth speed decays slightly slower with force when comparing multiple to single MTs. This has to be taken into account when looking at our data in the presence of EBs, which was mainly determined from axonemes growing multiple MTs. Nonetheless, we think that MTs grow under forces higher than 0.5 pN and in the presence of EBs (almost) with the same speed as MTs of tubulin alone (see fig. 6.5). Or in other words, growth speed is only slightly affected by forces in the range we measured. Note that we cannot compare the data reliably for forces below 0.5 pN since we do not have enough data in the presence of EBs. Possibly, the growth speeds differ with or without EBs for low forces.

6.3 Conclusions and discussion

By using an optical tweezers set-up we can measure MT growth trajectories with high temporal and spatial resolution. We extended the existing assay by force-feedback which allows us to measure at constant forces. Comparing the relationship of average MT growth speed and average force in the absence and presence of a MT end-binding system (EBs: mal3, tea2 and tip1) we do not detect a difference. Our results show that MTs grow under forces higher than 0.5 pN with a speed only slightly changed by the presence of EBs. On the other hand, as shown in chapter 5, the catastrophe rate under force is much increased when EBs are added. As this might seem contradictory, let us look at it in more detail. First of all, free MTs grown in the presence of EBs show an increased growth speed compared to pure tubulin-MTs [Brunner and Nurse, 2000a, Busch and Brunner, 2004, Bieling et al., 2007, Vitre et al., 2008]. We therefore expect the speed-force curves to cut the independent axis (where force is zero) at a higher magnitude when EBs are present. Whether this is the case is not obvious from our graphs since we do not have data at very small forces. Small forces only occur in two cases: right after the MT reached the barrier or with a pre-set small force using force-feedback. The former is hard to reliably measure since it is close to the soft regime of the

construct. In the latter case the force-feedback algorithm is too prone to react on noise and makes sensible measurements difficult.

On the other hand, we have shown in chapter 3 that EBs start to dissociate from the MT tip as soon as the MT reaches the barrier. So, several seconds after barrier contact is established and a force generated, the MT tip is free of EBs. As shown earlier, these MTs earlier underwent a catastrophe-promoting event which highly increases the likelihood for catastrophe. Nonetheless, while undergoing this step towards catastrophe, the MT tip structure can possibly still extend. MT growth until catastrophe with a decreasing mal3 binding has been shown earlier by Maurer et al. [Maurer et al., 2012]. The authors measured mal3 comet intensity and MT length changes of free MTs before, during and after a catastrophe. They saw that mal3 intensity, on average, started linearly decreasing about 10 s before catastrophe while the MT kept on growing until the onset of the actual shorting. As argued in chapter 4 also these free MTs "accomplished" a second step towards catastrophe, the difference of our MTs is the additional force. In our case we thus have a growing MT which, induced by force, lost (maybe partly) its mal3 comet. Since EBs do not bind to these MTs anymore, it could grow as if it was in the absence of EBs. Looking therefore at MT growth in the absence (of binding) of EBs it is not surprising the the speed-force curves look alike no matter whether EBs are present in the ambient buffer or not.

It has been speculated for long that EBs increase the sensitivity of MTs to force [Brunner and Nurse, 2000a]. The fact that EBs dissociate from the MT as soon as barrier contact is made shows that an EB decorated MT indeed reacts to forces. Therefore we can imagine that an effect of EBs on MTs under force happens already at very small forces. Since it is difficult to measure at these forces, the effect of EBs would not be visible in our speed-force relationship. If it was we would image a steep decline of speed-force relationship for those small forces. This would then at slightly higher forces coalesce into the speed-force relationship measured with pure tubulin.

6.4 Methods

The optical tweezers experiment was based on [Laan et al., 2008] and chapter 2.3 on page 18.

Preparation of the flow chamber. "Star"-shaped polymer barriers made of SU-8 were micro-fabricated on glass cover slips (see 2.3.1). Before experiment they were briefly sonicated first in iso-propanol and then in Milli-Q. An experimental chamber was assembled by first cutting a fine path into a piece of parafilm which would later serve as the flow chamber. This was glued between a microscope slide and a barrier-containing coverslip such that the barriers were on top of the cut-out path. Flow speed could be controlled by the relative height of loading gap and drain (see fig. 6.6). The flow chamber was functionalised by subsequently flowing 2-propanol, 0.0125% triton X-100 (PlusOne, GE Healthcare, Buckinghamshire, UK) and MRB80. It was then passivated by incubating 0.3 % F-127 Pluronic for 10 minutes. Unless stated otherwise, chemical reagents were obtained from Sigma-Aldrich (Saint-Louis, MO, USA).

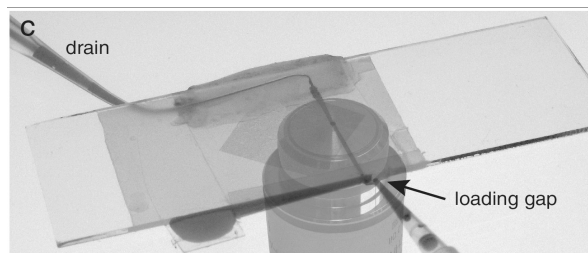


Figure 6.6: Flow chamber.

Flow cell consisting of a channel in parafilm sandwiched between a microscope slide (top) and a coverslip with star-shaped barriers (bottom). Dye shows the fluid path from reservoir to drain. The microscope objective was photographed separately and added for clarity.

Sample preparation. The experiment started with the injection of axonemes (kind gift from Matt Footer, Stanford University School of Medicine, Stanford, CA, USA) and 2.01 μm -diameter streptavidin-coated polystyrene beads (Spherotech, Libertyville, IL, USA). Next, an axoneme-bead construct was assembled by non-specific attachment of streptavidin to the axoneme. After checking the construct for softness and trap stiffness (see also 2.3.4) the construct was positioned in proximity to a barrier. In the presence of end-binding proteins (EBs) MT nucleation from the axoneme was difficult under force. Therefore, with EBs, the axoneme tip was positioned 50-100 nm in front of the barrier. Finally, MT growth was initiated by flowing MRB80 buffer at low speeds (80 mM K-PIPES pH 6.8, 50 mM KCl, 4 mM MgCl_2 , 1.6 mM GTP, 2 mM ATP, 1 mM EGTA, 10 mM 2-mercaptoethanol), 0.2 mg/ml κ -casein, 25 μM tubulin (Cytoskeleton, Denver, CO, USA). Optionally, end-binding proteins (EBs) were added to the MRB80 buffer: 200 nM mal3, 8 nM tea2 and 50 nM tip1 which were purified as described in [Bieling et al., 2007]. The experiments were performed at a constant temperature of 28 $^\circ\text{C}$.

Experimental methods. During an experiment MT growth pushed the bead out of the trap centre. The bead-axoneme construct was imaged with video-enhanced differential interference contrast microscopy (VE-DIC). Using cross-correlation the bead position was live tracked with home-written LabView software. When doing force-feedback experiments, the bead was imaged onto a quadrant photo diode (QPD) using a red HeNe-laser with 633 nm wavelength (1125P, Uniphase, Barrington, NJ, USA). A home-written LabView software calculated the measured relative distance between bead and trap centre and compared it to a desired "setpoint" (which we defined before onset of the experiment) at 8-12 Hz. Aiming at keeping the bead position the same as the setpoint the software then calculated the speed and distance of barrier translation. For this it used a proportional-integral-derivative (PID) algorithm.

Data analysis. All data was saved to disk and after the experiment the bead position was tracked with our LabView software at 25 Hz. The data was then processed with MathCad 15 (PTC, Needham, MA, USA) and Matlab (Mathworks, Natick, NA, USA).

Acknowledgements

I want to thank Olga Sytina for help in preparing the experiments, for carrying them out and for doing most of the data analysis. We thank Chris Rétif, Gijs Vollenbroek and Hans Zeijlemaker for their advice on micro-fabrication, E. Laura Munteanu, and Julien Husson for help with the optical trap assay and Roland Dries for developing the bead-tracking software. We appreciate the help of Peter Bieling and Thomas Surrey with the protein purification of mal3, tea2 and tip1 and we thank Matt Footer for generously providing us with axonemes. The work presented in this chapter was carried out as part of the EU Program AMOCROSS, as part of a "VICI" grant provided by the "Nederlandse Organisatie voor Wetenschappelijk Onderzoek (NWO)" and as part of the research program of the "Stichting voor Fundamenteel Onderzoek der Materie (FOM)", which is financially supported by the "Nederlandse Organisatie voor Wetenschappelijk Onderzoek (NWO)".

EB3-informed dynamics of the MT stabilizing cap during stalled growth



Authors: Kok MWA, Huber F, Kalisch SMJ, and Dogterom M

Microtubule stability is known to be governed by a stabilizing GTP/GDP-Pi cap, but the exact relation between growth velocity, GTP hydrolysis and catastrophes remains unclear. We investigate the dynamics of the stabilizing cap through *in vitro* reconstitution of microtubule dynamics in contact with micro-fabricated barriers, using the plus-end binding protein GFP-EB3 as a marker for the nucleotide state of the tip. The interaction of growing microtubules with steric objects is known to slow down microtubule growth and accelerate catastrophes. We show that the lifetime distributions of stalled microtubules, as well as the corresponding lifetime distributions of freely growing microtubules, can be fully described with a simple phenomenological 1D model based on noisy microtubule growth and a single EB3-dependent hydrolysis rate. This same model is furthermore capable of explaining both the previously reported mild catastrophe dependence on microtubule growth rates and the catastrophe statistics during tubulin washout experiments.

7.1 Introduction

Microtubules are hollow cylindrical polymers consisting of $\alpha\beta$ -tubulin dimers arranged in a head-to-tail fashion to form protofilaments, ~ 13 of which typically constitute the microtubule lattice ([Debs et al., 2020, Tilney et al., 1973, Zhang et al., 2015]). Individual microtubules constantly switch between phases of growth and shrinkage, a fundamental process known as dynamic instability ([Mitchison and Kirschner, 1984a]). As a major constituent of the eukaryotic cytoskeleton, microtubules are involved in many essential processes within the cell, including intracellular transport, cell division, and cell morphology ([Akhmanova and Steinmetz, 2015]). During these processes, dynamic microtubule ends interact with other cellular components, either through intermediary protein complexes or through direct physical contact ([Colin et al., 2018, Dogterom and Koenderink, 2019, Gurel et al., 2014, Nguyen-Ngoc et al., 2007, Lopez et al., 2014, Waterman-Storer et al., 1995]). Such contacts typically affect the dynamic behaviour of

microtubule ends which is integral to the biological function of these interactions ([Bouchet et al., 2016, Brangwynne et al., 2006, Gregoret et al., 2006, Komarova et al., 2002, Letort et al., 2016, Tischer et al., 2009, Vleugel et al., 2016]).

The biochemical mechanism behind the stochastic transition from growth to shrinkage, known as a catastrophe, is related to the progressive hydrolysis of GTP bound to β -tubulin ([Carlier and Pantaloni, 1982, Nogales, 1999]). During polymerization, the microtubule tip is highly dynamic due to continuous addition and removal of tubulin dimers ([Gardner et al., 2011b, Kerssemakers et al., 2006, Rickman et al., 2017, Schek et al., 2007]). After GTP-bound tubulin is incorporated at the microtubule tip, hydrolysis of the nucleotide followed by Pi release is hypothesized to lead to a destabilization of the lattice by a compaction around the exchangeable nucleotide [Alushin et al., 2014, Zhang et al., 2015]. The delay between tubulin incorporation and hydrolysis results in a GTP/GDP-Pi enriched region at the microtubule tip, which gives rise to what is known as the stabilizing cap ([Carlier and Pantaloni, 1981]). Upon the loss of the stabilizing cap, a catastrophe follows upon which the strain build-up in the lattice is released during depolymerization. However, whereas this basic description of the biochemistry behind dynamic instability is generally accepted, the exact relation between GTP hydrolysis, the size of the stabilizing cap, the details of microtubule growth and the statistics of catastrophes is still not fully understood, despite the availability of a wealth of quantitative data on catastrophe statistics under different conditions ([Brouhard and Rice, 2018, Ohi and Zanic, 2016]).

Various estimates of the stabilizing cap size have been reported, from short caps of a few terminal tubulin layers ([Brun et al., 2009, Caplow and Shanks, 1996, Drechsel and Kirschner, 1994, Karr and Purich, 1978, Walker et al., 1991]) to longer caps spanning up to dozens of layers ([Carlier and Pantaloni, 1981, Seetapun et al., 2012]). In recent years, direct visualisation of the tubulin nucleotide state has become possible with the family of end binding proteins (EBs) that can autonomously bind to the GDP-Pi region at the microtubule tip ([Maurer et al., 2011]). It has been shown that the size of the EB comet at the tip correlates with the size of the stabilizing cap and consequently with microtubule stability ([Duellberg et al., 2016a, Seetapun et al., 2012, Zhang et al., 2015]). In fact, tubulin washout experiments using Mal3 (the EB1 homolog in yeast) suggest that not the size of the total EB binding region is decisive in preventing a catastrophe, but the presence of a critical number of unhydrolyzed subunits at the terminal (~10 tubulin layers at the microtubule tip (~130 dimers) ([Duellberg et al., 2016a]).

Here we use the ability of EB3 to report on the status of the stabilizing cap to investigate the detailed relation between cap dynamics and catastrophe statistics for stalling microtubules that are pushing against microfabricated barriers. A stalling microtubule exerts a pushing force that is too small to overcome its critical buckling force, resulting in the blocking of further microtubule growth. The stability of pushing microtubules has previously been studied for buckling and bending microtubules in vitro ([Janson et al., 2003]), in vivo ([Brangwynne

et al., 2007, Odde et al., 1999, Pallavicini et al., 2017)), and in silico ([Das et al., 2014, Valiyakath and Gopalakrishnan, 2018]). It was established that microtubules generating pushing forces against rigid barriers in vitro experience an increased catastrophe frequency ([Janson et al., 2003, Laan et al., 2008]). This force-induced catastrophe is thought to be the result of a reduction in the addition of tubulin dimers as the microtubule growth velocity is slowed with increasing force ([Janson et al., 2003, Kerssemakers et al., 2006]). However, exactly how the reduction of tubulin addition in combination with nucleotide hydrolysis affects the dynamics of the stabilizing cap, and thereby determines the lifetime statistics for stalled microtubules, has remained unresolved.

We determine the lifetime statistics of stalling microtubules in vitro by growing microtubules against micro-fabricated barriers using GFP-EB3 as a proxy for the size of the stabilizing cap. By introducing a novel barrier design with a long overhang, we ensure that microtubule stalling can be imaged simultaneously with the EB3 signal using TIRF microscopy. We observe that microtubule stalling increases the catastrophe frequency in the absence of EB3 as previously reported ([Janson et al., 2003]). In the presence of EB3 the microtubule lifetime is further reduced in a concentration dependent manner. Surprisingly, the full decay of the EB3 comet during microtubule stalling does not necessarily lead to an immediate catastrophe. We compare our results to similar data obtained for freely growing microtubules under the same conditions, and then perform simulations of microtubule dynamics based on a simple model in an attempt to simultaneously explain both data sets.

Over the years, different types of models have been proposed to gain a better understanding of what triggers a catastrophe. Biochemical models rely on the hydrolysis of tubulin dimers to reduce the size of the stabilizing cap to trigger a catastrophe ([Bayley et al., 1989, Brun et al., 2009, Chen and Hill, 1985, Gardner et al., 2011b, Margolin et al., 2012, Padinhateeri et al., 2012, Piedra et al., 2016, VanBuren et al., 2002]). However, only with the introduction of lateral interactions between dimers in a 2D model can these models capture observed growth fluctuations ([Gardner et al., 2011b]) and observed microtubule lifetimes ([Bowne-Anderson et al., 2013, Lee and Terentjev, 2019]). Mechanochemical models additionally include the build-up of strain in the lattice and protofilament bending at the tip ([Bollinger and Stevens, 2019, Coombes et al., 2013, Mcintosh et al., 2018, Michaels et al., 2020, Molodtsov et al., 2005b, VanBuren et al., 2005, Zakharov et al., 2015]). Both types of models can explain a variety of experimental observations of dynamic instability, but they typically require many fitting parameters and do not explicitly include the highly dynamic nature of the microtubule tip. Alternatively, simple phenomenological models have been useful in obtaining an intuitive insight into the principles behind microtubule dynamics and the effect of microtubule associated proteins ([Brun et al., 2009, Duellberg et al., 2016a, Flyvbjerg et al., 1996, Rickman et al., 2017]).

To find a minimal model capable of explaining microtubule catastrophe statistics with the smallest possible number of fitting parameters, we use coarse-grained

Monte Carlo simulations of 1D filaments ([Flyvbjerg et al., 1996, Margolin et al., 2006, Padinhateeri et al., 2012, Rickman et al., 2017]). We show that the lifetimes of both freely growing and stalled microtubules can be explained by a combination of random GTP hydrolysis and a parameter that characterises the noisiness of microtubule growth, a concept that was generally missing from previous phenomenological models in the description of microtubule lifetimes. We confirm that while the EB binding region is a measure for the size of the stabilizing cap, there is no one-to-one correlation between its presence and the onset of a catastrophe. Instead, the data are consistent with a catastrophe being triggered when a large enough sequence of GDP-bound tubulin dimers becomes exposed at the microtubule tip. Importantly, this 1D biochemical model can also successfully capture the previously reported catastrophe dependence on tubulin concentration, taking into account previously reported velocity-dependent growth fluctuations, and it is in good agreement with previously reported catastrophe delays after tubulin dilution. The so-called “ageing” of microtubules, referring to the observed increase of the catastrophe frequency with microtubule age ([Coombes et al., 2013, Duellberg et al., 2016b, Gardner et al., 2011b, Odde et al., 1995]), is not a feature of our simple model, but this behaviour naturally emerges by additionally assuming that microtubule growth fluctuations increase with microtubule age.

7.2 Results

7.2.1 In vitro reconstitution of microtubule stalling

To investigate the stability of stalling microtubules in the presence of different concentrations of GFP-EB3, we analysed the dynamics of microtubules growing against micro-fabricated barriers using an in vitro reconstitution assay ([Bieling et al., 2007, Kalisch et al., 2011]). We assume each microtubule to consist of three regions: 1) a GTP rich terminal region where protofilament growth takes place ([Maurer et al., 2014, Mcintosh et al., 2018]), 2) a region containing the intermediate GDP-Pi state to which EB3 preferably binds ([Maurer et al., 2011]), and 3) the GDP lattice (Fig. 1A). The presence of EB3 is known to increase both the GTP hydrolysis rate and the microtubule growth velocity by respectively compacting the microtubule lattice and closing the lattice seam ([Maurer et al., 2014, Zhang et al., 2015]). Microtubules were nucleated from GMPCPP-stabilized seeds and imaged with Total Internal Reflection Fluorescence (TIRF) microscopy. The barriers were composed of 100 nm SiO₂ deposited on a glass coverslip with an amorphous silicon carbide (SiC) overhang, approximately 1.5 μm long, to trap the microtubules and force them to grow into the barriers (Fig. 1BC). SiC is a mechanically stable, optically transparent material (wavelengths $> 0.5 \mu\text{m}$) with similar passivation and functionalization properties as SiO₂ due to a very thin native oxide layer on its surface ([Coletti et al., 2007, Dhar et al., 2009]). Although fabrication of the barriers requires a thin 10 nm layer of SiC on the glass surface (see Methods for details), microtubules can be imaged successfully with TIRF microscopy (Fig. 1D and S1). This novel barrier design enables high resolution imaging with TIRF microscopy as the microtubules are forced to remain within 100 nm from the surface during barrier contact, elimin-

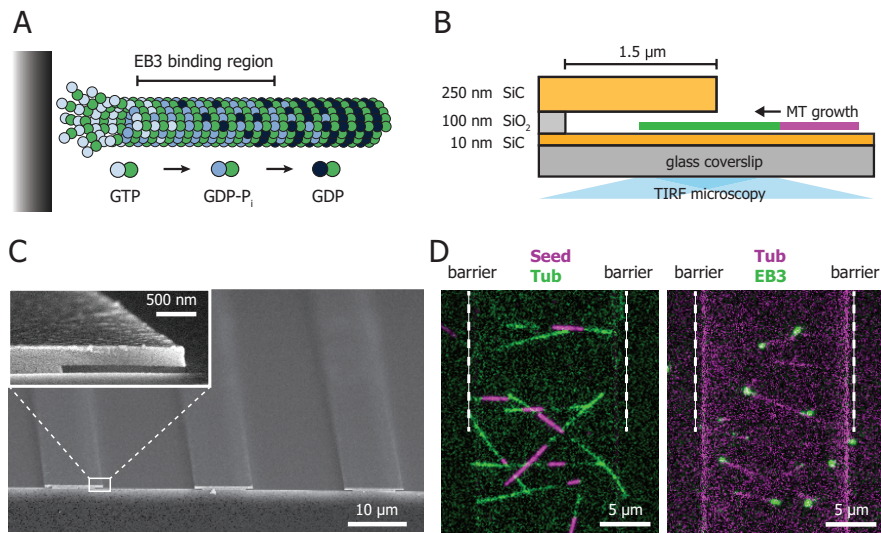


Figure 7.1: In vitro reconstitution of microtubule stalling. **A.** Schematic depiction of the nucleotide distribution at the microtubule tip. Progressive hydrolysis of GTP-tubulin after incorporation leads to a destabilized lattice that is stabilized by a GTP/GDP-Pi cap. EB3 chiefly binds to the GDP-Pi rich region. During microtubule-barrier contact, reduction of microtubule growth and ongoing hydrolysis are hypothesized to lead to an accelerated loss of the protective cap. **B.** Schematic of the micro-fabricated barrier with a 1.5 μm overhang made of silicon carbide (SiC). The barrier itself is composed of SiO₂ and is 100 nm high, forcing the growing microtubules to remain within the TIRF illumination field. Microtubules are grown from stabilized GMPCPP seeds. **C.** Scanning Electron Microscope image of two channels with barriers. The insert shows a zoom of the barrier with a 1.5 μm SiC overhang. **D.** TIRF images of the micro-fabricated channel enclosed by two barriers (white dotted lines). On the left microtubules (green) are nucleated from GMPCPP-stabilized seeds (magenta) towards the barriers and on the right microtubules (magenta) polymerize towards the barriers in the presence of GFP-EB3 (green). See also Fig S1 and Videos S1 and S2.

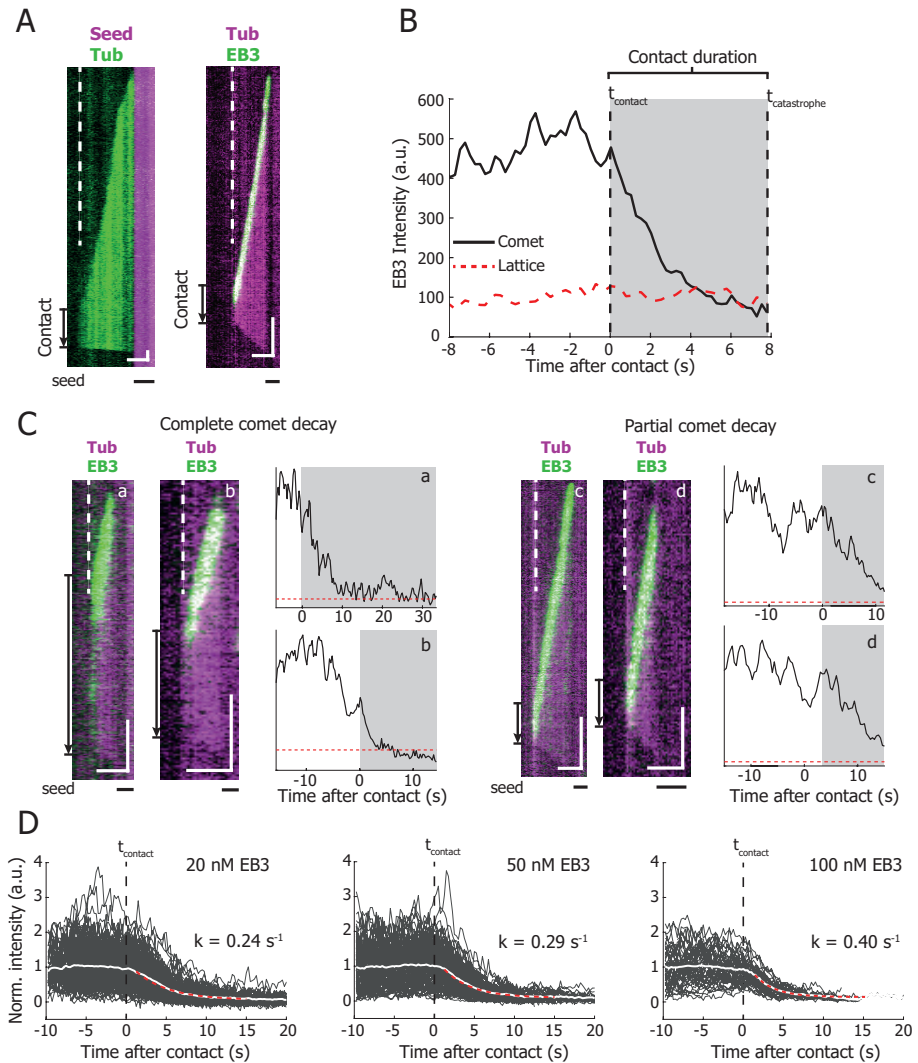


Figure 7.2: Microtubule stalling events in vitro. **A.** Representative kymographs of a microtubule-barrier contact event in the presence of $15 \mu\text{M}$ Hilyte488-labelled tubulin (left) and in the presence of $15 \mu\text{M}$ rhodamine-labelled tubulin with 20 nM GFP-EB3 (right). The dotted line denotes the position of the SiO_2 barrier. The duration of barrier contact is indicated with an arrow. Scale bars: $2 \mu\text{m}$ (horizontal) and 10 s (vertical). **B.** Mean intensity of the EB3 comet and the EB3 signal on the microtubule lattice of the kymograph on the right in **a**. From the moment of microtubule-barrier contact (t_{contact}), the EB3 comet signal decays to the level of the microtubule lattice, ultimately resulting in the onset of a catastrophe ($t_{\text{catastrophe}}$) after 7.75 s .

C. Several examples of stalling microtubules with their respective comet intensity traces. Traces **a-b** show a full comet decay during barrier contact before the onset of a catastrophe, whereas the comet in traces **c-d** only partially decays. All traces were in the presence of 15 μM tubulin. Additionally, trace **a** contained 20 nM EB3, trace **b** and **c** 100 nM EB3, and trace **d** 50 nM EB3. Arrows and shaded regions illustrate the duration of microtubule stalling event. Scale bars: 2 μm (horizontal) and 10 s (vertical). **D.** Normalized comet intensity traces of stalling microtubules in the presence of 20, 50, and 100 nM EB3, aligned on the moment of barrier contact (t_{contact}). The mean decays were fitted with a mono-exponential model and show an increasing decay rate with increasing EB3 concentrations, resulting in decay rates of 0.24 s^{-1} , 0.29 s^{-1} , and 0.40 s^{-1} for 20, 50, and 100 nM respectively. Number of stalling events analysed: 20 nM, $n = 151$, 50 nM, $n = 104$, and 100 nM, $n = 92$.

ating fluctuations perpendicular to the surface. The width between two barriers is 15 μm , chosen to keep the microtubules short and thereby reduce the probability of observing slipping and buckling events ([Janson et al., 2003]). All experiments were performed in the presence of 15 μM tubulin, and 0, 20, 50, or 100 nM GFP-EB3.

7.2.2 Complete EB3 decay is neither needed for, nor always immediately followed by a catastrophe

The microtubule-barrier contact events leading to a stalling microtubule were analysed with kymographs to obtain the contact duration and GFP-EB3 comet intensity prior and during contact (Fig. 2A and S1, see Methods for details). Any contact events leading to microtubule buckling or sliding along the barrier were excluded from the analysis. From the moment of barrier contact, the EB3 intensity at the microtubule tip decreased until the onset of catastrophe (Fig. 2B, S1D). We observed that for $\sim 65\%$ of all stalling events, a catastrophe occurred while the EB comet was still decaying ($> 10\%$ of the EB signal remaining) (Fig 2C, right). For those events, the mean comet intensity at the moment of catastrophe was 16% of the pre-contact mean. For the remaining $\sim 35\%$ of stalling events we found a decay of the EB comet to a steady near-zero value which did not immediately lead to catastrophe. Instead, the microtubules remained in contact with the barrier for some time, even in the absence of an observable EB3 comet (Fig. 2C, left). Fitting the average EB decay from the moment of barrier contact with a mono-exponential function, shows that the decay rate increases with EB3 concentration: 0.24 s^{-1} , 0.29 s^{-1} , and 0.40 s^{-1} for 20, 50, and 100 nM EB3 respectively (Fig. 2D). The presence of EB3 thus accelerates the decay of the EB comet during stalling events as predicted from its increasing effect on the GTP hydrolysis rate ([Maurer et al., 2014, Zhang et al., 2015]).

7.2.3 Monte Carlo simulation of microtubule catastrophes

To determine whether microtubule lifetime statistics of stalling microtubules can be understood solely by a single stochastic hydrolysis step combined with net stalling of noisy microtubule growth, we performed minimalistic Monte Carlo sim-

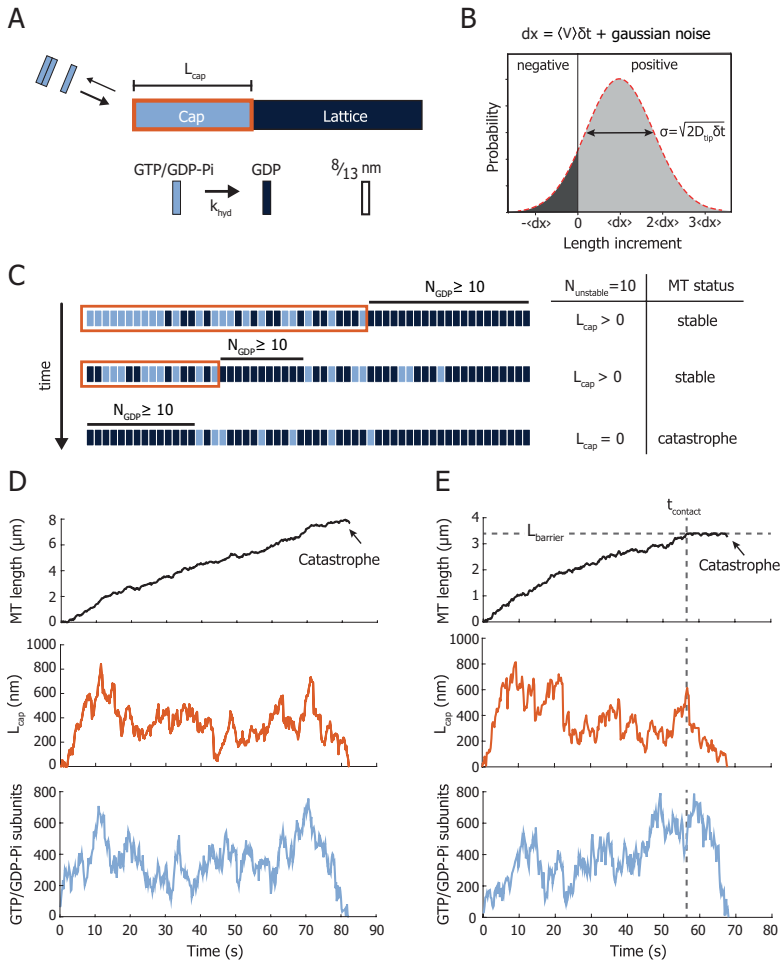


Figure 7.3: Monte-Carlo simulation of microtubule dynamics. **A.** The microtubule is simulated as a one-dimensional lattice with two states, a GTP/GDP-Pi and a GDP state, that are approximately distributed in a cap with length L_{cap} and a lattice region respectively. The size of each subunit is $8/13$ nm. Uncoupled stochastic hydrolysis matures the GTP/GDP-Pi-state into the GDP-state with rate k_{hyd} . **B.** Microtubule growth is determined by a mean growth velocity $\langle V \rangle$ with added Gaussian noise characterized by D_{tip} , resulting in stochastic tip elongation following a biased random walk. The diffusive character of the tip can also produce negative growth excursions. **C.** Detailed schematic of the nucleotide composition of the microtubule tip. The size of the stabilizing cap (orange) is defined as the region between the microtubule tip and the position along the lattice where for the first time an uninterrupted sequence of GDP subunits is equal or greater than $N_{unstable}$. A catastrophe is triggered when the number of uninterrupted GDP subunits at the very tip of the microtubule is equal or greater than $N_{unstable}$. As example, the case for $N_{unstable} = 10$ is shown. **D.** Simulated microtubule growing event. (top) During the noisy microtubule growth, the microtubule length follows a biased random walk. (middle) When the size of the stabilizing cap (L_{cap}) is reduced to zero, i.e. when the number of uninterrupted terminal GDP subunits is equal or greater than $N_{unstable}$, a catastrophe follows, and the simulation is terminated.

(bottom) Total number of GTP/GDP-Pi subunits in the simulated microtubule, which can be compared with the experimentally obtained EB3 signal. **E.** Simulated microtubule stalling event. Figures show the simulated microtubule length (top), the size of the stabilizing cap (L_{cap}) (middle), and the total number of GTP/GDP-Pi subunits in the simulated microtubule (bottom). Barrier contact is simulated by restricting the maximum length of the microtubule to $L_{barrier}$. As the microtubule can undergo occasional negative growth excursions due to noisy growth, the microtubule length can still fluctuate during barrier contact.

ulations of both free and stalled microtubule growth. Microtubules were treated as 1D filaments with subunits of 8/13 nm comprising two distinct states: GTP/GDP-Pi and GDP (Fig. 3A). We decided to ignore the initial transition from GTP to GDP-Pi, which was reported to be much faster than the GDP-Pi to GDP transition ([Kim and Rice, 2019, Maurer et al., 2014, Rickman et al., 2017]). We saw this justified by the fact that our key observations changed only very moderately when the first transition was included explicitly, whereas omitting this transition reduced the number of model parameters. Simulated microtubules grow by addition of GTP/GDP-Pi subunits which subsequently undergo random hydrolysis to GDP with rate k_{hyd} (Fig. 3A). We treat microtubule growth as a discrete, biased Gaussian random walk ([Antal et al., 2007, Flyvbjerg et al., 1996]), inspired by experimental observations that revealed a substantial diffusive character of the growing microtubule tip ([Gardner et al., 2011b, Kerssemakers et al., 2006, Rickman et al., 2017, Schek et al., 2007]). Following this model, tip growth is fully characterized by the experimentally measured mean growth velocity (V) and the diffusion constant D_{tip} , which may also result in occasional negative growth excursions (Fig. 3B). A catastrophe is triggered when a stabilizing cap (L_{cap}) that results from remaining GTP/GDP-Pi subunits is lost due to a negative growth excursion and/or random hydrolysis. We assume that the nucleotide state of the tubulins at the very tip of the microtubule are the most relevant for stability: a catastrophe is triggered when the number of uninterrupted GDP subunits at the very tip of the microtubule is equal or greater than $N_{unstable}$ ([Brun et al., 2009, Padinhateeri et al., 2012]), independent of how many GTP/GDP-Pi subunits remain elsewhere in the lattice (Fig 3CD). The length of the stabilizing cap is thus determined by the distance between the position of the microtubule tip and the position along the lattice where for the first time an uninterrupted sequence (or ‘island’) of GDP units equal or greater than the fitting parameter $N_{unstable}$ is found (Fig. 3C). Depolymerization and rescues are not considered in the model. To exclude nucleation kinetics from the simulated lifetimes, a microtubule is considered to grow after reaching a length of 250 nm. The simulation then only requires the three fitting parameters k_{hyd} , D_{tip} , and $N_{unstable}$, all of which can be verified with experimental data (see below). The experimental EB3 intensity at the microtubule tip can be compared to the total number of GTP/GDP-Pi-state subunits in the simulated microtubules (Fig. 3DE, bottom).

Microtubule stalling is simulated by introducing a fixed maximum length $L_{barrier}$ (Fig. 3E). Any growth excursions that would bring the microtubule length to $L > L_{barrier}$ are truncated to this maximum length. Since tip fluctuations also include

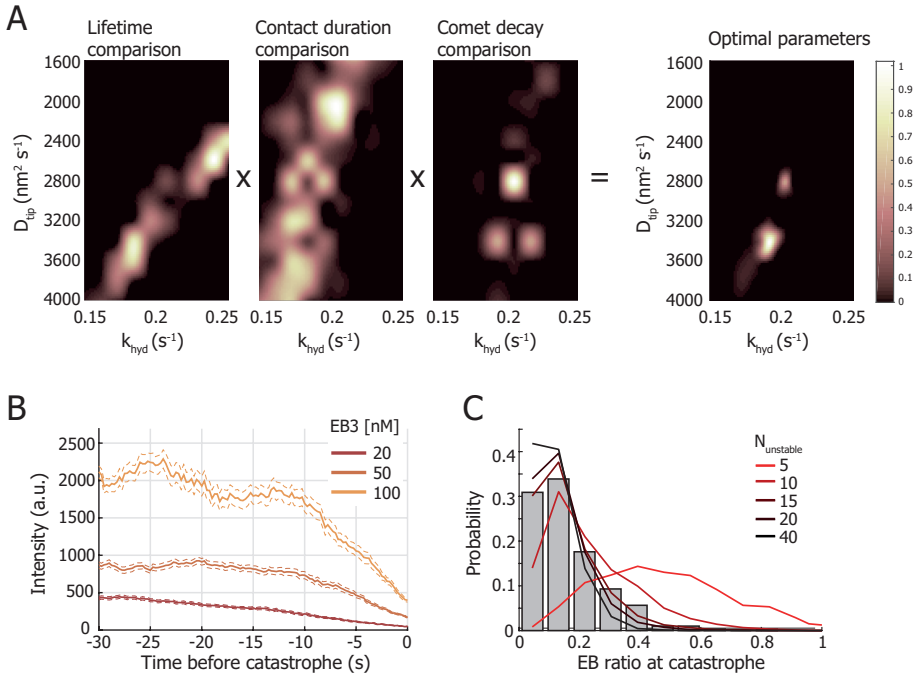


Figure 7.4: Parameter determination of the 1D model. **A.** The diffusion constant D_{tip} and hydrolysis rate k_{hyd} are determined by comparing the simulated microtubule lifetime distributions, the contact duration distributions, and the decay of the EB signal during contact with the respective experimental distributions. The lifetime and contact duration distributions are compared with the experimental distributions using a Kolmogorov-Smirnov test. A cubic interpolation of the similarity values is captured in (normalized) heatmaps. The comet decay rate comparison is obtained by evaluating the absolute difference between simulated rates and experimental rates. Evaluating the product of the three heatmaps results in a parameter pair of D_{tip} and k_{hyd} best describing the datasets. The shown heatmaps are of 20 nM EB3. See also Fig. S2. **B.** The mean experimental EB3 signal during barrier contact, aligned on the moment of catastrophe for 20 (n=151), 50 (n=104), and 100 nM (n=92) EB3. The ratio between the steady-state EB3 signal prior to catastrophe (from -30 to -15 seconds) and at the moment of catastrophe can be compared with the simulated data. The dotted lines denote the SEM. **C.** Histogram of the ratio between the mean comet intensity during steady-state growth and the comet intensity at the moment of catastrophe. The data is pooled from all experimental datasets of 20, 50, and 100 nM EB3 (n=347). The lines show the simulated GTP/GDP-Pi ratio for $N_{unstable}$ values of 5, 10, 15, 20, and 40. We find that a minimum $N_{unstable}$ value of 15 is required to capture the distribution of pooled experimental EB3 ratios.

occasional negative growth excursions (Fig. 3B), fluctuations of the tip position continue after barrier contact (Fig. 3E).

7.2.4 Obtaining the simulation parameters

Our 1D model relies on three fitting parameters, D_{tip} , k_{hyd} , and $N_{unstable}$. Based on existing literature ([Maurer et al., 2014]), we expected that adding EB3 would have an effect on the transition from GTP/GDP-Pi to GDP. Since EB3 also affects the microtubule growth velocity, we also expected that growing microtubules may display different growth fluctuations at different EB concentrations. It hence appeared reasonable to keep k_{hyd} and D_{tip} as free fitting parameters, while keeping $N_{unstable}$ as a global fitting parameter that is independent of the presence of EB3. We obtained values for the mean growth velocity $\langle V \rangle$ of 1.7, 2.8, 2.8, and 3.7 $\mu\text{m}/\text{min}$ for 0, 20, 50, and 100 nM EB3 respectively and a global mean seed-barrier distance $L_{barrier}$ of 3.4 μm from the experimental data.

To find good fitting values, we performed systematic parameter scans across a range of D_{tip} and k_{hyd} , simulating 500 microtubule growth events for each parameter combination. We simulated both freely growing and stalling microtubules and compared the distributions with the respective experimental distributions. Using a Kolmogorov-Smirnov test as a measure of the similarity between the simulated and experimental distributions, we obtained heatmaps with (normalized) similarity parameters for each compared distribution (Fig. 4A). We also included a comparison between the simulated GTP/GDP-Pi decay and the experimental EB decay rate during stalling (Fig. 2D). The resulting range of k_{hyd} values that captured the experimental decay rates was used to restrict the range of possible k_{hyd} values for the comparison of simulated and experimental lifetime distributions. The parameter set best capturing all three comparisons was then found by calculating the product between the heatmaps within the range allowed by the decay rates (Fig. 4A and S2).

7.2.5 Determining the catastrophe threshold for the 1D model

To determine the catastrophe threshold governed by $N_{unstable}$, we made use of the experimentally observed decay of the mean EB signal at the barrier (Fig. 2D). Our analysis yielded simultaneous fits of D_{tip} and k_{hyd} that were in very good agreement with our experimental observations across a wide range of $N_{unstable}$ values. To determine an ideal value for $N_{unstable}$ to match our data, we looked at the ratio between the mean EB3 signal during steady-state growth and the EB3 signal at the moment of catastrophe. This would give us a measure of what fraction of GTP/GDP-Pi subunits was on average hydrolysed at the moment a catastrophe occurred (Fig. 4B). Higher values for $N_{unstable}$ gave rise to a longer stabilizing cap, resulting in a higher ratio of hydrolysed subunits in the cap at the moment of catastrophe. Comparing the combined distributions of the EB3 ratios with simulated ratios for several $N_{unstable}$ values results in a minimum $N_{unstable}$ value of ~ 15 subunits (Fig. 4C).

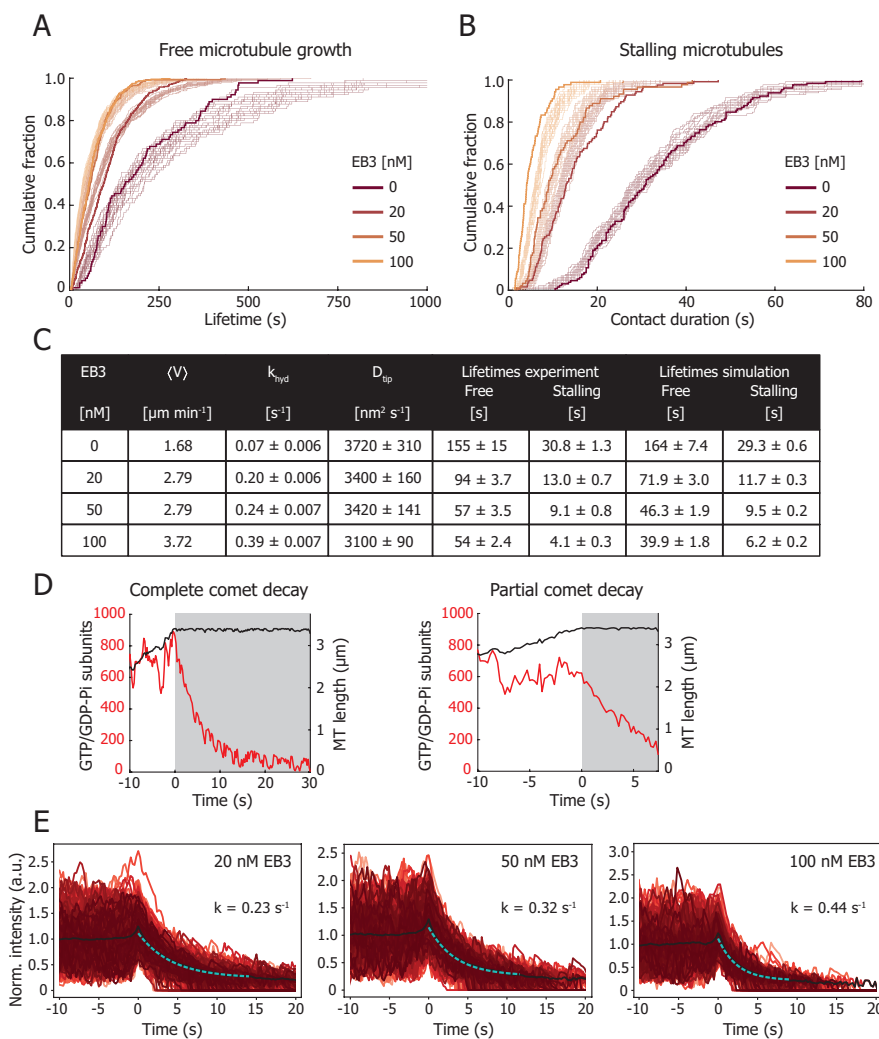


Figure 7.5: Free microtubule growth and microtubule stalling. **A.** The cumulative fraction of the lifetimes of freely growing microtubules at increasing concentrations of 0 nM ($n=90$), 20 nM ($n=384$), 50 nM ($n=262$), and 100 nM ($n=398$) EB3. All data were obtained with $15 \mu\text{M}$ tubulin. The bold lines show the experimental data and the thin lines show 25 bootstrapped simulated distributions of equal number of datapoints as the experimental distribution. **B.** The cumulative fraction of the microtubule-barrier contact durations at increasing concentrations of 0 nM ($n=131$), 20 nM ($n=126$), 50 nM ($n=90$), and 100 nM ($n=90$) GFP-EB3. All data were obtained with $15 \mu\text{M}$ tubulin. The bold lines show the experimental data and the thin lines show 25 bootstrapped simulated distributions of equal number of datapoints as the experimental distribution. **C.** Table with the growth velocity $\langle V \rangle$ (mean \pm std), hydrolysis rate k_{hyd} (mean \pm 95% CI), and diffusion constant D_{tip} (mean \pm 95% CI) as determined to simulate the lifetimes of freely growing microtubules and the contact duration of stalling microtubules at each EB concentration (median \pm SE). **D.** Examples of simulated stalling events, showing the microtubule length and the total number of GTP/GDP-Pi subunits in the lattice. The left trace shows a full comet decay during barrier contact before the onset of

a catastrophe, whereas the comet in traces on the right only partially decays. **E.** Simulated decay of GTP/GDP-Pi subunits during microtubule stalling at increasing EB concentration. Each dataset contains 1000 simulated events.

7.2.6 The 1D model can successfully capture microtubule lifetimes

Figures 5A and 5B show the experimental cumulative fraction of the lifetimes of freely growing microtubules and of the stalling duration respectively (bold lines), in the presence of 15 μM tubulin and 0, 20, 50, and 100 nM GFP-EB3. The distribution of free lifetimes was determined using microtubules growing parallel to the barriers. By bootstrapping each simulated distribution obtained with the best-fitting parameters (Fig. 5C), we show 25 simulated traces containing an equal number of data points as the experimental dataset (thin lines). The variability in the simulated distributions provides a good visual reference of the similarity between experiment and simulation (Fig. 5AB and S2). The distributions show that an increasing concentration of EB3 decreases the contact duration (Fig. 5BC). In the absence of EB3 the contact duration is 30.8 ± 1.3 seconds (median \pm SE), whereas in the presence of 20, 50, and 100 nM GFP-EB3 the contact duration is reduced to respectively 13.0 ± 0.7 , 9.1 ± 0.8 , and 4.1 ± 0.3 seconds (median \pm SE). The simulated distributions capture the data well and show that free microtubule lifetimes and microtubule stalling can indeed be simultaneously captured with a 1D model comprising three parameters (Fig 5A-C). From the fits, we find that with increasing EB3 concentration, k_{hyd} increases and D_{tip} decreases (Fig. 5C).

Additionally, we find both fully and partially decayed GTP/GDP-Pi intensities at the moment of catastrophe, in agreement with experimentally observed event types (Fig. 5D and 2C). Agreement between the experimental and simulated distributions of the remaining EB3 signal at the moment of catastrophe was ensured with $N_{unstable} = 15$ (Fig. 4C). The mean decay rate of GTP/GDP-Pi subunits during stalling also matches the experimental dataset well and increases with increasing EB3 (Fig. 5E and 2D). The simulated barrier contact events furthermore show a similar noisy comet intensity before catastrophe, confirming that the size of the microtubule stabilizing cap fluctuates with time.

7.2.7 Simulation of tubulin washout

Recent experiments using microfluidics assisted washout of tubulin in vitro have shown that a minimal stable cap has a length of ~ 10 tubulin layers at most, of which 15-30% dimers remain unhydrolysed ([Duellberg et al., 2016a]). The observed delay between tubulin washout and microtubule catastrophe is reported to be ~ 7 seconds ([Walker et al., 1991]) and shown to depend on the pre-washout growth velocity ([Duellberg et al., 2016a]). To verify the ability of our model to describe tubulin washout experiments, we simulated tubulin washout with our obtained parameter set (Fig. 5C). To simulate washout, we prohibit any growth of the microtubule tip after 40 seconds, but still allow microtubules to undergo negat-

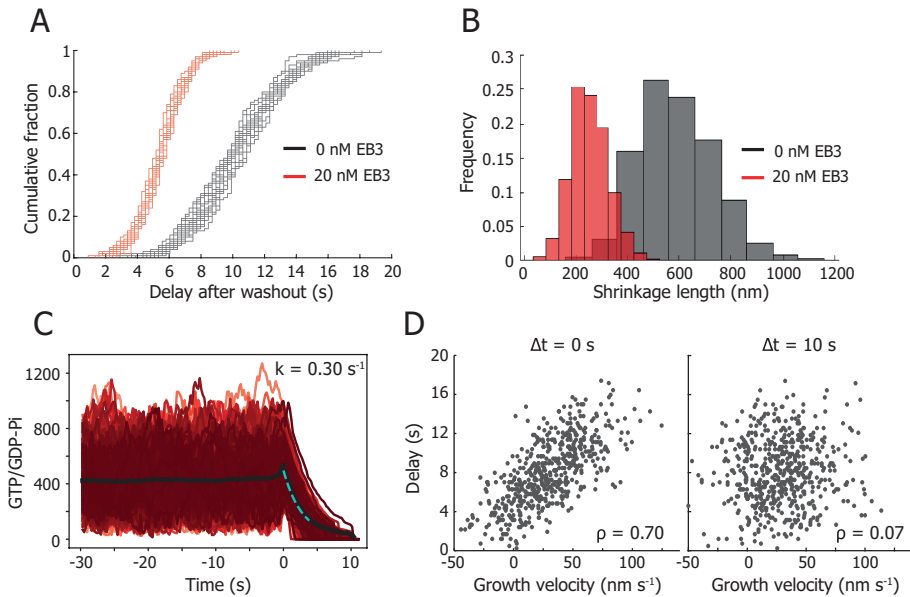


Figure 7.6: Simulating tubulin washout. **A.** Simulation of tubulin washout following the parameters in Fig. 5C for 0 and 20 nM EB3. For both conditions, 25 bootstrapped distributions of 100 data points are shown. The mean delay duration between washout and catastrophe is 10.3 ± 3.2 and 5.5 ± 1.8 seconds for 0 and 20 nM EB3 respectively (mean \pm std). **B.** Simulation of tubulin washout following the parameters in Fig. 5C for 0 and 20 nM EB3. The mean shrinkage length of the microtubule between washout and catastrophe is 588 ± 144 and 253 ± 71 nm respectively (mean \pm std). **C.** Simulation of the number of GTP/GDP-Pi subunits before and during tubulin washout following the parameters in Fig. 5C for 20 nM EB3. Fitting the loss of GTP/GDP-Pi subunits from the moment of washout gives a decay rate of 0.30 s^{-1} . **D.** Scatter plot of the simulated delay time dependency on the growth velocity before tubulin washout. Growth velocities measured immediately before tubulin washout ($\Delta t = 0$ seconds) show a strong correlation, which is lost for growth velocities measured $\Delta t = 10$ seconds before washout. The mean growth velocity is calculated from a 10 second time window. ρ is Spearman's rank correlation coefficient.

ive growth excursions (Fig 3B). To compare our results to published washout parameters (20 μM tubulin with 0 and 200 nM of Mal3) ([Duellberg et al., 2016a]), we simulate tubulin washout for 15 μM tubulin in the presence of 0 and 20 nM EB3, resulting in a comparable growth velocity and hydrolysis rate. The difference between the concentration of Mal3 (fission yeast homolog of EB1) and EB3 required to obtain a similar hydrolysis rate can be explained by the intrinsic structural differences ([Roth et al., 2018, Von Loeffelholz et al., 2017]). Our simulation of tubulin washout showed a delay between washout and catastrophe of 10.2 ± 3.2 and 5.5 ± 1.8 seconds (mean \pm std) for 0 and 20 nM EB3 (Fig. 6A), similar to the reported values of 7.3 and 3.5 seconds for 0 and 200 nM Mal3 ([Duellberg et al., 2016a]). In addition, it was reported that microtubule growth is not simply paused after washout, but that microtubules slowly shrank prior to catastrophe. During the simulated washout delay, we measured a slow decrease in microtubule length of 253 ± 71 nm (mean \pm std) for 20 nM EB3 (Fig. 6B), comparable to the reported 165 ± 105 nm for 200 nM Mal3 ([Duellberg et al., 2016a]). Furthermore, we find that the simulated decay rate of 0.30 s^{-1} (20 nM EB3) of GTP/GDP-Pi subunits from the moment of tubulin washout is in agreement with the reported 0.33 s^{-1} (200 nM Mal3) (Fig. 6C).

Our simulated data also captures the reported positive correlation between microtubule stability and growth velocity (Fig. 6D) ([Duellberg et al., 2016a]). The simulated washout delay increases with an increasing growth velocity as measured immediately prior to washout (Spearman correlation coefficient of $\rho = 0.70$). However, the correlation is lost when the growth velocity is measured 10 seconds before washout ($\rho = 0.07$), in agreement with published results ([Duellberg et al., 2016a]). We conclude that our model is thus capable of accurately capturing tubulin washout experiments.

7.2.8 The 1D model successfully captures the mild catastrophe dependence on microtubule growth rates

As an additional verification of our model, we simulated microtubule lifetimes and stalling durations based on our previous experimental data (Fig. 7) ([Janson et al., 2003]). Our model can simultaneously capture the reported mild reduction in catastrophe rate with increasing growth velocity as well as the distribution of stalling durations (Fig. 7AB). To explain these data, we had to assume a velocity-dependent tip noise (at a fixed k_{hyd} of 0.10 s^{-1}), which is in line with the reported dependence of the tip noise on the growth velocity (Fig. 7C). This relationship shows a linear dependence of the tip noise on the growth velocity, as has been developed for a 1D model ([Gardner et al., 2011b, Rickman et al., 2017]): where a is the size of a dimer, k_a the tubulin addition rate, and k_d the tubulin dissociation rate. We thus conclude that our 1D model can describe the reported mild dependence of the microtubule lifetimes on the growth velocity.

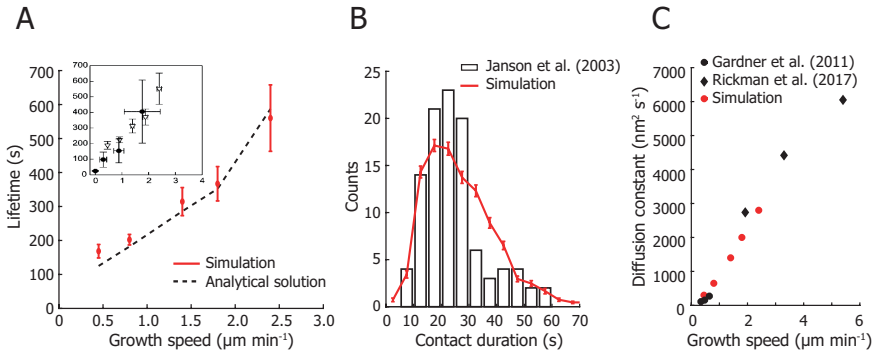


Figure 7.7: Model evaluation. **A.** Simulation of microtubule lifetimes for increasing growth velocities. The simulation growth velocities were obtained from ([Janson et al., 2003]) and combined with a global value for k_{hyd} of 0.10 s^{-1} and the determined $N_{unstable}$ of 15. The insert shows the experimental lifetimes for freely growing microtubules (triangles) and for buckling microtubules (dots) (Janson2003). Our simulation gives a similarly mild suppression of catastrophes with increasing tubulin concentrations, with the growth velocities of 0.45, 0.8, 1.4, 1.8, and $2.4 \mu\text{m min}^{-1}$ corresponding to tubulin concentrations of 7.2 ($n=58$), 10 ($n=152$), 15.2 ($n=49$), 20 ($n=51$), and $28 \mu\text{M}$ ($n=30$). Simulated lifetimes are given as mean \pm SEM with the same number of datapoints as the experimental values. The mild catastrophe suppression is also captured by the analytical solution of our model (see Methods). **B.** Histogram of the pooled stalling duration with 103 events measured at 15.2, 20, and $28 \mu\text{M}$ from (Janson2003) and the simulated stalling duration. The simulated values represent mean \pm std for $n = 103$ events. **C.** The diffusion constant of the microtubule tip required to simulate the microtubule lifetimes in **A.** based on data from (Janson2003). These values agree with reported values by (Gardner2011a, Rickman2017) and follow a linear dependency on the growth speed.

7.3 Discussion

7.3.1 EB3 enhances catastrophes for stalling microtubules

Using novel micro-fabricated barriers in conjunction with TIRF microscopy, we studied the duration of barrier contact as well as the dynamics of the EB3 comet during microtubule stalling. We confirm that stalled microtubules undergo a catastrophe after 30.8 ± 1.3 seconds (median \pm SE) in the absence of EB3, comparable to previously measured values (Fig. 7B) ([Janson et al., 2003]). The presence of EB3 further enhances catastrophes in a concentration dependent manner which results in up to five times shorter microtubule contact times at the barriers (Fig 5A-C). In earlier unpublished experiments, we made similar observations for stalling microtubules in the presence of Mal3 (Fig. S4). These shorter contact times are accompanied by an increase in the decay rate of the EB3 comet (Fig. 2D).

Additionally, we developed a simple phenomenological computational model that predicts catastrophe statistics based on parameters related to random (uncoupled)

GTP hydrolysis and fluctuations in microtubule growth. Fitting the model to the data suggests that the size of the growth fluctuations (D_{tip}) decreases in the presence of EB3 (Fig. 5C). This effect would support the hypothesis that the increase in growth velocity due to the presence of EB3 is the result of a lower tubulin dissociation rate at the microtubule tip. If we assume that the tubulin association rate at the microtubule tip only depends on the soluble tubulin concentration and is therefore not affected by EB3, we would indeed expect the resulting tip noise D_{tip} to be smaller with increasing concentrations of EB3. This effect could originate from EB3 binding in between protofilaments and reducing tip fluctuations or from the hypothesis that EB3 increases the growth velocity by closing the lattice seam ([Zhang et al., 2015]).

7.3.2 A 1D phenomenological model successfully describes microtubule lifetimes, stalling, and tubulin washout

We developed a simple phenomenological computational model that can capture a very rich set of experimental data on dynamic microtubules. Its sole dependence on (velocity-dependent) tip noise and random hydrolysis makes it possible to build an intuition of key processes in microtubule dynamics, in particular the onset of catastrophe. We find that our model can reproduce both the experimental microtubule stalling duration and the accompanying EB comet decay rate (Fig 5). At the same time, our model captures the reported mild reduction in catastrophe rate with increasing growth velocity as well as the distribution of stalling durations (Fig. 7AB). Previous 1D models were not able to describe both the mild catastrophe dependence on microtubule growth rates and the size of the stabilizing cap ([Brun et al., 2009, Flyvbjerg et al., 1996]). A reason for this was the assumption that tubulin dissociation is independent from the microtubule growth velocity ([Bowne-Anderson et al., 2013]). This necessitated introducing lateral tubulin-tubulin interactions in a 2D model to accurately capture microtubule lifetimes and cap dynamics ([Brun et al., 2009, Gardner et al., 2011b]). Here, we showed that introducing a highly dynamic tip in a 1D model is sufficient to accurately capture both the microtubule lifetimes as well as the size of the stabilizing cap. The magnitude of the required simulated tip noise would not be observable using fluorescence microscopy, but only with optical tweezers ([Gardner et al., 2011b, Kerssemakers et al., 2006, Schek et al., 2007]). The extend of any “blurring” of the microtubule tip due to tip noise during frame acquisition would remain below the observable optical resolution (Fig. S6D).

We furthermore showed that our model can capture tubulin washout and reproduces a similar catastrophe delay, tip shrinkage, and comet decay as previously reported (Fig. 6) ([Duellberg et al., 2016a]). Our model also produces the same correlation between washout delays and growth velocity as was recently observed experimentally ([Duellberg et al., 2016a]) and thus captures the reported momentary nature of microtubule stability. We conclude that our model can describe tubulin washout and simulate values in good agreement with experiments.

7.3.3 MT stability depends on the distribution of hydrolysed dimers at the tip

The decay of the EB3 comet during barrier contact can provide further insights into the criterium for microtubule stability. We find that microtubules can remain in a stalled state without the presence of an observable EB3 comet both in our experiments and simulations (compare Fig. 2C and 5D). This suggests that a stalled microtubule does not necessarily require a number of GTP/GDP-Pi subunits that is large enough to be observed as a comet. The effect is explained by the presence of growth fluctuations during microtubule stalling. Hydrolysed subunits at the tip are continually replaced by newly incorporated unhydrolysed subunits, reducing the probability of reaching the critical threshold of $N_{unstable}$ at the microtubule tip. This phenomenon could also account for reported pausing events during which a microtubule temporarily stops growing without triggering a catastrophe ([Van-Buren et al., 2005]). It illustrates that the onset of a catastrophe is not fully coupled to the presence of an observable comet.

To determine the stretch of hydrolysed subunits at the microtubule tip required to initiate a catastrophe ($N_{unstable}$), we measured the ratio between the EB3 comet intensity at the moment of catastrophe and the mean EB3 comet intensity during steady-state growth (Fig. 4BC). In parallel, we evaluated the decay rates of EB3 comets after initial barrier contact. Both measures converge on a catastrophe threshold $N_{unstable}$ of ~ 15 uninterrupted hydrolysed terminal subunits, which would approximate a single tubulin layer at the tip of a real 3D microtubule, in line with experimental observations ([Caplow and Shanks, 1996, Drechsel and Kirschner, 1994]). A recent finding from washout experiments showing that a microtubule requires a stable cap of ~ 10 tubulin layers at most ([Duellberg et al., 2016a]) is not at odds with our finding that a catastrophe is triggered when the terminal layer of tubulin is hydrolysed. Because the former result is based on the average remaining density of Mal3 at the moment of catastrophe after tubulin washout, it does not inform on a specific catastrophe criterium. The notion that the stabilizing cap (L_{cap}) and the EB3 comet (GTP/GDP-Pi region) are large on average, but that only a short stretch of hydrolysed subunits at the microtubule tip is required to trigger a catastrophe, reconciles short and long cap observations ([Brun et al., 2009, Duellberg et al., 2016a, Molodtsov et al., 2005b, Seetapun et al., 2012, Walker et al., 1991]). We thus find that the stability of a microtubule does not primarily depend on the size of the observed EB comet, but instead on the underlying distribution of hydrolysed subunits at the microtubule tip.

7.3.4 Both the cap size and tip fluctuations determine the onset of catastrophe

To better understand the size of the stabilizing cap (L_{cap}) and its effect on the catastrophe frequency, we derived an analytical expression for the position of the sequence of hydrolysed subunits equal or greater than $N_{unstable}$ (see Methods for details). This position is determined by $N_{unstable}$ and the underlying distribution of hydrolysed subunits. We assume that the density of unhydrolysed dimers de-

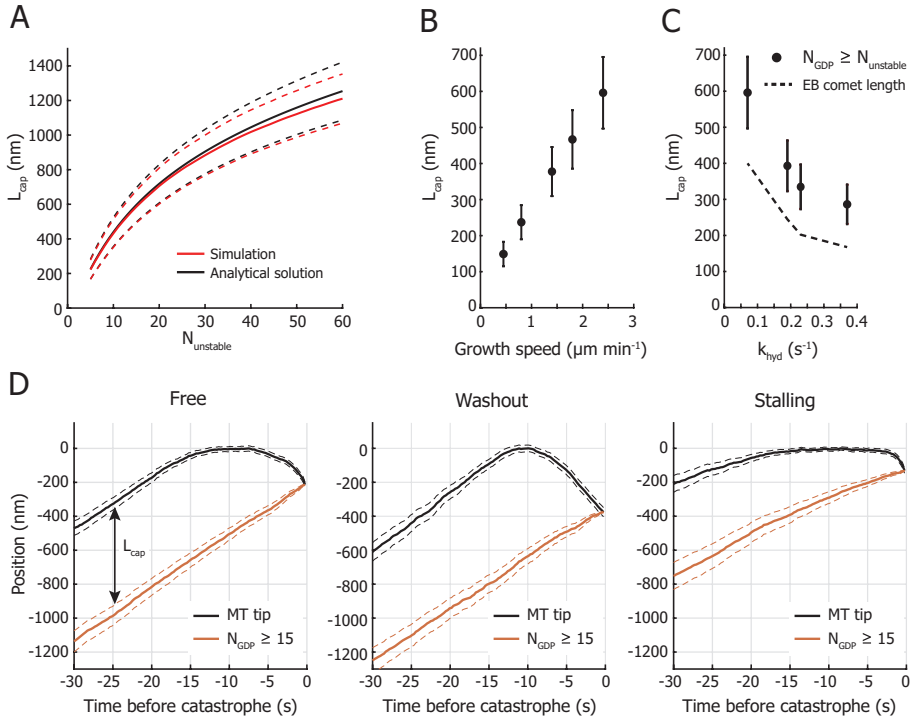


Figure 7.8: Fluctuations of the stabilizing cap trigger catastrophes. **A.** Dependence of the cap length L_{cap} on $N_{unstable}$ (mean \pm std). The simulated cap length and the numerical solution based on the analytical model are in good agreement. The shown cap length was determined for the parameters of 0 nM EB3 in Fig. 5C. **B.** The length of the stabilizing cap L_{cap} depends linearly on the growth velocity $\langle V \rangle$. The cap length was calculated with the analytical model (mean \pm std) and required a constant k_{hyd} of 0.1 s^{-1} and an $N_{unstable}$ of 15, equal to the simulation parameters based on the data from (Janson2003) (see Fig 7B). **C.** The mean length of the stabilizing cap L_{cap} decreases with increasing hydrolysis rate k_{hyd} . The dependence of the cap size on the hydrolysis rate is calculated with the analytical model (mean \pm std) and is based on the parameters of the EB concentrations 0, 20, 50, and 100 nM in Fig 5C. The size of the stabilizing cap based on the position of the sequence $N_{unstable}$ is larger than the stabilizing cap based on the characteristic length of the EB signal (GTP/GDP-Pi region). **D.** Simulation of the position of the microtubule tip and of the position of the sequence of hydrolysed subunits defined by $N_{unstable} = 15$ prior to catastrophe. Mean traces are for catastrophes during microtubule free growth, after tubulin washout, and during microtubule stalling (mean \pm SE). Before the onset of catastrophe, the mean cap length L_{cap} is constant during steady-state growth as both the position of the tip and the end of the cap move with equal velocity $\langle V \rangle$. A catastrophe is triggered when $L_{cap} = 0$, which is predominantly determined by persistent negative growth excursions of the microtubule tip. All simulations were performed with the parameters for 0 nM EB (Fig. 5C)

creases exponentially along the microtubule lattice and is fully characterized by k_{hyd} and $\langle V \rangle$ ([Duellberg et al., 2016a, Maurer et al., 2014, Seetapun et al., 2012]). By treating the microtubule lattice as a series of independent Bernoulli trials, we can obtain an expression for the mean position of the first occurrence of a series of hydrolysed subunits equal or greater than $N_{unstable}$ (Fig. 8A and S5AB). The distance between the microtubule tip and this position is equal to the size of the stabilizing cap, which means we can obtain the relation between the size of the stabilizing cap and the parameters $N_{unstable}$, k_{hyd} , and $\langle V \rangle$ (Fig. 8BC and S5B). We find that the size of the stabilizing cap scales linearly with the growth velocity $\langle V \rangle$ (Fig. 8B). The addition of EB3 however affects both the growth velocity and the hydrolysis rate, the combined effect of which results in a decreasing cap size with increasing EB concentration (Fig. 8C). We can calculate the mean size of the stabilizing cap in our model based on k_{hyd} , $\langle V \rangle$, and $N_{unstable}$ and compare it to the length of the GTP/GDP-Pi region for which the EB comet signal is a proxy. Taking as the characteristic length of the EB comet ([Duellberg et al., 2016a, Rickman et al., 2017]), we find that the comet underestimates the size of the calculated stabilizing cap (Fig 8C).

Having an expression for the size of the stabilizing cap, we can now explore an intuitive view on how a catastrophe is triggered. The length of the cap is determined by two competing processes on either end, namely noisy growth at the microtubule tip and hydrolysis in the lattice. During steady-state growth, the mean length of the stabilizing cap has a constant size determined by the growth velocity $\langle V \rangle$ and hydrolysis rate k_{hyd} ([Duellberg et al., 2016a]). We observe in our simulations that catastrophes for freely growing microtubules occur as a result of a short period of slowed down or negative growth (Fig 8D left and S3C), in agreement with previous experimental observations (compare Fig. S3 with Fig. 7 in ([Maurer et al., 2014])). This shows that the onset of catastrophe is determined by the probability that growth fluctuations remove the stabilizing cap. When we treat the probability for a catastrophe as the probability for negative growth excursions to exceed the length of the stabilizing cap, the microtubule lifetimes are successfully reproduced with the analytical solution (Fig 7A and S5D). This holds true for catastrophes during free growth and after tubulin washout (Fig 8D left and middle). During microtubule stalling however, continuing tip fluctuations replace hydrolysed subunits at the tip for unhydrolysed subunits, reducing the effective mean hydrolysis rate. This results in slowing down of the cap end and delaying the onset of catastrophe (Fig. 8D right). Additionally, the longer catastrophe delay observed with microtubule stalling compared to tubulin washout can be explained by the different effective tip fluctuations. After tubulin washout, loss of the stabilizing cap is caused by both continued hydrolysis and the irreversible loss of tubulin subunits at the tip, whereas the tip of a stalling microtubule can still recover after loss of terminal subunits through tubulin addition and continue to fluctuate (Fig. 8D).

7.3.5 MT ageing is not required to describe microtubule lifetimes

An observed feature of microtubule stability lacking in our model is an age-dependent catastrophe frequency. It has been reported that “younger” microtu-

bules are more stable than “older” ones ([Gardner et al., 2011b, Odde et al., 1995]). Ageing has also been observed through a gradual reduction of the EB comet intensity during steady-state growth ([Maurer et al., 2012, Mohan et al., 2013]) and through shorter catastrophe delays after tubulin washout for older microtubules ([Duellberg et al., 2016b]). The two proposed processes responsible for inferring ageing are either based on a multi-step lattice defect model ([Bowne-Anderson et al., 2013, Mohan et al., 2013]) or on tapering of the microtubule tip during growth ([Chretien et al., 1995, Coombes et al., 2013, Duellberg et al., 2016b, VanBuren et al., 2005]). Invariably, these mechanisms are tightly coupled to the onset of a catastrophe and are required to understand microtubule lifetimes. In our model however, we find that the onset of a catastrophe is independent from microtubule ageing.

Microtubule ageing is generally characterized by fitting lifetime distributions to a Gamma distribution to obtain the shape parameter, a measure for the number of sequential steps required to trigger a catastrophe ([Gardner et al., 2011b, Odde et al., 1995]). In our experimental lifetime distribution, we find that the Gamma shape parameter is independent from the EB concentration (Fig. S6A), in line with previous reports ([Mohan et al., 2013]). To account for microtubule ageing in our model, we introduced time-dependent tip fluctuations (Fig. S6B). Increasing the growth fluctuations with time while keeping the mean growth velocity constant, increases the probability of reducing the stabilizing cap to zero due to an increase in negative growth excursions. By increasing D_{tip} with a rate of 0.025 s^{-1} following a bounded exponential curve, we can reproduce the experimental ageing parameters (Fig. S6C). Linking microtubule ageing to an increase in tip noise and not to the hydrolysis rate or to the accumulation of defects in the microtubule lattice also agrees with previous studies. It was reported that microtubule ageing is in fact correlated with the frequency of encountering curled protofilaments ([Zakharov et al., 2015]), an effect that can be represented with our phenomenological description of increasing tip noise ([Mcintosh et al., 2018]). So, although microtubule ageing is not required to accurately capture microtubule lifetimes, it can be easily incorporated by introducing time-dependent tip fluctuations.

7.3.6 Outlook

Our experimental setup will be useful for studying microtubule interactions and the functional effect of stabilizing and destabilizing microtubule associated proteins. Our approach can be used to study the influence of MAPs ([Meadows et al., 2018]), tubulin isoforms and PTMs ([Sirajuddin et al., 2014]) on the stability of pushing microtubules. Furthermore, the SiC overhangs are designed to be compatible with a previously published method to specifically functionalize the barriers with protein complexes ([Taberner et al., 2014]), enabling the study of microtubule end-on interactions with TIRF microscopy ([Vleugel et al., 2016]).

A possible extension of our 1D model to describe the effect of +TIPs on microtubule dynamics in general could be to characterize them phenomenologically by their effect on GTP hydrolysis and tip fluctuations. As the effect of EB3 can be de-

scribed this way, we hypothesize that the effect of other microtubule associated proteins can be characterized similarly. To allow future extensions and modifications of our model, we have made the simulation source code available under an open-source licence on GitHub (<https://github.com/florian-huber/mtdynamics>) with extra documentation.

7.4 Methods

Proteins

GFP-EB3 was a kind gift from Michel Steinmetz. All tubulin products were acquired from Cytoskeleton Inc, with all unlabelled tubulin specifically from a single lot.

Microfabrication of barriers

The fabrication method for the micro-fabricated barriers with an SiC overhang is inspired by ([Kalisch et al., 2011, Taberner et al., 2014, Aher et al., 2018]). All fabrication steps were performed in a cleanroom environment (van Leeuwenhoek Laboratory, NanoLab NL). The barrier was designed with the following considerations in mind:

- The width of the channels should favour stalling events over buckling events, but remain large enough for GMPCPP-stabilized seeds to easily land.
- A bottom layer of SiC is needed to prevent etching into the coverslip during a Buffered Oxide Etch. This layer needs to be as thin as possible to prevent photon absorption by the semiconductor resulting in a diminished signal-to-noise and surface heating. Although SiC is transparent for wavelengths $> 0.5 \mu\text{m}$, its bandgap of $\sim 2.8 \text{ eV}$ can result in photon absorption for the commonly used 405 and 488 nm lasers ([Pham, 2004]). Using PE-CVD, 10 nm is thinnest layer we could fabricate while still maintaining the layer's integrity to protect the coverslip from the Buffered Oxide Etch.
- The layer of SiO₂ of 100 nm ensures that the microtubule can polymerize underneath the overhang while remaining inside the evanescent wave.
- The top layer of SiC is 250 nm thick to ensure mechanical stability, while still allowing to observe microtubules growing on top of the barrier despite some photon absorption.

To start, glass coverslips (24×24 mm, #1) were cleaned for 10 min with base piranha, a mixture of H₂O:NH₄OH:H₂O₂ in a 5:1:1 ratio heated to 70°C. Then, three sequential layers of SiC (10 nm), SiO₂ (100 nm), and SiC (250 nm) are deposited on the cleaned surface via Plasma-Enhanced Chemical Vapour Deposition (PE-CVD) at 300°C (Oxford Instruments PlasmaPro 80). PE-CVD ensures a surface smooth enough for TIRF microscopy with fast deposition rates (70 nm/min for SiO₂ and 40 nm/min for SiC).

In order to transfer the barrier pattern to the surface, UV lithography is used. First,

to aid in the adhesion of the photoresist, a few drops of hexamethyldisilazane (HMDS) are spin coated on the SiC surface and allowed to dry on a 115°C hotplate for 30 seconds. Then a 1.3 µm layer of the positive photoresist S1813 (MicroChem) is spin coated (5000rpm) on the surface and pre-baked for 90 seconds on a 115°C hotplate. Exposure of the photoresist through a chromium mask with a near-UV source (320-365 nm, approx. 13 mW/cm²) transfers the barrier pattern in 4 seconds (EVgroup EVG 620). Development with MF321 (MicroPosit) for 60 seconds removes the UV-exposed regions of the resist.

Next, Reactive Ion Etching (Leybold Hereaus) with a mixture of CHF₃:O₂ (50 sccm:2.5 sccm) etches through the exposed regions of the 250 nm SiC layer and into the SiO₂ layer. The etch is performed at 50 µbar and at 100 W, resulting in a bias voltage of 400 V. It is important to etch completely through the top SiC layer, but only partly through the SiO₂ layer, to leave the bottom SiC layer intact. Any remaining photoresist after the etch is removed by sonication of the sample in acetone for 10 minutes.

Finally, the sample is submerged in buffered hydrofluoric acid (HF:NH₄F = 12.5:87.5%) to selectively etch the exposed SiO₂ with a rate of approximately 200 nm/min to obtain an overhang of 1.5 µm. The final barriers are 100 nm high with an overhang of 1.5 µm, enclosing channels with a width of 15 µm.

***In vitro* microtubule dynamics assay**

Reconstitution of microtubule dynamics was performed as previously described in ([Bieling et al., 2007, Gouveia et al., 2010]). After cleaning the barrier sample with O₂-plasma, a flow channel was constructed with a cleaned glass slide and double-sided sticky tape in such a way that the channel direction is perpendicular to the barriers. Then, the surface was consecutively functionalized with 0.5 mg/ml PLL-PEG-biotin(20%) (SuSoS AG, Switzerland), 0.2 mg/ml NeutrAvidin (Invitrogen), and 0.5 mg/ml κ-casein (Sigma). All components were kept in MRB80 buffer, comprised of 80mM piperazine-N,N'-bis(2-ethanesulfonic acid), 4mM MgCl₂, and 1mM EGTA at a pH of 6.8. The reaction mixture contained 15 µM tubulin (7% rhodamine labelled) in the presence of GFP-EB3 or Hilyte488 labelled tubulin in the absence of GFP-EB3, supplemented with 0.5 mg/ml κ-casein, 0.15% methylcellulose, 50 mM KCl, 1 mM GTP, oxygen scavenger mix (4 mM DTT, 200 µg/ml catalase, 400 µg/ml glucose oxidase, 50mM glucose). The reaction mix is then centrifuged in an Airfuge (Beckman Coulter) at 30psi for 8 minutes to remove any aggregated complexes before being introduced to the sample. GMPCPP-stabilized seeds (70% unlabelled tubulin, 18% biotinylated tubulin, 12% rhodamine-labelled tubulin) were introduced to the channel with the flow direction perpendicular to the barriers. Flow cells were sealed with vacuum grease and imaged on a TIRF microscope at 28-30°C.

TIRF microscopy

All experiments were imaged using TIRF microscopy, consisting of an Ilas² system (Roper Scientific) on a Nikon Ti-E inverted microscope. The Ilas² system is

a dual illuminator for azimuthal spinning TIRF illumination equipped with a 150 mW 488 nm laser, a 100 mW 561 nm laser, and a ZT405/488/561/640rpc dichroic mirror. Simultaneous dual-acquisition was performed with two Evolve 512 EMCCD camera's (Photometrics) through a 525/50 nm and a 609/54 emission filter, using a Nikon CFI Plan Apochromat 100XH NA1.45 TIRF oil objective. Together with an additional magnifying lens, the final magnification resulted in a pixel size of 107 nm/pixel. The sample was heated with a custom objective heater to 28-30°C and was kept in focus with the Nikon Perfect Focus system. The hardware was controlled with MetaMorph 7.8.8.0 (Molecular Device).

Image treatment

The image stacks obtained with TIRF microscopy were corrected prior to data analysis. First, simultaneous acquisition of rhodamine-labelled tubulin and GFP-EB3 on two cameras introduced a non-linear spatial offset between the two image stacks due to imperfections in the dichroic mirror and in the alignment of the two cameras. By scanning multiple FOVs of a calibration slide containing 100 nm TetraSpeck beads (ThermoFisher) and automatically locating the centroids through a custom written MATLAB script, a non-linear registration profile accounting for the spatial offset was calculated. The misaligned image stack was corrected by applying this registration profile based on the position of ~500 bead positions. Additionally, any sample drift was corrected by subpixel image registration through cross-correlation ([Guzar-Sicairos et al., 2008]).

Secondly, some scattering of excitation light at the edge of the SiC overhang made proper determination of the GFP-EB3 signal near the barrier difficult. Although this effect was mostly mediated by creating a wide undercut that physically separated the edge of the overhang from the barrier, a correction was nonetheless applied. To correct the signal, the minimum intensity value of each pixel in the image stack was subtracted from that pixel in each image. This correction enabled tracking of the EB3 comet near the barrier and accurate measurement of the EB3 comet intensity. Thirdly, a general background subtraction was performed in Fiji ([Schindelin et al., 2012]) to correct for inhomogeneous illumination.

Image analysis

Analysis of the images was partly performed with Fiji and with MATLAB. After the image treatment described above, kymographs were created by drawing straight lines of 9-pixel width (0.95 μm) along growing microtubules using KymoResliceWide plugin with maximum transverse intensity (<http://fiji.sc/KymoResliceWide>). Each growth event in the kymographs was manually traced to determine the position of the microtubule tip. This position was then used to fit the EB3 comet to obtain its position and intensity, using the intensity profile:

$$I(x) = I_A \cdot \exp\left(-\frac{(x - x_c)^2}{\sigma^2}\right) + I_{bkg}$$

where $I(x)$ is the fluorescence intensity, I_{bkg} is the background intensity, I_A is the intensity amplitude, x_c is the position of the peak of the EB3 comet, and σ is the width of the EB3 comet. As EB3 comet decay at the barrier makes fitting impossible, the intensity during contact was determined by calculating the average intensity value in a region around the comet position and around the barrier (Fig. S1C). The barrier contact duration and comet decay duration were determined manually.

Monte Carlo simulations

Simulations of growing microtubules were run as a series of discrete, fixed time-steps. The length of the time steps δt was chosen small enough to properly account for the random hydrolysis of the subunits (P_{hyd} , the probability for a dimer to undergo hydrolysis within one timestep was kept at <0.05). Further restrictions were to not exceed the desired framerate, in our case the lowest used experimental frame rate of 250 ms. Due to the discrete nature of microtubule growth in subunits, the next-lowest time-step for which $\langle V \rangle \delta t / L_0$ became an integer was chosen, with $L_0 = 8/13$ nm the length increment per subunit and $\langle V \rangle$ the microtubule mean growth velocity.

Each microtubule simulation started from a few initial subunits (a ‘seed’) that were excluded from hydrolysis, and that were not allowed to be removed during microtubule tip fluctuations. Microtubule growth was simulated as a discrete, biased, Gaussian random walk. This means that for each time-step δt , the microtubule length was changed by a discretized random number of subunits that was drawn from a Gaussian distribution with standard deviation $\sigma = \sqrt{2D_{tip}\delta t}$ and centered at $\langle dx \rangle / L_0$.

During each time step, subunits transition from the GTP/GDP-Pi to the GDP state by random hydrolysis with a rate k_{hyd} . Whenever the foremost uninterrupted strand of GDP state subunits ($\geq N_{unstable}$ subunits in a row) is changed, the position of the end of the stable cap will jump to the front element of this strand, which we interpret as the new position of the end of the stable cap $L_{end-of-cap}$.

A simulation run ends when a catastrophe occurs. This happens when the stable cap shrinks to zero, i.e. if $L_{tip} - L_{end-of-cap} = 0$, where L_{tip} is defined as the position of the foremost subunit of the microtubule. The growth duration was defined as the time from initial growth until catastrophe. To exclude nucleation kinetics from the simulated lifetimes, a microtubule is considered to grow after reaching a length of 250 nm.

The presence of a physical barrier is modelled by introducing a fixed barrier position $L_{barrier}$. Tip dynamics and random hydrolysis remained unchanged, only the microtubule length was truncated whenever it would penetrate the barrier. This means the length of the microtubule was set back to $L_{barrier}$ if $L_{tip} > L_{barrier}$. The barrier contact time was then defined as the time from the microtubules first contact with the barrier until its catastrophe. The simulation was written in Python 3.6 and run on standard PCs. The code to run the simulation is available under an open-license on GitHub (<https://github.com/florian-huber/mtdynamics>).

Author contributions, acknowledgements and further information

M.K. designed and fabricated the micro-fabricated barriers, performed experiments with EB and analysed the data, developed the analytical solution, and ran simulations. F.H. developed the 1D microtubule model, wrote the simulation code and ran and analysed the simulations. S.K. performed and analysed the experiments with Mal3. M.K, F.H., and M.D. wrote the paper. M.D. coordinated the project.

We thank M.O. Steinmetz for the gift of GFP-EB3 and the technicians of the van Leeuwenhoek Laboratory for their technical assistance in the fabrication of the barriers. We thank Vladimir Volkov and Louis Reese for discussions and critical reading of the manuscript and Seungkyu Ha for his assistance in acquiring the SEM images. This work was supported by the European Research Council Synergy grant 6098822 to Marileen Dogterom.

This chapter was published as a preprint on the *bioRxiv* Website [Kok et al., 2021]. An analytical expression for the size of the stabilizing cap and for the catastrophe probability and microtubule lifetimes, as well as supplementary figures and videos, can be found on the same website.



Final considerations and new research directions

This thesis gave a close-up view on microtubule catastrophes. We examined how forces and end-binding proteins affect the transition from growth to shrinkage. By using different methods ranging from quantitative and qualitative fluorescence intensity measurements to high-resolution optical tweezers experiments we targeted our research questions from different directions. Here we want to remark on our data and analysis and show preliminary observations connected to this topic. Besides, we present new research ideas emerging from our current experiments.

8.1 EB intensity

In order to understand the effect of end-binding proteins on microtubule (MT) dynamics we first examined the binding of the end-binding protein (EB) mal3 to MT ends, see chapter 3. We observed that mal3 intensity decreased on average several seconds before catastrophe which we explained with the disappearance of binding sites as a step towards catastrophe [Maurer et al., 2012]. While performing our experiments we identified three interesting future lines of investigations.

8.1.1 Mal3 intensity reflects the growth speed of MTs

Microtubule (MT) growth speed can be increased by elevating the mal3 concentration in the buffer (up to saturating conditions, $\sim 200\text{nM}$ mal3) [Munteanu, 2008, Vitre et al., 2008]. This change of concentration is accompanied with an increased mal3 comet intensity, both in width and peak intensity of the comet [Munteanu, 2008]. As a result we wondered about a possible correlation between the instantaneous MT growth speed and the mal3 comet intensity. To clarify this issue we calculated the MT growth speed during each phase of free, constant growth. Next, we determined for each of these phases an average mal3 intensity (methods in chapter 3, page 105ff.). The resulting plot is shown in figure 8.1. To get a better overview we also grouped the intensities in speed intervals of same width and determined for each interval a time-weighted average. We see that with an increasing growth speed also the mal3 intensity increased, up to a growth speed of approximately $5\ \mu\text{m}/\text{min}$. Above this we cannot see a clear relationship which is possibly

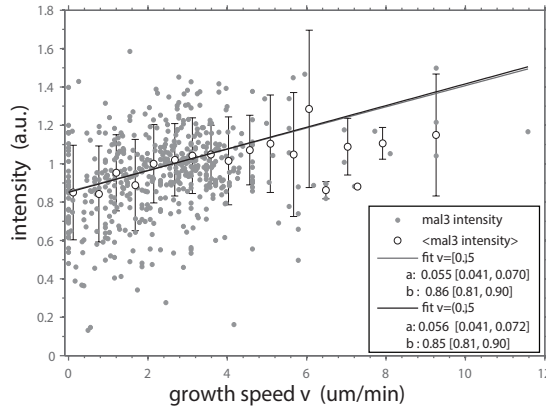


Figure 8.1: Mal3 intensity reflects the MT growth speed. For each interval during which the MT grew with constant speed we determined the average mal3-alexa488 intensity and MT growth speed (grey circles). We fitted the unbinned data with a linear function as first approximation, in the growth speed interval zero to 5 $\mu\text{m}/\text{min}$ (grey line) and the same interval excluding zero (black line). For better view we grouped the data into intervals of constant width and determined for each interval a time-weighted average (open circles). The fit results are presented in the legend for a linear function $y(x)=ax+b$, with the 95 % confidence intervals in square brackets.

due to a saturation of the mal3 binding sites [Bieling et al., 2007, Munteanu, 2008] and also due to limited statistics. To quantify the relationship, we fitted the unbinned data, as a first approximation, with a linear fit. More precisely, we fitted in the range 0 to 5 $\mu\text{m}/\text{min}$ and see a clear trend. We therefore suggest that growth speed is correlated with mal3 binding.

8.1.2 Correlated dynamics of end-binding proteins

To get a better picture of the regulatory effect of individual EBs we examined the correlated dynamics of mal3 and tip1 at MT ends. For analysis we proceeded as explained in section 3.2.2 with the difference of using mal3-mCherry and adding tea2 and tip1-GFP. Example kymographs are shown in figure 8.2a-c. The MT was not labelled for faster imaging purposes. As we could hence not identify the MT tip but only the EB comet, we could not exactly assess the instant of catastrophe. Instead, we defined by eye the time point when the tip1 intensity started reducing. As a consequence we also aligned the seventeen traces by the loss of the tip1 signal. As shown in figure 8.2d., both traces are similar to the one observed in the presence of only mal3 (fig. 3.5, page 31). Also here we observe a decrease of intensity, however it lasts only approximately 5 s. We believe that this results mainly from aligning the traces with the loss of tip1 signal instead of with catastrophe. Besides, all data stems from one single field of view and excludes therefore slight concentration and imaging differences. From the mal3 trace and previous results (chapter 3 and [Maurer et al., 2012]) we can estimate the moment of catastrophe to happen

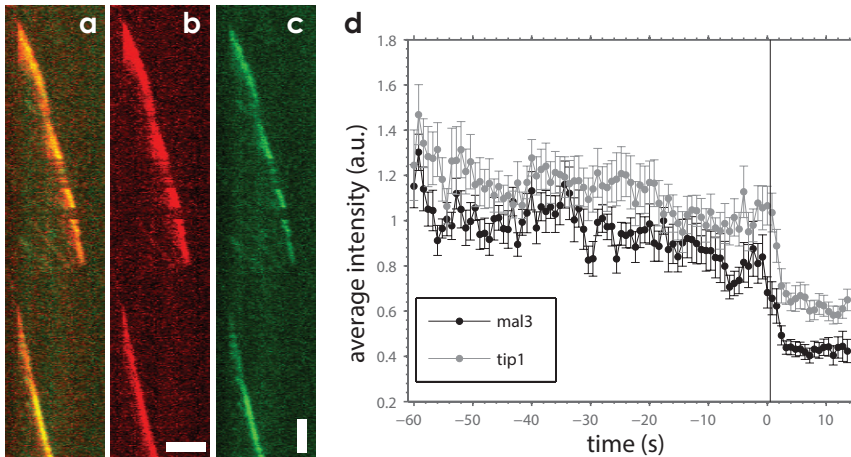


Figure 8.2: Protein intensities at MT ends during free growth. **a.** A colour-merge kymograph demonstrates a fluorescent mal3-mCherry and tip1-GFP comet at the tip of a dynamic MT. The MT grows from the seed and undergoes catastrophe which is accompanied by the loss of the EBs. Shortly afterwards, the MT renucleates from the seed. Vertical dark lines appearing abruptly in the comet are very likely caused by the MT being out of focus. They are not to be confused with a decreased affinity of the EBs to the MT tip. **b.** The same kymograph presenting only the mal3-mCherry signal and **c.** the tip1-GFP signal. Horizontal scale bar is 4 μm and the vertical one 25 s. **d.** We determined the maximum fluorescent intensity from a four-pixel long region at the MT tip. Here we show the average intensity, obtained from seventeen traces from one field of view, aligned at the sudden reduction of the tip1 signal (black vertical line). For the sake of faster imaging we did not label the MT fluorescently and could therefore not determine the exact time of catastrophe. Our data hence shows the tip1 binding dynamics with respect to mal3. On average, we observe the loss of mal3 followed by the one of tip1.

after the average mal3 intensity began decreasing. Interestingly, we see a small delay in the reduction of the tip1 signal compared to the mal3 signal (in the order of two seconds). We think that this is not solely caused by the delay in recording the two colours, which is here 0.3 s. Since tip1 and tea2 are thought to be able to proceed autonomously to the MT tip [Bieling et al., 2007], we also imagine that tip1 can bind directly to the MT tip and does not necessarily need mal3. This has also been shown experimentally for the tip1-homologue Clip170 [Bieling et al., 2008]. It was thought not to associate with EB1 to the MT end, but to use a structural recognition mechanism. Since tip1 contains a structural domain which allows it to bind directly to α -tubulin we also suggest that tip1 recognises a structure at the MT tip rather than or besides binding directly to mal3. As explained, we envision mal3 to catalyse a structural change in the MT tip before catastrophe. The omission of this structure might also result in the loss of tip1 from the MT end. Why there remains the short delay in tip1 loss compared to mal3 loss remains to be elucidated. Possibilities are that the tip1-binding region is further away from the MT tip than is the mal3-binding region or that tea2/tip1 binding is not as critical to

the conformational state of the MT.

Our experiments only obtain information from the total EB intensity in the comet. One approach to learn more about the loss of mal3 (and/or tip1) from the MT end prior to catastrophe involves experiments with the same concentration of mal3 but a low fraction of labelled mal3. By doing single-molecule measurements at high time resolution we might be able to gain more information about the change of the MT comet. More precisely, we could learn about the change in width and length of the comet and also whether the mal3 binding region is different with respect to the one of tip1 or other end-binding proteins. Further, we might be able to deduce the internal dynamics in the comet such as whether mal3 unbinds from the MT tip or from the lattice end.

8.2 The catastrophe process

In chapters 4 and 5 we determined catastrophe time distributions of free MTs and those stalling at a barrier. We suggested catastrophes of free MTs to be comprised of two steps in the absence and presence of EBs with a longer step followed by a shorter one. Combined with the results from chapter 3 we proposed that the shorter step is characterised by the transformational change of the EB-competent state into the GDP-state.

MTs under force underwent a catastrophe faster than when there was no force present. Moreover, there was also a clear change when we added EBs: the histogram of catastrophe times shifted from a peaked multistep distribution to an exponential single-step one. Our explanation is that the force puts EB-decorated MTs immediately into the "ready-for-catastrophe" state where only one more event provokes transition to disassembly.

In the following we discuss our results and its implications on our view of MT assembly and disassembly.

8.2.1 Catastrophes: the underlying distribution

We fitted our data with four (truncated) probability density functions (pdfs):

- gamma distribution: consecutive steps have the same timescale
- two-step exponential distribution: two consecutive steps are not restricted to have the same timescale
- parallel two-step exponential distribution: two parallel/competing steps are not restricted to have the same timescale
- parallel multistep exponential distribution: parallel steps of equal timescale

In all of these distributions the steps are considered irreversible. Therefore we described a further distribution with the possibility of a backward step where an already performed step can be made undone. We did not fit our data with such a distribution since it contains more variables than we can deduce from our data. Here, however, we want to think about the consequences of such a process.

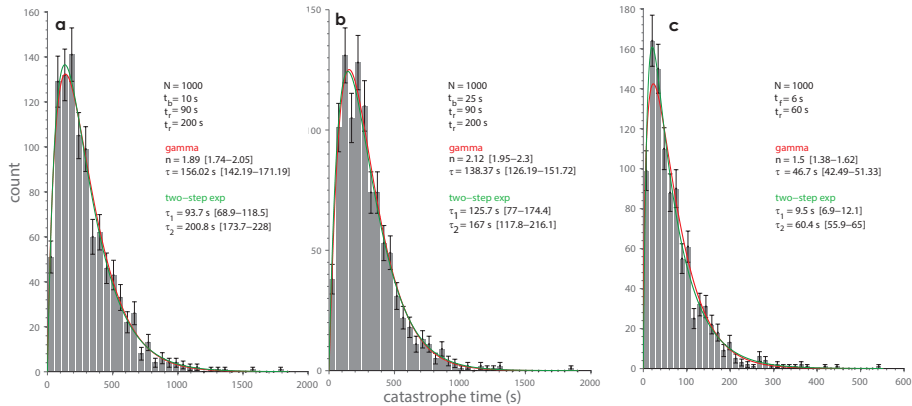


Figure 8.3: Simulated catastrophe time histograms for models introducing either a reversible step or a fixed-duration step. a-b. We assume a distribution describing a process with two random forward steps of duration t_f where the first step can be reversible with a timescale t_b . (A similar reaction with only irreversible forward steps is displayed in figure 4.5c.) The timescales for each step are presented by random numbers generated from an exponential distribution. **c.** This distribution is composed of a short, fixed step of duration t_f and a random long-term step of timescale t_r . Also here the random number was generated from an exponential distribution while the fixed-duration step was chosen. These generated or chosen numbers present the steps of the catastrophe process and were added up to obtain a catastrophe time, representing the duration of the total reaction (for a detailed explanation see section 8.3.2). Here we show the histograms of, in each case, thousand catastrophe times where the bin sizes are determined objectively [Freedman and Diaconis, 1981]. The unbinned data was fitted with gamma and two-step exponential distributions. The fit results are shown in the figure with the 95% confidence intervals in square brackets.

To get a better view of the consequences of a reversible process we simulated a distribution containing one backward step, see fig. 8.3a-b. These distributions, compared to our data obtained from free MTs in only tubulin (fig. 4.4a., page 41), display a wider peak and more apparent steps (gamma distribution), provided the backward step lasts longer than ten seconds. We can therefore not fully exclude a fast backward step in the catastrophe process. However, since in this case the reaction would be dominated by the longer forward steps the simplification to a two-step process is reasonable.

Common to all distributions is that the steps are thought to occur randomly. More specifically, the time point characterised by the transition from one state to the next takes place randomly. However, the assumption of random events does not necessarily need to be correct. It is also possible that one of the steps happens gradually. For example, assuming that after a first, random step the MT was in an intermediate state which immediately triggered the second step, the gradual transition to the final state. The second step would thus not occur randomly but would instantly follow the first step/transition. Further, it would always take the

same, fixed amount of time. An example of such a process is shown in figure 8.3c. Since this histogram resembles our data we cannot exclude the occurrence of a fixed, gradual step instead of a random one. Nevertheless, we can already say that the fixed step must be relatively short (a crude estimate yields half the bin width, so approximately 40 s for tubulin and 6 s for tubulin&EBs), otherwise we would not get a count in the first bin.

In this context we want to look at another problem, the different number of steps found for the catastrophe process. As already mentioned, Gardner et al [Gardner et al., 2011b] found approximately 2.5 - 3.4 steps until catastrophe, for free MTs grown in the presence of 7 - 14 μM tubulin (without EBs). This is larger than the ~ 1.8 steps we find. To understand the reason for the variation we analysed/repeated the experiments at different conditions (different tubulin batch (data of [Janson et al., 2003]), different conditions, 28° C, 12 μM tubulin and 110 mM KCl (same as [Gardner et al., 2011b])). The gamma distribution suggested 1.8 - 2.5 steps where the highest number of steps was found when using the conditions from [Gardner et al., 2011b] (data not shown). Whether the number of steps is changed by the experimental conditions, shows the inherent nature of the MT or stems from a simple systematic difference (e.g. surface blocking method) will be shown in the future.

8.2.2 The catastrophe process of MTs under force

Both for free MTs and MTs at a barrier we have a problem in accurately determining short events. For free MTs we solved this by fitting truncated distributions. However, at the barrier we would need more statistics to do this and to determine the precise number of steps. Nevertheless, our data clearly shows that the distributions for MTs under force (with tubulin / tubulin&EBs) differ while they look alike for free MTs. Whereas in the presence of force and tubulin we saw at least two steps, in the presence of force and EBs we only identified one. We suggested an explanation for the reduction of steps in the presence of EBs, namely the omission of the first catastrophe-promoting event. As we did not give a physical explanation for the increase of number of steps for MTs grown in only tubulin, let us look at this data in more detail now.

One putative scenario involves missing a short, third step for the free MTs. If this step lasted the same time for free MTs and for MTs at the barrier it could be retrieved at the barrier due to the relative duration compared to the other steps. To examine this we simulated three-step distributions, see fig. 8.4. Two steps were of similar timescales as obtained from our data of free MTs in the absence of EBs (here: $t_{r1}=90$ s and $t_{r2}=210$ s). A third fixed-duration step or a random step was added to the total catastrophe time. We fitted thousand such catastrophe times with gamma distributions and found that only for short third steps does the gamma distribution suggest less than two steps, as we found for our data. It seems that we hence did not miss a third step, unless it is faster than ~ 6 s (fixed)

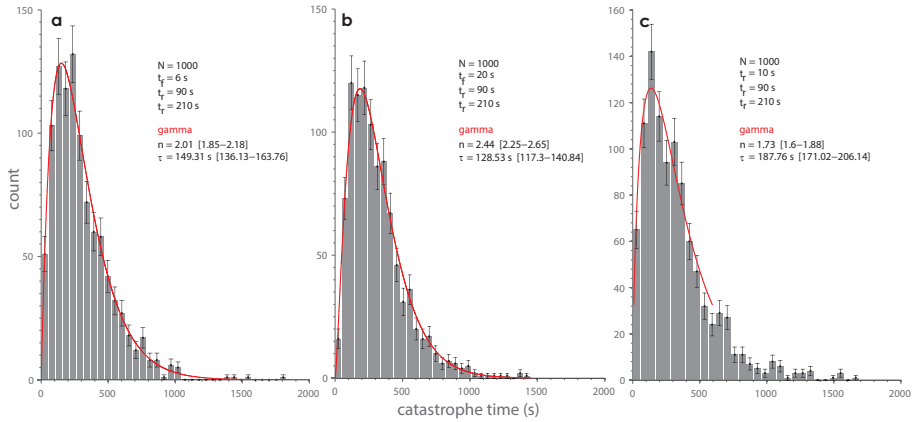


Figure 8.4: Simulated catastrophe time histograms testing the influence of a short step on the fitting parameters. Individual numbers were chosen (representing a fixed-duration step with timescale t_f) or random numbers were generated from an exponential distribution (representing a random step of timescale t_r). **a-b.** Two random numbers and one fixed one or **c.** three random numbers were added up to obtain a catastrophe time, representing the duration of the total reaction. Here we show the histograms of thousand catastrophe times where the bin sizes are determined objectively [Freedman and Diaconis, 1981]. The unbinned data was fitted with a gamma distribution where the fit results are displayed in the figure with the 95% confidence intervals in square brackets. The gamma distribution only suggests less than two steps if the third step is short. For our data, obtained in the absence of EBs, it means that we did not miss a third step, unless it is faster than ~ 6 s (fixed) or ~ 15 s (random).

or ~ 15 s (random). This teaches us that we cannot fully exclude a very short third step. Assuming therefore a three-step distribution for free MTs what would the distribution at the barrier look like? For this we simulated a process with $N=1000$ catastrophe times made up of two random steps and a third random or fixed one which was the shortest step and of ten seconds duration. Yet, no matter which combination we tried for the other two steps we could not reproduce our data at the barrier (data not shown). If the short step was comparably fast (the longer ones ~ 50 s) then the gamma distribution found only 2 to 2.5 steps (though we assumed three). This makes sense as the gamma distribution assumes steps of equal timescales which was not the case here. On the other hand, if two or all steps were comparably fast (all about 10 s long) then the gamma function found 3 to 4 steps. Yet, in this case the total reaction lasted much shorter than we measured for our data. We face comparable difficulties when simulating a distribution with four steps where one of them is of fixed duration, 10 s (data not shown). Conclusively, we do not think that we miss a step in the catastrophe process of free MTs which would show up at the barrier data. To understand the catastrophe process at the barrier more experiments are therefore necessary.

8.2.3 More insights into the catastrophe process

In line with the results of other studies we have found that the MT lifetime distribution does not follow an exponential decay but displays a clear maximum. As such, MTs that are already growing several minutes are more likely to catastrophe than freshly nucleated ones. In the literature this has led to the concept of "MT aging" which has also been observed through the gradual decrease of the EB comet intensity during steady-state growth [Maurer et al., 2012, Mohan et al., 2013]. For MT aging currently two main models exist.

In one of them MT aging not only refers to the time the MT has been growing but also to its accumulation of "defects" [Odde et al., 1995, Gardner et al., 2011b, Mohan et al., 2013]. Several ideas for these defects have been proposed. Kinetic steps could lead to transient states to which local and temporal criteria apply in order to render the MT unstable [Brun et al., 2009]. Contrary, kinetic steps could lead to permanent defects believing the MT to have a "memory" of them. A prominent example for such a catastrophe criterion is formed by the aforementioned GDP-terminated protofilaments with the condition of accumulating several such defects [Gardner et al., 2011b, Gardner et al., 2013]. Recent studies have indeed shown that GDP-tubulin at the MT end has an impact on further growth [Piedra et al., 2016, Kim and Rice, 2019, Cleary and Hancock, 2021]. Furthermore, calculations based on the catastrophe criterion of accumulating three such defect protofilaments well agreed with experimental results and MT lifetime distributions [Bowne-Anderson et al., 2013].

On the other hand, an analytic extension of these calculations and a fit to MT delay times after tubulin washout experiments failed to fit or implied rate constants that contradict experimental data [Duellberg et al., 2016b]. In addition, *in vitro* TIRF experiments with two differently coloured tubulin dimers showed that laser-induced MTs can repair themselves, leading to quite stable rescue-inducing lattice sites [Aumeier et al., 2016]. As we have shown, EBs are highly capable of influencing MT stability by e.g. mal3 inducing a compaction of the lattice [Maurer et al., 2012], XMAP215 binding and removing tubulin dimers from the MT end [Brouhard et al., 2008] or CLASP stabilizing incomplete lattices [Aher et al., 2018, Mahserejian et al., 2022]. In *in vivo* environments where these microtubule-associated proteins, among others, are present it is hard to imagine that a MT could not "repair" a GDP-capped protofilament and render it capable of further growth. This holds especially in the light that also cells are found to repair damaged MT lattices [Aumeier et al., 2016] and that further experiments with TIRF microscopy and Monte Carlo modelling have shown that the MT lattice can rejuvenate itself [Schaedel et al., 2019].

Also in this thesis we have analyzed our data based on the assumption of the multistep defect model. We have found no cue as to decide whether these steps are transient or permanent and what the molecular nature of these steps could be. Confirming this problem, todate experiments are missing which give a deeper molecular insight into the multistep catastrophe model. It does not make it easier that also the mechanism of growth leaves many questions open and the postulated

conditions for MT catastrophe cannot be probed directly.

Next to the defect-accumulation model for explaining the peaked MT lifetime distributions is the "taper-cap density" model. Electron microscopy images had shown rugged extensions at the microtubule ends indicating that not all protofilaments have the same length [Mandelkow et al., 1991, Chretien et al., 1995]. These so-called tapered tips are found increasingly pointed over the MT lifetime causing progressive instability [Coombes et al., 2013]. Duellberg et al. assumed in their MT washout experiments [Duellberg et al., 2016a] that MT destabilization occurs by lattice maturation (through random hydrolysis and accompanying conformational changes) and slow depolymerization (by the ongoing dissociation of tubulin subunits after free tubulin washout) until a critical density is reached. Catastrophe occurs when this critical density is reached at the very end of the blunt MT. Taking into account a tapered MT end changes the density of binding sites in the MT: the more tapered the MT becomes, the more the binding sites are distributed and the lower the density of binding sites becomes. Thus, an "older" MT with already a lower density of binding sites at steady state reaches the critical density threshold faster than a MT which "starts" with a higher density at washout [Duellberg et al., 2016b].

Next to these two lines of reasoning several MT growth and catastrophe models exist explaining experimental data without these two MT aging models. Assuming different hydrolysis mechanisms (vectorial, random or coupled or often a combination of these) often in conjunction with different tubulin dimer association rates depending on longitudinal and lateral protofilament interactions in the 3D MT lattice results in a multitude of models fitting data with more or less varying accuracy [Margolin et al., 2012, VanBuren et al., 2002, Gardner et al., 2011b, Mickolajczyk et al., 2019, Bowne-Anderson et al., 2013, Coombes et al., 2013]. Also our model of fluctuating tip growth, random hydrolysis in a 1D MT lattice, together with a critical density as a catastrophe criterion, can explain a range of experimental data including washout experiments, see chapter 7. Here, the progressive increase of the catastrophe probability over time is reached by introducing a time-dependent, increasing tip (growth) noise, gradually raising the probability for an unstable MT tip.

At the moment, it is not clear which of the above mentioned models is really describing MT dynamics and further investigations are crucial. At the moment the dilemma between low resolution and dynamic imaging methods (light microscopy) versus high resolution but static ones (electron microscopy) poses a limit. Only with new ideas will our horizon be broadened.

8.3 High resolution on MT growth under force

In chapter 6 we examined the influence of force on the MT growth speed using optical tweezers. Though free MTs grow faster in the presence of mal3, tea2 and

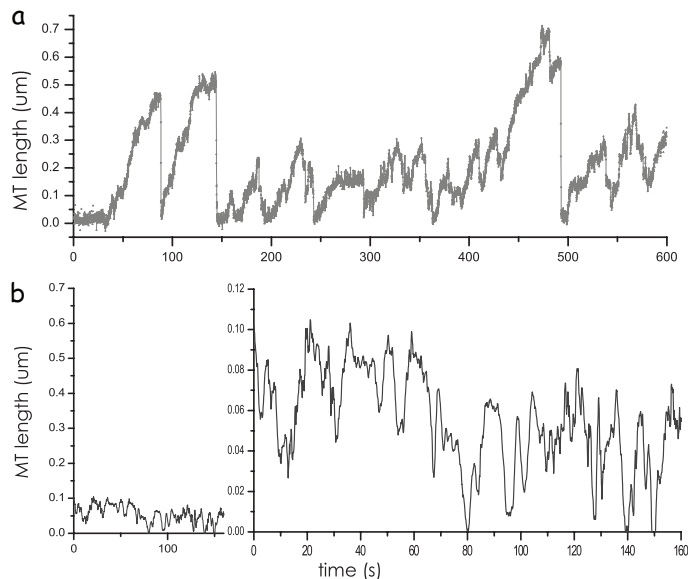


Figure 8.5: MT growth traces obtained with optical tweezers. MTs are grown from a bead-axoneme construct against a rigid barrier. MT growth results in displacement of the trapped bead from which we can deduce the MT length. Here, MT length is plotted over time in the presence of tubulin with mal3, tea2 and tip1. **a.** This example shows twice the nucleation of a single MT after which only MT bundles are nucleated. **b.** We occasionally saw repeated "saw-tooth" growth events where MTs do not grow long and have frequent catastrophes and (re-)nucleation events. In the presence of tubulin alone we never observed this type of dynamics. The *right* figure shows the same data as on the *left*, zoomed in.

tip1 than in their absence, we could not observe this under force. We explained this result with our aforementioned observation about the loss of the mal3 comet under force. Since mal3 may unbind from the MT already at small forces we think that the effect of EBs on MT growth speed is only visible for forces $F < 0.5$ pN. Thereafter the MT tip is not bound by EBs even if they are present in the buffer and the growth speed is (almost) the same as for MTs grown in pure tubulin.

8.3.1 Growth at small forces

The interesting questions thus are: do EBs affect MT growth only at small forces, $F < 0.5$ pN? If yes, of what nature is the force-growth speed relationship in this case? For this we would need to measure at forces smaller than 0.5 pN. This could be tried with the use of force-feedback though it is experimentally hard. Another, easier, method is to analyse our data carefully in the "soft-regime". At the barrier MT growth does initially not result in displacement of the attached bead from the trap centre. The reason is the elastic unspecific attachment between bead

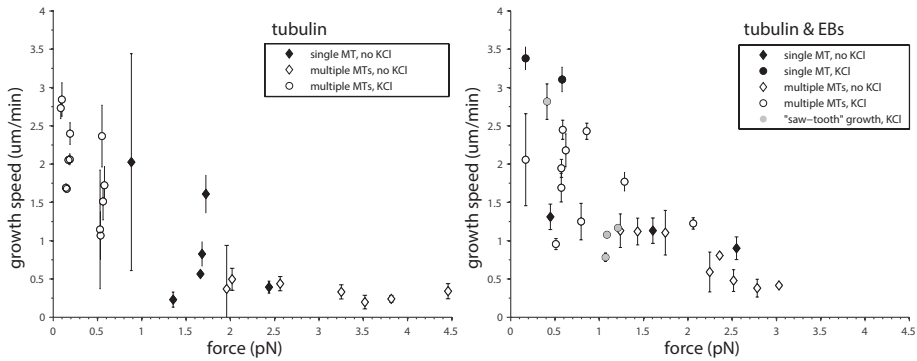


Figure 8.6: Force - growth speed relationship of "saw-tooth" growth. Average growth speed and average force for MTs grown in different conditions (left in pure tubulin, right in presence of tubulin and mal3, tea2 and tip1; open symbols: multiple MTs, black symbols: single MTs, grey symbols: "saw-tooth" growth; diamonds: no added salt, circles: 50 mM KCl added). Considering force generation and growth speed saw-tooth growth is comparable to "normal" MT growth events. (This figure is adapted from fig. 6.5.)

and axoneme. Only after this attachment is stretched out, after about 50 nm, is MT length proportional to the bead displacement (see page 68ff.). Since here it is easier to deduce force and MT length we measured only in this regime. With careful analysis we can also analyse the MT growth trajectories in the presence of EBs at the initial build-up of force.

Another complication of the experiment is the nucleation of multiple MTs. Since they can share the force load and it is hard to determine the exact number of MTs it is hard to reliably reproduce and analyse such data. As the nucleation of several MTs happens far more often in the presence of EBs than in their absence it makes the comparison between the two datasets difficult. This also obstructs the effect of EBs on the MT growth speed. Therefore a better control of MT nucleation, e.g. by altering the tubulin concentration or the temperature would improve our insight into effect of EBs.

8.3.2 "Saw-tooth" growth dynamics

In the presence of EBs we occasionally saw repeated catastrophe and (re-) nucleation cycles during which MTs stayed relatively short ($< 0.3 \mu\text{m}$), see figure 8.5. Growth occurred in short bursts and the MT did not shrink back to the axoneme but experienced many "rescue" events. We rarely observed this "saw-tooth" growth pattern in the presence of pure tubulin and therefore find mal3, tea2 and/or tip1 responsible. Comparing figure 8.5a and b (left), we can be sure that saw-tooth growth is not noise. On the other hand, it is also not representing an artifact since after some time of saw-tooth growth the MT usually nucleated a "normal" growth event. We observed that the nucleation of one/the first MT under force in the presence of

EBs is difficult and therefore fewer MTs are nucleated. This is opposite to the case of free MTs where EBs increase the nucleation frequency of MTs. To increase the occurrence of nucleation we placed the axoneme tip approximately 50 nm in front of the barrier such that only after having grown to a length of 50 nm the MT would experience a force. Conclusively, we can say that MTs with EBs have difficulties in nucleation under force and therefore display this saw-tooth dynamics. We surmise that it represents tubulin structures not yet closed into the MT tube. The results of a first analysis analogously to described in chapter 6 are presented in figure 8.6. Nonetheless, it might be useful to analyse their dynamics in detail which might give us useful information about the structural effects of EBs of MTs under force.

Methods

Here we will only remark on the differences to the more extended explanation of methods in the respective chapters.

To measure the correlated dynamics of EBs we used both labelled mal3-mCherry and tip1-GFP and unlabelled tea2. The microtubule was not fluorescent, however, the seed contained tubulin-HiLyte635. We measured at time-lapse intervals of 0.8 s.

For the simulation of a reversible-step distribution we generated $N=1000$ catastrophe times, each comprised of two forward, random steps of duration τ_1 and τ_2 . We then added another random backward and forward step (of duration τ_{-1} and τ_1 , respectively) to $\tau_1/\tau_{-1} N$ catastrophe times. This represents the reversibility of the first reaction occurring once. Since a backward reaction could possibly occur more often, we added a second forward and backward step to $(\tau_1/\tau_{-1})^2 N$ catastrophe times. The probability for a further backward step is so small that we omitted it.

Acknowledgements

I want to thank Olga Sytina for help in preparing the optical tweezer experiments, for carrying them out and for doing most of the optical tweezers data analysis. Further, I want to thank Katja Zieske for performing the correlated intensity experiments containing mal3-mCherry and tip1-GFP. I am grateful that Magdalena Preciado-Lopez performed the experiments of free MTs grown in 12 μM tubulin at 28° C.

We thank Chris Rétif, Gijs Vollenbroek and Hans Zeijlemaker for their advice on micro-fabrication, E. Laura Munteanu, and Julien Husson for help with the optical trap assay and Roland Dries for developing the bead-tracking software. We appreciate the generous axoneme present from Matt Footer. We are grateful for the help of Peter Bieling and Thomas Surrey with the protein purification of mal3-alexa488, tea2 and tip1 and for generously providing us a mal3-GFP vector.

The work presented in this chapter was carried out as part of the EU Program AMOCROSS, as part of a "VICI" grant provided by the "Nederlandse Organisatie voor Wetenschappelijk Onderzoek (NWO)" and as part of the research program of the "Stichting voor Fundamenteel Onderzoek der Materie (FOM)", which is financially supported by the "Nederlandse Organisatie voor Wetenschappelijk Onderzoek (NWO)".

References

- [web, a] <http://celldynamics.org/celldynamics/research/cytokinesis/>.
- [web, b] <http://www.london-research-institute.org.uk/research/takashi-toda/projects>.
- [web, c] <http://www.proteinatlas.org/dictionary/cell/cytoskeleton+++microtubules>.
- [Adames and Cooper, 2000] Adames, N. R. and Cooper, J. A. (2000). Microtubule interactions with the cell cortex causing nuclear movements in *saccharomyces cerevisiae*. *J Cell Biol*, 149(4):863–874.
- [Aher et al., 2018] Aher, A., Kok, M., Sharma, A., Rai, A., Olieric, N., Rodriguez-Garcia, R., Katrukha, E., Weinert, T., Olieric, V., Kapitein, L., Steinmetz, M., Dogterom, M., and Akhmanova, A. (2018). CLASP suppresses microtubule catastrophes through a single TOG domain. *Dev Cell*, 46:40–58.
- [Akhmanova et al., 2001] Akhmanova, A., Hoogenraad, C. C., Drabek, K., Stepanova, T., Dortland, B., Verkerk, T., Vermeulen, W., Burgering, B. M., De Zeeuw, C. I., Grosveld, F., and Galjart, N. (2001). Clasps are clip-115 and-170 associating proteins involved in the regional regulation of microtubule dynamics in motile fibroblasts. *Cell*, 104(6):923–935–.
- [Akhmanova and Steinmetz, 2008] Akhmanova, A. and Steinmetz, M. O. (2008). Tracking the ends: a dynamic protein network controls the fate of microtubule tips. *Nature Reviews Molecular Cell Biology*, 9(4):309–322–.
- [Akhmanova and Steinmetz, 2015] Akhmanova, A. and Steinmetz, M. O. (2015). Control of microtubule organization and dynamics: two ends in the limelight. *Nature reviews. Molecular cell biology*, 16:711–726.
- [Alberts et al., 2002] Alberts, B., Johnson, A., Lewis, J., Raff, M., Roberts, K., and Walter, P. (2002). *Molecular Biology Of The Cell*, volume 4. Garland Publishing, New York.
- [Allen and Borisy, 1974] Allen, C. and Borisy, G. G. (1974). Structural polarity and directional growth of microtubules of *chlamydomonas flagella*. *Journal of Molecular Biology*, 90(2):381–402.
- [Alushin et al., 2014] Alushin, G., Lander, G., Kellogg, E., Zhang, R., Baker, D., and Nogales, E. (2014). High-resolution microtubule structures reveal the structural transitions in α -tubulin upon gtp hydrolysis. *Cell*, 157:1117–1129.
- [Amos and Klug, 1974] Amos, L. A. and Klug, A. (1974). Arrangement of subunits in flagellar microtubules. *Journal of Cell Science*, 14(3):523–549.
- [Antal et al., 2007] Antal, T., Krapivsky, P., Redner, S., Mailman, M., and Chakraborty, B. (2007). Dynamics of an idealized model of microtubule growth and catastrophe. *Phys Rev E Stat Nonlin Soft Matter Phys*, 76:41907.
- [Arnal et al., 2004] Arnal, I., Heichette, C., Diamantopoulos, G. S., and Chretien, D. (2004). Clip-170/tubulin-curved oligomers coassemble at microtubule ends and promote rescues. *Current Biology*, 14(23):2086–2095–.
- [Ashkin, 1970] Ashkin, A. (1970). Acceleration and trapping of particles by radiation pressure. *Physical Review Letters*, 24(4):156–159–.
- [Atkins, 1979] Atkins, P. W. (1979). *Physical Chemistry*. Oxford University Press.
- [Aumeier et al., 2016] Aumeier, C., Schaedel, L., Gaillard, J., John, K., Blanchoin, L., and Théry, M. (2016). Self-repair promotes microtubule rescue. *Nature cell biology*, 18:1054–1064.
- [Barnes et al., 2001] Barnes, R. S. K., Calow, P., Olive, P., Golding, D., and Spicer, J. (2001). *Invertebrates with Legs: the Arthropods and Similar Groups. The Invertebrates: A Synthesis.*. Blackwell Publishing.
- [Barton and Goldstein, 1996] Barton, N. R. and Goldstein, L. S. (1996). Going mobile: microtubule motors and chromosome segregation. *Proceedings of the National Academy of Sciences*, 93(5):1735–1742.
- [Bayley et al., 1989] Bayley, P., Schilstra, M., and Martin, S. (1989). A lateral cap model of microtubule dynamic instability. *FEBS Lett*, 259:181–184.

-
- [Beinhauer et al., 1997] Beinhauer, J. D., Hagan, I. M., Hegemann, J. H., and Fleig, U. (1997). Mal3, the fission yeast homologue of the human apc-interacting protein eb-1 is required for microtubule integrity and the maintenance of cell form. *J Cell Biol*, 139(3):717–728.
- [Bieling et al., 2008] Bieling, P., Kandels-Lewis, S., Telley, I. A., van Dijk, J., Janke, C., and Surrey, T. (2008). Clip-170 tracks growing microtubule ends by dynamically recognizing composite eb1/tubulin-binding sites. *Journal of Cell Biology*, 183(7):1223–1233–.
- [Bieling et al., 2007] Bieling, P., Laan, L., Schek, H., Munteanu, E. L., Sandblad, L., Dogterom, M., Brunner, D., and Surrey, T. (2007). Reconstitution of a microtubule plus-end tracking system in vitro. *Nature*, 450(7172):1100–1105.
- [Bollinger and Stevens, 2019] Bollinger, J. and Stevens, M. (2019). Diverse balances of tubulin interactions and shape change drive and interrupt microtubule depolymerization. *Soft Matter*, 15:8137–8146.
- [Bouchet et al., 2016] Bouchet, B., Noordstra, I., Van Amersfoort, M., Katrukha, E., Ammon, Y., Ter Hoeve, N., Hodgson, L., Dogterom, M., Derksen, P., and Akhmanova, A. (2016). Mesenchymal cell invasion requires cooperative regulation of persistent microtubule growth by SLAIN2 and CLASP1. *Dev Cell*, 39:708–723.
- [Bowne-Anderson et al., 2015] Bowne-Anderson, H., Hibbel, A., and Howard, J. (2015). Regulation of microtubule growth and catastrophe: Unifying theory and experiment. *Trends in cell biology*, 25:769–779.
- [Bowne-Anderson et al., 2013] Bowne-Anderson, H., Zanic, M., Kauer, M., and Howard, J. (2013). Microtubule dynamic instability: a new model with coupled gtp hydrolysis and multistep catastrophe. *BioEssays : news and reviews in molecular, cellular and developmental biology*, 35:452–461.
- [Brangwynne et al., 2006] Brangwynne, C., Mackintosh, F., Kumar, S., Geisse, N., Talbot, J., Mahadevan, L., Parker, K., Ingber, D., and Weitz, D. (2006). Microtubules can bear enhanced compressive loads in living cells because of lateral reinforcement. *J Cell Biol*, 173:733–741.
- [Brangwynne et al., 2007] Brangwynne, C., Mackintosh, F., Weitz ; G, D., and Rice, L. (2007). Force fluctuations and polymerization dynamics of intracellular microtubules. *Proc Natl Acad Sci U S A*, 104:451–463.
- [Brouhard and Rice, 2018] Brouhard, G. and Rice, L. (2018). Microtubule dynamics: an interplay of biochemistry and mechanics. *Nat Rev Mol Cell Biol*, 19:451–463.
- [Brouhard et al., 2008] Brouhard, G. J., Stear, J. H., Noetzel, T. L., Al-Bassam, J., Kinoshita, K., Harrison, S. C., Howard, J., and Hyman, A. A. (2008). Xmap215 is a processive microtubule polymerase. *Cell*, 132(1):79–88–.
- [Browning et al., 2003] Browning, H., Hackney, D. D., and Nurse, P. (2003). Targeted movement of cell end factors in fission yeast. *Nature Cell Biology*, 5(9):812–818–.
- [Browning et al., 2000] Browning, H., Hayles, J., Mata, J., Aveline, L., Nurse, P., and McIntosh, J. R. (2000). Tea2p is a kinesin-like protein required to generate polarized growth in fission yeast. *Journal of Cell Biology*, 151(1):15–27–.
- [Brun et al., 2009] Brun, L., Rupp, B., Ward, J. J., and N?d?lec, F. (2009). A theory of microtubule catastrophes and their regulation. *Proceedings of the National Academy of Sciences*, 106(50):21173–21178.
- [Brunner and Nurse, 2000a] Brunner, D. and Nurse, P. (2000a). Clip170-like tip1p spatially organizes microtubular dynamics in fission yeast. *Cell*, 102(5):695–704–.
- [Brunner and Nurse, 2000b] Brunner, D. and Nurse, P. (2000b). New concepts in fission yeast morphogenesis. *Philosophical Transactions of the Royal Society of London Series B-Biological Sciences*, 355(1399):873–877–.
- [Burakov et al., 2002] Burakov, A. V., Nadezhdina, E. S., and Rodionov, V. I. (2002). The nature of the centering force. *Molecular Biology of the Cell*, 13:199A–199A–.
- [Busch and Brunner, 2004] Busch, K. E. and Brunner, D. (2004). The microtubule plus end-tracking proteins mal3p and tip1p cooperate for cell-end targeting of interphase microtubules. *Current Biology*, 14(7):548–559–.

- [Busch et al., 2004] Busch, K. E., Hayles, J., Nurse, P., and Brunner, D. (2004). Tea2p kinesin is involved in spatial microtubule organization by transporting tip1p on microtubules. *Developmental Cell*, 6(6):831–843–.
- [Caplow et al., 1994] Caplow, M., Ruhlen, R. L., and Shanks, J. (1994). The free energy for hydrolysis of a microtubule-bound nucleotide triphosphate is near zero: all of the free energy for hydrolysis is stored in the microtubule lattice. *J. Cell Biol.*, 127(3):779–788.
- [Caplow and Shanks, 1996] Caplow, M. and Shanks, J. (1996). Evidence that a single monolayer tubulin-gtp cap is both necessary and sufficient to stabilize microtubules. *Mol Biol Cell*, 7(4):663–675.
- [Carlier and Pantaloni, 1982] Carlier, M. and Pantaloni, D. (1982). Assembly of microtubule protein: role of guanosine di- and triphosphate nucleotides. *Biochemistry*, 21:1215–1224.
- [Carlier et al., 1989] Carlier, M. F., Didry, D., Simon, C., and Pantaloni, D. (1989). Mechanism of gtp hydrolysis in tubulin polymerization: characterization of the kinetic intermediate microtubule-gdp-pi using phosphate analogs. *Biochemistry*, 28(4):1783–1791.
- [Carlier et al., 1984] Carlier, M.-F., Hill, T. L., and Chen, Y.-D. (1984). Interference of GTP hydrolysis in the mechanism of microtubule assembly: an experimental study. *Proc. Natl. Acad. Sci.*, 81(3):771–775.
- [Carlier and Pantaloni, 1981] Carlier, M. F. and Pantaloni, D. (1981). Kinetic analysis of guanosine 5'-triphosphate hydrolysis associated with tubulin polymerization. *Biochemistry*, 20:1918–1924.
- [Charlebois et al., 2010] Charlebois, B. D., Schek III, H. T., and Hunt, A. J. (2010). Chapter 12 - nanometer-resolution microtubule polymerization assays using optical tweezers and microfabricated barriers. In Wilson, L. and Correia, J. J., editors, *Microtubules, in vitro*, volume Volume 95, pages 207–219. Academic Press.
- [Chen and Hill, 1985] Chen, Y. and Hill, T. (1985). Monte Carlo study of the GTP cap in a five-start helix model of a microtubule. *Proc Natl Acad Sci U S A*, 82:1131–1135.
- [Chretien et al., 1995] Chretien, D., Fuller, S. D., and Karsenti, E. (1995). Structure of growing microtubule ends - 2-dimensional sheets close into tubes at variable rates. *Journal of Cell Biology*, 129(5):1311–1328–.
- [Chretien et al., 1992] Chretien, D., Metoz, F., Verde, F., Karsenti, E., and Wade, R. H. (1992). Lattice-defects in microtubules - protofilament numbers vary within individual microtubules. *Journal of Cell Biology*, 117(5):1031–1040–.
- [Chretien and Wade, 1991] Chretien, D. and Wade, R. H. (1991). New data on the microtubule surface lattice. *Biology of the Cell*, 71(1-2):161–174–.
- [Cleary and Hancock, 2021] Cleary, J. M. and Hancock, W. O. (2021). Molecular mechanisms underlying microtubule growth dynamics. *Current Biology*, 31(10):R560–R573.
- [Coletti et al., 2007] Coletti, C., Jaroszeski, M., Pallaoro, A., Hoff, A., Iannotta, S., and Saddow, S. (2007). Biocompatibility and wettability of crystalline SiC and Si surfaces. *Conf Proc IEEE Eng Med Biol Soc*, pages 5850–5853.
- [Colin et al., 2018] Colin, A., Singaravelu, P., They, M., Blanchoin, L., and Gueroui, Z. (2018). Actin-network architecture regulates microtubule dynamics. *Curr Biol*.
- [Coombes et al., 2013] Coombes, C., Yamamoto, A., Kenzie, M., Odde, D., and Gardner, M. (2013). Evolving tip structures can explain age-dependent microtubule catastrophe. *Curr Biol*, 23:1342–1348.
- [Das et al., 2014] Das, D., Das, D., and Padinhateeri, R. (2014). Force-induced dynamical properties of multiple cytoskeletal filaments are distinct from that of single filaments. *PLoS One*, 9:e114014.
- [Debs et al., 2020] Debs, G. E., Cha, M., Liu, X., Huehn, A. R., and Sindelar, C. V. (2020). Dynamic and asymmetric fluctuations in the microtubule wall captured by high-resolution cryoelectron microscopy. *Proceedings of the National Academy of Sciences of the United States of America*, 117:16976–16984.
- [Desai and Mitchison, 1997] Desai, A. and Mitchison, T. J. (1997). Microtubule polymerization dynamics. *Annu Rev Cell Dev Biol*, 13:83–117–.

-
- [Dhar et al., 2009] Dhar, S., Seitz, O., Halls, M., Choi, S., Chabal, Y., and Feldman, L. (2009). Chemical properties of oxidized silicon carbide surfaces upon etching in hydrofluoric acid. *J Am Chem Soc*, 131:16808–16813.
- [Dimitrov et al., 2008] Dimitrov, A., Quesnoit, M., Moutel, S., Cantaloube, I., Pous, C., and Perez, F. (2008). Detection of gtp-tubulin conformation in vivo reveals a role for gtp remnants in microtubule rescues. *Science*, 322(5906):1353–1356–.
- [Dixit et al., 2009] Dixit, R., Barnett, B., Lazarus, J. E., Tokito, M., Goldman, Y. E., and Holzbaur, E. L. F. (2009). Microtubule plus-end tracking by clip-170 requires eb1. *Proceedings of the National Academy of Sciences of the United States of America*, 106(2):492–497–.
- [Dogterom and Leibler, 1993] Dogterom and Leibler (1993). Physical aspects of the growth and regulation of microtubule structures. *Phys Rev Lett*, 70(9):1347–1350.
- [Dogterom et al., 1996] Dogterom, M., Felix, M. A., Guet, C. C., and Leibler, S. (1996). Influence of m-phase chromatin on the anisotropy of microtubule asters. *J Cell Biol*, 133(1):125–40–.
- [Dogterom et al., 2002] Dogterom, M., Janson, M., Faivre-Moskalenko, C., van der Horst, A., Kerssemakers, J., Tanase, C., and Mulder, B. (2002). Force generation by polymerizing microtubules. *Applied Physics A: Materials Science & Processing*, 75:331–336. 10.1007/s003390201342.
- [Dogterom et al., 2005] Dogterom, M., Kerssemakers, J. W., Romet-Lemonne, G., and Janson, M. E. (2005). Force generation by dynamic microtubules. *Curr Opin Cell Biol*, 17(1):67–74–.
- [Dogterom and Koenderink, 2019] Dogterom, M. and Koenderink, G. H. (2019). Actin-microtubule crosstalk in cell biology. *Nature reviews. Molecular cell biology*, 20:38–54.
- [Dogterom and Yurke, 1997] Dogterom, M. and Yurke, B. (1997). Measurement of the force-velocity relation for growing microtubules. *Science*, 278(5339):856–860–.
- [Drechsel and Kirschner, 1994] Drechsel, D. N. and Kirschner, M. W. (1994). The minimum gtp cap required to stabilize microtubules. *Current Biology*, 4(12):1053–1061–.
- [Drummond and Cross, 2000] Drummond, D. R. and Cross, R. A. (2000). Dynamics of interphase microtubules in *schizosaccharomyces pombe*. *Curr Biol*, 10(13):766–775.
- [Duellberg et al., 2016a] Duellberg, C., Cade, N., Holmes, D., and Surrey, T. (2016a). The size of the EB cap determines instantaneous microtubule stability. *Elife*, 5.
- [Duellberg et al., 2016b] Duellberg, C., Cade, N., and Surrey, T. (2016b). Microtubule aging probed by microfluidics-assisted tubulin washout. *Mol Biol Cell*, 27:3563–3573.
- [Felgner et al., 1997] Felgner, H., Frank, R., Biernat, J., Mandelkow, E.-M., Mandelkow, E., Ludin, B., Matus, A., and Schliwa, M. (1997). Domains of neuronal microtubule-associated proteins and flexural rigidity of microtubules. *J. Cell Biol*, 138(5):1067–1075.
- [Felgner et al., 1996] Felgner, H., Frank, R., and Schliwa, M. (1996). Flexural rigidity of microtubules measured with the use of optical tweezers. *J Cell Sci*, 109(2):509–516.
- [Finer et al., 1994] Finer, J. T., Simmons, R. M., and Spudich, J. A. (1994). Single myosin molecule mechanics: piconewton forces and nanometre steps. *Nature*, 368(6467):113–119.
- [Floyd et al., 2010] Floyd, D. L., Harrison, S. C., and van Oijen, A. M. (2010). Analysis of kinetic intermediates in single-particle dwell-time distributions. *Biophysical Journal*, 99(2):360–366.
- [Flyvbjerg et al., 1994] Flyvbjerg, Holy, and Leibler (1994). Stochastic dynamics of microtubules: A model for caps and catastrophes. *Phys Rev Lett*, 73(17):2372–2375.
- [Flyvbjerg et al., 1996] Flyvbjerg, H., Holy, T., and Leibler, S. (1996). Microtubule dynamics: Caps, catastrophes, and coupled hydrolysis. *Phys Rev E Stat Phys Plasmas Fluids Relat Interdiscip Topics*, 54:5538–5560.
- [Foethke et al., 2009] Foethke, D., Makushok, T., Brunner, D., and Nedelec, F. (2009). Force and length-dependent catastrophe activities explain interphase microtubule organization in fission yeast. *Molecular systems biology*, pages —.
- [Freedman and Diaconis, 1981] Freedman, D. and Diaconis, P. (1981). On the histogram as a density estimator: L2 theory. *Probability Theory and Related Fields*, 57:453–476. 10.1007/BF01025868.

- [Fygenon et al., 1994] Fygenon, D. K., Braun, E., and Libchaber, A. (1994). Phase-diagram of microtubules. *Physical Review E*, 50(2):1579–1588–.
- [Fygenon et al., 1997] Fygenon, D. K., Marko, J. F., and Libchaber, A. (1997). Mechanics of microtubule-based membrane extension. *Phys. Rev. Lett.*, 79(22):4497–4500–.
- [Gadde and Heald, 2004] Gadde, S. and Heald, R. (2004). Mechanisms and molecules of the mitotic spindle. *Current Biology*, 14(18):R797–R805–.
- [Gardner et al., 2011a] Gardner, M. K., Charlebois, B. D., Jánosi, I. M., Howard, J., Hunt, A. J., and Odde, D. J. (2011a). Rapid microtubule self-assembly kinetics. *Cell*, 146(4):582–592.
- [Gardner et al., 2011b] Gardner, M. K., Zanic, M., Gell, C., Bormuth, V., and Howard, J. (2011b). Depolymerizing kinesins kip3 and mcaK shape cellular microtubule architecture by differential control of catastrophe. *Cell*, 147(5):1092–1103.
- [Gardner et al., 2013] Gardner, M. K., Zanic, M., and Howard, J. (2013). Microtubule catastrophe and rescue. *Current opinion in cell biology*, 25:14–22.
- [Gildersleeve et al., 1992] Gildersleeve, R. F., Cross, A. R., Cullen, K. E., Fagen, A. P., and Williams, R. C. (1992). Microtubules grow and shorten at intrinsically variable rates. *Journal of Biological Chemistry*, 267(12):7995–8006.
- [Gittes et al., 1996] Gittes, F., Meyhofer, E., Baek, S., and Howard, J. (1996). Directional loading of the kinesin motor molecule as it buckles a microtubule. *Biophys J*, 70(1):418–429.
- [Gittes and Schmidt, 1998] Gittes, F. and Schmidt, C. F. (1998). Signals and noise in micromechanical measurements. *Methods in Cell Biology*, Vol 55, 55:129–156–.
- [Gouveia et al., 2010] Gouveia, S. M., Leslie, K., Kapitein, L. C., Buey, R. M., Grigoriev, I., Wagenbach, M., Smal, I., Meijering, E., Hoogenraad, C. C., Wordeman, L., Steinmetz, M. O., and Akhmanova, A. (2010). In vitro reconstitution of the functional interplay between mcaK and eb3 at microtubule plus ends. *Curr Biol*.
- [Gregoretto et al., 2006] Gregoretto, I. V., Margolin, G., Alber, M. S., and Goodson, H. V. (2006). Insights into cytoskeletal behavior from computational modeling of dynamic microtubules in a cell-like environment. *J Cell Sci*, 119(Pt 22):4781–4788.
- [Grishchuk et al., 2005] Grishchuk, E. L., Molodtsov, M. I., Ataullakhanov, F. I., and McIntosh, J. R. (2005). Force production by disassembling microtubules. *Nature*, 438(7066):384–388–.
- [Guizar-Sicairos et al., 2008] Guizar-Sicairos, M., Thurman, S., and Fienup, J. (2008). Efficient subpixel image registration algorithms. *Opt Lett*, 33:156–158.
- [Gurel et al., 2014] Gurel, P., Hatch, A., and Higgs, H. (2014). Connecting the cytoskeleton to the endoplasmic reticulum and Golgi. *Curr Biol*, 24:R660–R672.
- [Hill, 1987] Hill, T. (1987). *Linear aggregation theory in cell biology*. Springer-Verlag, New York, Berlin, Heidelberg.
- [Hill and Kirschner, 1982] Hill, T. and Kirschner, M. (1982). Bioenergetics and kinetics of microtubule and actin filament assembly and disassembly. *Int. Rev. Cytol.*, 78:1–125–.
- [Hill, 1984] Hill, T. L. (1984). Introductory analysis of the gtp-cap phase-change kinetics at the end of a microtubule. *Proceedings of the National Academy of Sciences*, 81(21):6728–6732.
- [Holy et al., 1997] Holy, T. E., Dogterom, M., Yurke, B., and Leibler, S. (1997). Assembly and positioning of microtubule asters in microfabricated chambers. *Proceedings of the National Academy of Sciences of the United States of America*, 94(12):6228–6231–.
- [Holy and Leibler, 1994] Holy, T. E. and Leibler, S. (1994). Dynamic instability of microtubules as an efficient way to search in space. *Proceedings of the National Academy of Sciences*, 91(12):5682–5685.
- [Honnappa et al., 2009] Honnappa, S., Gouveia, S. M., Weisbrich, A., Damberger, F. F., Bhavesh, N. S., Jawhari, H., Grigoriev, I., van Rijssel, F. J., Buey, R. M., Lawera, A., Jelesarov, I., Winkler, F. K., Wuthrich, K., Akhmanova, A., and Steinmetz, M. O. (2009). An eb1-binding motif acts as a microtubule tip localization signal. *Cell*, 138(2):366–76–.
- [Hotani and Miyamoto, 1990] Hotani, H. and Miyamoto, H. (1990). Dynamic features of microtubules as visualized by dark-field microscopy. *Advances in Biophysics*, 26(0):135–156.

-
- [Howard, 2001] Howard, J. (2001). *Mechanics of Motor Proteins and the Cytoskeleton*, volume 1. Sinauer Associates, Sunderland, USA.
- [Howard and Hyman, 2007] Howard, J. and Hyman, A. A. (2007). Microtubule polymerases and depolymerases. *Curr Opin Cell Biol*, 19(1):31–35–.
- [Hyman et al., 1992] Hyman, A. A., Salser, S., Drechsel, D. N., Unwin, N., and Mitchison, T. J. (1992). Role of gtp hydrolysis in microtubule dynamics - information from a slowly hydrolyzable analog, gmpcpp. *Mol Biol Cell*, 3(10):1155–1167–.
- [Inoue and Salmon, 1995] Inoue, S. and Salmon, E. D. (1995). Force generation by microtubule assembly disassembly in mitosis and related movements. *Mol Biol Cell*, 6(12):1619–1640–.
- [Janosi et al., 2002] Janosi, I. M., Chretien, D., and Flyvbjerg, H. (2002). Structural microtubule cap: Stability, catastrophe, rescue, and third state. *Biophysical Journal*, 83(3):1317–1330–.
- [Janson, 2002] Janson, M. E. (2002). *Force Generation by Growing Microtubules*. PhD thesis, Leiden University.
- [Janson and Dogterom, 2004] Janson, M. E. and Dogterom, M. (2004). A bending mode analysis for growing microtubules: Evidence for a velocity-dependent rigidity. *Biophysical Journal*, 87(4):2723–2736–.
- [Janson et al., 2003] Janson, M. E., Dood, M. E. d., and Dogterom, M. (2003). Dynamic instability of microtubules is regulated by force. *The Journal of Cell Biology*, 161(6):1029–1034–.
- [Johnson et al., 1994] Johnson, N., Kotz, S., and Balakrishnan, N. (1994). *Continuous Univariate Distributions*, volume 1. Wiley.
- [Kalisch et al., 2011] Kalisch, S.-M., Laan, L., and Dogterom, M. (2011). Microtubule dynamics : methods and protocols. In *Springer Protocols. Methods in Molecular Biology*, volume 777, pages Chap. 11: 147–165. Humana; Springer, New York.
- [Karr and Purich, 1978] Karr, T. and Purich, D. (1978). Examination of tubulin-nucleotide interactions by protein fluorescence quenching measurements. *Biochem Biophys Res Commun*, 84:957–961.
- [Katsuki et al., 2009] Katsuki, M., Drummond, D. R., Osei, M., and Cross, R. A. (2009). Mal3 masks catastrophe events in schizosaccharomyces pombe microtubules by inhibiting shrinkage and promoting rescue. *J Biol Chem*, 284(43):29246–29250.
- [Kellogg et al., 1994] Kellogg, D. R., Moritz, M., and Alberts, B. M. (1994). The centrosome and cellular organization. *Annu. Rev. Biochem.*, 63(1):639–674.
- [Kerssemakers et al., 2003] Kerssemakers, J. W. J., Janson, M. E., Van der Horst, A., and Dogterom, M. (2003). Optical trap setup for measuring microtubule pushing forces. *Applied Physics Letters*, 83:4441–.
- [Kerssemakers et al., 2006] Kerssemakers, J. W. J., Munteanu, E. L., Laan, L., Noetzel, T. L., Janson, M. E., and Dogterom, M. (2006). Assembly dynamics of microtubules at molecular resolution. *Nature*, 442(7103):709–712–.
- [Kim and Rice, 2019] Kim, T. and Rice, L. (2019). Long-range, through-lattice coupling improves predictions of microtubule catastrophe. *Mol Biol Cell*, 30:1451–1462.
- [Kinoshita et al., 2001] Kinoshita, K., Arnal, I., Desai, A., Drechsel, D. N., and Hyman, A. A. (2001). Reconstitution of physiological microtubule dynamics using purified components. *Science*, 294(5545):1340–1343–.
- [Kinoshita et al., 2002] Kinoshita, K., Habermann, B., and Hyman, A. A. (2002). Xmap215: a key component of the dynamic microtubule cytoskeleton. *Trends in Cell Biology*, 12(6):267–273–.
- [Kok et al., 2021] Kok, M., Huber, F., Kalisch, S.-M., and Dogterom, M. (2021). Eb3-informed dynamics of the microtubule stabilizing cap during stalled growth. *bioRxiv*.
- [Komarova et al., 2009] Komarova, Y., Groot, C. O. D., Grigoriev, I., Gouveia, S. M., Munteanu, E. L., Schober, J. M., Honnappa, S., Buey, R. M., Hoogenraad, C. C., Dogterom, M., Borisy, G. G., Steinmetz, M. O., and Akhmanovabru, A. (2009). Mammalian end binding proteins control persistent microtubule growth. *J Cell Biol*, 184(5):691–706.

- [Komarova et al., 2002] Komarova, Y. A., Akhmanova, A. S., Kojima, S.-I., Galjart, N., and Borisy, G. G. (2002). Cytoplasmic linker proteins promote microtubule rescue in vivo. *J Cell Biol*, 159(4):589–599.
- [Laan et al., 2008] Laan, L., Husson, J., Munteanu, E. L., Kerssemakers, J. W. J., and Dogterom, M. (2008). Force-generation and dynamic instability of microtubule bundles. *Proc Natl Acad Sci U S A*, 105(26):8920–8925.
- [Laan et al., 2012] Laan, L., Pavin, N., Husson, J., Romet-Lemonne, G., van Duijn, M., Lopez, M. P., Vale, R. D., Jlicher, F., Reck-Peterson, S. L., and Dogterom, M. (2012). Cortical dynein controls microtubule dynamics to generate pulling forces that position microtubule asters. *Cell*, 148(3):502–514.
- [Lansbergen et al., 2006] Lansbergen, G., Grigoriev, I., Mimori-Kiyosue, Y., Ohtsuka, T., Higa, S., Kitajima, I., Demmers, J., Galjart, N., Houtsmuller, A. B., Grosveld, F., and Akhmanova, A. (2006). Clasps attach microtubule plus ends to the cell cortex through a complex with I15 beta. *Developmental Cell*, 11(1):21–32–.
- [Lee and Terentjev, 2019] Lee, C. and Terentjev, E. (2019). Structural effects of cap, crack, and intrinsic curvature on the microtubule catastrophe kinetics. *J Chem Phys*, 151:135101.
- [Letort et al., 2016] Letort, G., Nedelec, F., Blanchoin, L., and Thery, M. (2016). Centrosome centering and decentering by 988 microtubule network rearrangement. *Mol Biol Cell*, 27:2833–2843.
- [Li and Kolomeisky, 2014] Li, X. and Kolomeisky, A. B. (2014). Theoretical analysis of microtubule dynamics at all times. *The journal of physical chemistry. B*, 118:13777–84.
- [Lombillo et al., 1995] Lombillo, V. A., Stewart, R. J., and McIntosh, J. R. (1995). Minus-end-directed motion of kinesin-coated microspheres driven by microtubule depolymerization. *Nature*, 373(6510):161–164–.
- [Lopez et al., 2014] Lopez, P., M., Huber, F., Grigoriev, I., Steinmetz, M., Akhmanova, A., Koenderink, G., and Dogterom, M. (2014). Actin-microtubule coordination at growing microtubule ends. *Nat Commun*, 5:4778.
- [Lye and McIntosh, 1987] Lye, R. J., P. M. S. J. and McIntosh, J. (1987). Identification of a microtubule-based cytoplasmic motor in the nematode *C. elegans*. *Cell*, 51:309–318–.
- [Mahserejian et al., 2022] Mahserejian, S. M., Scripture, J. P., Mauro, A. J., Lawrence, E. J., Jonasson, E. M., Murray, K. S., Li, J., Gardner, M., Alber, M., Zanic, M., and Goodson, H. V. (2022). Quantification of microtubule stutters: dynamic instability behaviors that are strongly associated with catastrophe. *Molecular biology of the cell*, 33:ar22.
- [Maiato et al., 2004] Maiato, H., DeLuca, J., Salmon, E. D., and Earnshaw, W. C. (2004). The dynamic kinetochore-microtubule interface. *Journal of Cell Science*, 117(23):5461–5477–.
- [Maiato et al., 2003] Maiato, H., Fairley, E. A., Rieder, C. L., Swedlow, J. R., Sunkel, C. E., and Earnshaw, W. C. (2003). Human clasp1 is an outer kinetochore component that regulates spindle microtubule dynamics. *Cell*, 113(7):891 – 904.
- [Mandelkow et al., 1991] Mandelkow, E., Mandelkow, E., and Milligan, R. (1991). Microtubule dynamics and microtubule caps: a time-resolved cryo-electron microscopy study. *J. Cell Biol.*, 114(5):977–991.
- [Mandelkow et al., 1986] Mandelkow, E. M., Schultheiss, R., Rapp, R., Müller, M., and Mandelkow, E. (1986). On the surface lattice of microtubules: helix starts, protofilament number, seam, and handedness. *The Journal of Cell Biology*, 102(3):1067–1073.
- [Margolin et al., 2006] Margolin, G., Gregoret, I., Goodson, H., and Alber, M. (2006). Analysis of a mesoscopic stochastic model of microtubule dynamic instability. *Phys Rev E Stat Nonlin Soft Matter Phys*, 74:41920.
- [Margolin et al., 2012] Margolin, G., Gregoret, I. V., Cickovski, T. M., Li, C., Shi, W., Alber, M. S., and Goodson, H. V. (2012). The mechanisms of microtubule catastrophe and rescue: implications from analysis of a dimer-scale computational model. *Molecular Biology of the Cell*, 23(4):642–656.
- [Maurer et al., 2014] Maurer, S., Cade, N., Bohner, G., Gustafsson, N., Boutant, E., and Surrey, T. (2014). EB1 accelerates two conformational transitions important for microtubule maturation and dynamics. *Curr Biol*, 24:372–384.
- [Maurer et al., 2011] Maurer, S. P., Bieling, P., Cope, J., Hoenger, A., and Surrey, T. (2011). GtpgammaS microtubules mimic the growing microtubule end structure recognized by end-binding proteins (ebs). *Proc Natl Acad Sci U S A*, 108(10):3988–3993.

-
- [Maurer et al., 2012] Maurer, S. P., Fourniol, F. J., Bohner, G., Moores, C. A., and Surrey, T. (2012). Ebs recognize a nucleotide-dependent structural cap at growing microtubule ends. *Cell*, 149(2):371–382.
- [McIntosh et al., 2018] McIntosh, J., O’toole, E., Morgan, G., Austin, J., Ulyanov, E., Ataulkhanov, F., and Gudimchuk, N. (2018). Microtubules grow by the addition of bent guanosine triphosphate tubulin to the tips of curved protofilaments. *J Cell Biol*.
- [McIntosh and Mcdonald, 1989] McIntosh, J. R. and Mcdonald, K. L. (1989). The mitotic spindle. *Scientific American*, 261(4):48–56–.
- [McIntosh and Pfarr, 1991] McIntosh, J. R. and Pfarr, C. M. (1991). Mitotic motors. *The Journal of Cell Biology*, 115(3):577–585.
- [Meadows et al., 2018] Meadows, J., Messin, L., Kamnev, A., Lancaster, T., Balasubramanian, M., Cross, R., and Millar, J. (2018). Opposing kinesin complexes queue at plus tips to ensure microtubule catastrophe at cell ends. *EMBO Rep*, 19.
- [Michaels et al., 2020] Michaels, T., Feng, S., Liang, H., and Mahadevan, L. (2020). Mechanics and kinetics of dynamic instability.
- [Mickey and Howard, 1995] Mickey, B. and Howard, J. (1995). Rigidity of microtubules is increased by stabilizing agents. *Journal of Cell Biology*, 130(4):909–917–.
- [Mickolajczyk et al., 2019] Mickolajczyk, K. J., Geyer, E. A., Kim, T., Rice, L. M., and Hancock, W. O. (2019). Direct observation of individual tubulin dimers binding to growing microtubules. *Proceedings of the National Academy of Sciences*, 116(15):7314–7322.
- [Mimori-Kiyosue et al., 2005] Mimori-Kiyosue, Y., Grigoriev, I., Lansbergen, G., Sasaki, H., Matsui, C., Severin, F., Galjart, N., Grosveld, E., Vorobjev, I., Tsukita, S., and Akhmanova, A. (2005). Clasp1 and clasp2 bind to eb1 and regulate microtubule plus-end dynamics at the cell cortex. *The Journal of Cell Biology*, 168(1):141–153.
- [Mimori-Kiyosue et al., 2000] Mimori-Kiyosue, Y., Shiina, N., and Tsukita, S. (2000). The dynamic behavior of the apc-binding protein eb1 on the distal ends of microtubules. *Current Biology*, 10(14):865–868–.
- [Mitchison and Kirschner, 1984a] Mitchison, J. and Kirschner, M. (1984a). Dynamic instability of microtubule growth. *nature*, 312:237–242–.
- [Mitchison and Kirschner, 1984b] Mitchison, J. and Kirschner, M. (1984b). Microtubule assembly nucleated by isolated centrosomes. *nature*, 312:232–237–.
- [Mitchison, 1988] Mitchison, T. (1988). Microtubule dynamics and kinetochore function in mitosis. *Annu Rev Cell Biol*, 4:527–49.
- [Mitchison and Kirschner, 1987] Mitchison, T. J. and Kirschner, M. W. (1987). Some thoughts on the partitioning of tubulin between monomer and polymer under conditions of dynamic instability. *Cell Biophys*, 11:35–55.
- [Mogilner and Oster, 1999] Mogilner, A. and Oster, G. (1999). The polymerization ratchet model explains the force-velocity relation for growing microtubules. *Eur. Biophys. J. Biophys. Lett.*, 28(3):235–242–.
- [Mohan et al., 2013] Mohan, R., Katrukha, E., Doodhi, H., Smal, I., Meijering, E., Kapitein, L., Steinmetz, M., and Akhmanova, A. (2013). End-binding proteins sensitize microtubules to the action of microtubule-targeting agents. *Proc Natl Acad Sci U S A*, 110:8900–8905.
- [Molodtsov et al., 2005a] Molodtsov, M. I., Ermakova, E. A., Shnol, E. E., Grishchuk, E. L., McIntosh, J. R., and Ataulkhanov, F. I. (2005a). A molecular-mechanical model of the microtubule. *Biophysical Journal*, 88(5):3167–3179–.
- [Molodtsov et al., 2005b] Molodtsov, M. I., Grishchuk, E. L., Efremov, A. K., McIntosh, J. R., and Ataulkhanov, F. I. (2005b). Force production by depolymerizing microtubules: A theoretical study. *Proceedings of the National Academy of Sciences of America*, 102(12):4353–4358–.
- [Moudjou and Bornens, 1994] Moudjou, M. and Bornens, M. (1994). Isolation of centrosomes from cultured animal cells. *Cell Biology: A Laboratory Handbook*, ed. J.E.Celis Academic Press, New York, pages 595–604.–.
-

- [Munteanu, 2008] Munteanu, E. M. (2008). *Dynamics and regulation at the tip*. PhD thesis, Leiden University.
- [Neuman and Block, 2004] Neuman, K. C. and Block, S. M. (2004). Optical trapping. *Rev. Sci. Instrum.*, 75(9):2787–2809.
- [Nguyen-Ngoc et al., 2007] Nguyen-Ngoc, T., Afshar, K., and Gonczy, P. (2007). Coupling of cortical dynein and Ga proteins mediates spindle positioning in *Caenorhabditis elegans*. *Nat Cell Biol*, 9:1294–1302.
- [Nogales, 1999] Nogales, E. (1999). A structural view of microtubule dynamics. *Cell Mol Life Sci*, 56:133–142.
- [Nogales, 2000] Nogales, E. (2000). Structural insights into microtubule function. *Annu Rev Biochem*, 69:277–302.
- [Odde et al., 1995] Odde, D., Cassimeris, L., and Buettner, H. (1995). Kinetics of microtubule catastrophe assessed by probabilistic analysis. *Biophysical Journal*, 69(3):796 – 802.
- [Odde et al., 1999] Odde, D., Ma, L., Briggs, A., Demarco, A., and Kirschner, M. (1999). Microtubule bending and breaking in living fibroblast cells. *J Cell Sci*, 112:3283–3288.
- [Odde et al., 1996] Odde, D. J., Buettner, H. M., and Cassimeris, L. (1996). Spectral analysis of microtubule assembly dynamics. *AICHE J.*, 42(5):1434–1442.
- [Ohi and Zanic, 2016] Ohi, R. and Zanic, M. (2016).
- [Padinhateeri et al., 2012] Padinhateeri, R., Kolomeisky, A., and Lacoste, D. (2012). Random hydrolysis controls the dynamic instability of microtubules. *Biophys J*, 102:1274–1283.
- [Pallavicini et al., 2017] Pallavicini, C., Monastra, A., Bardeci, N., Wetzler, D., Levi, V., and Bruno, L. (2017). Characterization of microtubule buckling in living cells. *Eur Biophys J*.
- [Pampaloni et al., 2006] Pampaloni, E., Lattanzi, G., JonÅrÅ, A., Surrey, T., Frey, E., and Florin, E.-L. (2006). Thermal fluctuations of grafted microtubules provide evidence of a length-dependent persistence length. *Proceedings of the National Academy of Sciences*, 103(27):10248–10253.
- [Parry and Brown, 1959] Parry, D. A. and Brown, R. H. J. (1959). The hydraulic mechanism of the spider leg. *Journal of Experimental Biology* 36, 2:423–433.
- [Perez et al., 1999] Perez, F., Diamantopoulos, G. S., Stalder, R., and Kreis, T. E. (1999). Clip-170 highlights growing microtubule ends in vivo. *Cell*, 96(4):517–527–.
- [Peskin et al., 1993] Peskin, C. S., Odell, G. M., and Oster, G. F. (1993). Cellular motions and thermal fluctuations - the brownian ratchet. *Biophys. J.*, 65(1):316–324–.
- [Pham, 2004] Pham, H. (2004). PE-CVD Silicon Carbide - a structured material for surface micromachined devices. Technical report.
- [Phillips R., 2008] Phillips R., Kondev J., T. J. (2008). *Physical Biology of the Cell*. Garland Science.
- [Piedra et al., 2016] Piedra, F., Kim, T., Garza, E., Geyer, E., Burns, A., Ye, X., and Rice, L. (2016). GDP-to-GTP exchange on the microtubule end can contribute to the frequency of catastrophe. *Mol Biol Cell*, 27:3515–3525.
- [Rice, 1995] Rice, J. (1995). *Mathematical Statistics and Data Analysis*. Duxbury Press.
- [Rickman et al., 2017] Rickman, J., Duellberg, C., Cade, N., Griffin, L., and Surrey, T. (2017). Steady-state EB cap size fluctuations are determined by stochastic microtubule growth and maturation. *Proc Natl Acad Sci U S A*, 114:3427–3432.
- [Roth et al., 2018] Roth, D., Fitton, B., Chmel, N., Wasiluk, N., and Straube, A. (2018). Spatial positioning of EB family proteins at microtubule tips involves distinct nucleotide-dependent binding properties. *J Cell Sci*, 132.
- [Sandblad et al., 2006] Sandblad, L., Busch, K. E., Tittmann, P., Gross, H., Brunner, D., and Hoenger, A. (2006). The schizosaccharomyces pombe eb1 homolog mal3p binds and stabilizes the microtubule lattice seam. *Cell*, 127(7):1415–1424–.
- [Schaedel et al., 2019] Schaedel, L., Triclin, S., Chrétien, D., Abrieu, A., Aumeier, C., Gaillard, J., Blanchoin, L., Théry, M., and John, K. (2019). Lattice defects induce microtubule self-renewal. *Nature Physics*, 15(8):830–838.

-
- [Schek et al., 2007] Schek, H. T., Gardner, M. K., Cheng, J., Odde, D. J., and Hunt, A. J. (2007). Microtubule assembly dynamics at the nanoscale. *Current Biology*, 17(17):1445–1455–.
- [Schek and Hunt, 2005] Schek, H. T. and Hunt, A. J. (2005). Micropatterned structures for studying the mechanics of biological polymers. *Biomed. Microdevices*, 7(1):41–46–.
- [Schindelin et al., 2012] Schindelin, J., Arganda-Carreras, I., Frise, E., Kaynig, V., Longair, M., Pietzsch, T., Preibisch, S., Rueden, C., Saalfeld, S., Schmid, B., Tinevez, J., White, D., Hartenstein, V., Eliceiri, K., Tomancak, P., and Cardona, A. (2012). Fiji: an open-source platform for biological-image analysis. *Nat Methods*, 9:676–682.
- [Seetapun et al., 2012] Seetapun, D., Castle, B., McIntyre, A., Tran, P., and Odde, D. (2012). Estimating the microtubule gtp cap size in vivo. *Current Biology*, (0):–.
- [Sept et al., 2003] Sept, D., Baker, N. A., and McCammon, J. A. (2003). The physical basis of microtubule structure and stability. *Protein Sci*, 12(10):2257–2261.
- [Simmons et al., 1996] Simmons, R. M., Finer, J. T., Chu, S., and Spudich, J. A. (1996). Quantitative measurements of force and displacement using an optical trap. *Biophys J*, 70(4):1813–1822.
- [Sirajuddin et al., 2014] Sirajuddin, M., Rice, L., and Vale, R. (2014). Regulation of microtubule motors by tubulin isotypes and post-translational modifications. *Nat Cell Biol*, 16:335–344.
- [Stepanova et al., 2010] Stepanova, T., Smal, I., van Haren, J., Akinci, U., Liu, Z., Miedema, M., Limpens, R., van Ham, M., van der Reijden, M., Poot, R., Grosveld, F., Mommaas, M., Meijering, E., and Galjart, N. (2010). History-dependent catastrophes regulate axonal microtubule behavior. *Curr Biol*.
- [Stukalin and Kolomeisky, 2004] Stukalin, E. B. and Kolomeisky, A. B. (2004). Simple growth models of rigid multifilament biopolymers. *J. Chem. Phys.*, 121(2):1097–1104.
- [Svoboda and Block, 1994] Svoboda, K. and Block, S. M. (1994). Force and velocity measured for single kinesin molecules. *Cell*, 77(5):773–784–.
- [Taberner et al., 2014] Taberner, N., Weber, G., You, C., Dries, R., Piehler, J., and Dogterom, M. (2014). Reconstituting functional microtubule-barrier interactions. *Methods Cell Biol*, 120:69–90.
- [Tilney et al., 1973] Tilney, L. G., Bryan, J., Bush, D. J., Fujiwara, K., Mooseker, M. S., Murphy, D. B., and Snyder, D. H. (1973). Microtubules: evidence for 13 protofilaments. *The Journal of cell biology*, 59:267–275.
- [Tirnauer et al., 2002] Tirnauer, J. S., Grego, S., Salmon, E. D., and Mitchison, T. J. (2002). Eb1-microtubule interactions in xenopus egg extracts: Role of eb1 in microtubule stabilization and mechanisms of targeting to microtubules. *Molecular Biology of the Cell*, 13(10):3614–3626–.
- [Tischer et al., 2009] Tischer, C., Brunner, D., and Dogterom, M. (2009). Force-and kinesin-8-dependent effects in the spatial regulation of fission yeast microtubule dynamics. *molecular systems biology*, pages –.
- [Tolic-Norrelykke et al., 2005] Tolic-Norrelykke, I. M., Sacconi, L., Stringari, C., Raabe, I., and Pavone, F. S. (2005). Nuclear and division-plane positioning revealed by optical micromanipulation. *Current Biology*, 15(13):1212–1216–.
- [Tolic-Norrelykke et al., 2004] Tolic-Norrelykke, I. M., Sacconi, L., Thon, G., and Pavone, F. S. (2004). Positioning and elongation of the fission yeast spindle by microtubule-based pushing. *Current Biology*, 14(13):1181–1186–.
- [Tran et al., 2001] Tran, P., Marsh, L., Doye, V., Inoue, S., and Chang, F. (2001). A mechanism for nuclear positioning in fission yeast based on microtubule pushing. *J. Cell Biol.*, 153(2):397–411–.
- [Tran et al., 1997] Tran, P. T., Joshi, P., and Salmon, E. D. (1997). How tubulin subunits are lost from the shortening ends of microtubules. *Journal of Structural Biology*, 118(2):107–118–.
- [Vale, 1985] Vale, R. D. (1985). Identification of a novel force generating protein, kinesin. *Cell*, 42:39–50–.
- [Valiyakath and Gopalakrishnan, 2018] Valiyakath, J. and Gopalakrishnan, M. (2018). Polymerisation force of a rigid filament bundle: diffusive interaction leads to sublinear force-number scaling. *Sci Rep*, 8:2526.

- [Vallee and Stehman, 2005] Vallee, R. B. and Stehman, S. A. (2005). How dynein helps the cell find its center: a servomechanical model. *Trends in Cell Biology*, 15(6):288–294–.
- [van Doorn et al., 2000] van Doorn, G. S., Tanase, C., Mulder, B. M., and Dogterom, M. (2000). On the stall force for growing microtubules. *European Biophysics Journal with Biophysics Letters*, 29(1):2–6–.
- [VanBuren et al., 2005] VanBuren, V., Cassimeris, L., and Odde, D. J. (2005). Mechanochemical model of microtubule structure and self-assembly kinetics. *Biophysical Journal*, 89(5):2911–2926–.
- [VanBuren et al., 2002] VanBuren, V., Odde, D. J., and Cassimeris, L. (2002). Estimates of lateral and longitudinal bond energies within the microtubule lattice. *Proc Natl Acad Sci U S A*, 99(9):6035–6040.
- [Visscher et al., 1999] Visscher, K., Schnitzer, M. J., and Block, S. M. (1999). Single kinesin molecules studied with a molecular force clamp. *Nature*, 400(6740):184–189.
- [Vitre et al., 2008] Vitre, B., Coquelle, F. M., Heichette, C., Garnier, C., Chretien, D., and Arnal, I. (2008). Eb1 regulates microtubule dynamics and tubulin sheet closure in vitro. *Nature Cell Biology*, 10(4):415–U81–.
- [Vleugel et al., 2016] Vleugel, M., Kok, M., and Dogterom, M. (2016). Understanding force-generating microtubule systems through in vitro reconstitution. *Cell Adh Migr*, pages 475–494.
- [Vogel et al., 2007] Vogel, S. K., Raabe, I., Dereli, A., Maghelli, N., and Tolic-Norrelykke, I. (2007). Interphase microtubules determine the initial alignment of the mitotic spindle. *Current Biology*, 17(5):438–444–.
- [Von Loeffelholz et al., 2017] Von Loeffelholz, O., Venables, N., Drummond, D., Katsuki, M., Cross, R., and Moores, C. (2017). Nucleotide- and Mal3-dependent changes in fission yeast microtubules suggest a structural plasticity view of dynamics. *Nat Commun*, 8:2110.
- [Walker et al., 1991] Walker, R., Pryer, N., and Salmon, E. (1991). Dilution of individual microtubules observed in real time in vitro: evidence that cap size is small and independent of elongation rate. *J Cell Biol*, 114:73–81.
- [Walker et al., 1988] Walker, R. A., O'Brien, E. T., Pryer, N. K., Soboeiro, M. F., Voter, W. A., Erickson, H. P., and Salmon, E. D. (1988). Dynamic instability of individual microtubules analyzed by video light-microscopy - rate constants and transition frequencies. *J. Cell Biol.*, 107(4):1437–1448–.
- [Wang et al., 2005] Wang, H. W., Long, S., Finley, K. R., and Nogales, E. (2005). Assembly of gmpcpp-bound tubulin into helical ribbons and tubes and effect of colchicine. *Cell Cycle*, 4(9):1157–1160–.
- [Wang and Nogales, 2005] Wang, H. W. and Nogales, E. (2005). Nucleotide-dependent bending flexibility of tubulin regulates microtubule assembly. *Nature*, 435(7044):911–915–.
- [Waterman-Storer et al., 1995] Waterman-Storer, C., Gregory, J., Parsons, S., and Salmon, E. (1995). Membrane/microtubule tip attachment complexes (TACs) allow the assembly dynamics of plus ends to push and pull membranes into tubulovesicular networks in interphase *Xenopus* egg extracts. *J Cell Biol*, 130:1161–1169.
- [Yeaman et al., 1999] Yeaman, C., Grindstaff, K. K., and Nelson, W. J. (1999). New perspectives on mechanisms involved in generating epithelial cell polarity. *Physiological Reviews*, 79(1):73–98–.
- [Zakharov et al., 2015] Zakharov, P., Gudimchuk, N., Voevodin, V., Tikhonravov, A., Ataulakhanov, F., and Grishchuk, E. (2015). Molecular and mechanical causes of microtubule catastrophe and aging. *Biophys J*, 109:2574–2591.
- [Zhang et al., 2015] Zhang, R., Alushin, G., Brown, A., and Nogales, E. (2015). Mechanistic origin of microtubule dynamic instability and its modulation by EB proteins. *Cell*, 162:849–859.
- [Zhou and Zhuang, 2007] Zhou, Y. and Zhuang, X. (2007). Kinetic analysis of sequential multistep reactions. *J. Phys. Chem. B*, 111(48):13600–13610.

Summary

(in interview form)

This thesis deals with “microtubules” and “catastrophes”? Can you explain in simple words for a layman what is meant with these terms?

Let's first look at a spider. It is a complex creature with many different body parts but basically all of them are composed of one building block: the cell. That means that cells exist in many different shapes and sizes with many different functions. Still, these cells have much in common. Almost all of them contain a nucleus containing the hereditary information and a scaffold to give it shape and assist internal organisation. One of the filaments which comprise this scaffold are “microtubules” (MTs). They look like long rods and can span the whole cell. One special feature is that they are dynamic: like building a tower from Lego, the building blocks for children, MTs assemble from a smaller subunit, termed “tubulin”. Also similar to children's play with Lego, the MT alternates between periods of build-up and breakdown. The sudden switch to a disassembly period is called catastrophe.

Why do you want to study MT catastrophes?

As I said, the cell has many different functions. Failure in proper execution can ultimately lead to sickness or even death of the organism. To avoid this, it is important that the cell's tasks are fulfilled properly which can only be achieved by tight regulation. MTs play a crucial role in this. As they infer a framework to an ever-changing cell and serve as guiding structures for delivering cargo and signals, they need to be built up (which we call “grow”) at the right time and space. Similarly, their other dynamic instability parameters: their breakdown (which we call “shrinkage”) and the switch from growth to shrinkage, catastrophe, or vice versa from shrinkage to growth, need to be regulated.

Can you be more specific in what you want to know about catastrophes?

Yes. It was thought for long time that catastrophes occur suddenly, at a random time [Hill, 1984, Mitchison and Kirschner, 1987, Dogterom and Leibler, 1993, Flyvbjerg et al., 1994, Howard, 2001, Phillips R., 2008]. Later, another idea in research came up thinking that a catastrophe happens progressively in several steps [Odde et al., 1995, Odde et al., 1996, Stepanova et al., 2010, Gardner et al., 2011b]. We want to examine whether this is indeed the case and what is the cause of catastrophe. How many steps is the catastrophe process composed of, what is the nature of the step(s). As I mentioned MTs need tight regulation for proper functioning. This thesis deals with two MT regulators: proteins and compressive forces generated

when MTs encounter an intracellular obstacle. We want to understand how both these factors influence MT catastrophes.

What are these proteins?

Cells contain a lot of different proteins associated with microtubules. In order to uncouple their regulatory effect we do *in vitro* experiments with three highly conserved proteins known to influence MT dynamics [Beinhauer et al., 1997, Brunner and Nurse, 2000a]. This makes them biologically very relevant. Our proteins are known to interact with each other and are all from fission yeast: mal3, tea2 and tip1 [Busch et al., 2004, Busch and Brunner, 2004]. They belong to a class of microtubule-associated proteins which bind specifically to the MT ends. That's why they are called "end-binding proteins" (EBs).

What are your methods to examine MT catastrophes, EBs and force?

The methods are described in chapter 2 of this thesis. All the experiments are performed *in-vitro* in flow chambers containing on the bottom surface rigid, custom-made grooves. MTs assembled in these grooves from stabilised MT seeds grow against the rigid barriers where they experience compressive forces. This imitates the interaction of MTs and the cell wall. In the flow chamber is tubulin and also the EBs. Using a TIRF microscope we can specifically illuminate the fluorescently-tagged EBs and tubulin at the chamber surface between the grooves. We also use optical tweezers where we nucleated MTs from an axoneme (serving as a MT nucleation template) which is attached to a trapped bead. We direct the MTs against a rigid barrier in the presence and absence of EBs. The growth of the MTs against the barrier results in displacement of the bead from the trap centre which we can measure with high spatial and temporal resolution. We can thus deduce MT growth and force generation from these measurements. Furthermore, we also do experiments at constant force conditions where a growth of the MT results in translation of the barrier and constant location of the bead.

So what do you observe with the microscope? What do you learn from it?

We first looked at the binding dynamics of the end-binding protein mal3 in chapter 3. We observed the fluorescent accumulation at the growing MT end and examined how it altered before, during and after catastrophe. This we did for free MTs and for MTs in contact with a barrier. We saw, as already mentioned in [Maurer et al., 2011], that mal3 starts unbinding from the free MT, on average 15 s before catastrophe. This decrease of mal3 intensity stops about 5 s after catastrophe when the lattice intensity is reached. When MTs are under force it is similar, just that the decrease of intensity is now timed with the establishment of barrier-contact instead of with catastrophe.

Why do you see mal3 unbinding with a free catastrophe or establishment of barrier-contact?

Maurer et al [Maurer et al., 2011, Maurer et al., 2012] proposed a model where the tubulin at the very tip of the MT is in another nucleotide conformation than tubulin farther from the tip (termed the “EB1-competent state”) or the tubulin in the lattice. The authors suggest that mal3 only binds to the nucleotide state of tubulin in the EB1-competent state. The decrease of mal3’s affinity to the MT must therefore mean the loss of its binding sites [Maurer et al., 2012]. As a consequence we reason catastrophe or a compressive force (upon barrier contact) to provoke the omission of the EB1-competent state.

What do you know about the catastrophe process?

In chapter 4 we examined the catastrophe process of free MTs. We measured the catastrophe time, the time spanned from nucleation off the seed until catastrophe, in three conditions: free MTs in the absence of EBs, in the presence of mal3 and in the presence of the three EBs: mal3, tea2, and tip1. However, since it is experimentally difficult to determine the lifetime of very short MTs we have an uncertainty in the short catastrophe events. To account for this we fitted our unbinned data with several truncated distributions. The distributions describe multistep reactions with irreversible sequential and parallel steps, where the steps are or are not restricted to have the same timescale (gamma, (parallel) two-step exponential and multistep exponential distributions). We observed that in all our three conditions catastrophe is a multistep process as suggested before [Gardner et al., 2011b]. Moreover, we propose catastrophe to consist of (almost) two steps of unequal timescales. Comparing the observed timescales to the results from chapter 3, the timescales of mal3 unbinding, we conclude that the shorter step of the two must be characterised by the loss of mal3. Therefore, it cannot be the first step. At the moment we cannot say more about the nature of the other, longer step nor can we be sure about the steps being consecutive.

Special about your data is that you let MTs grow against a barrier. Do compressive forces influence the catastrophe process?

That we examined in chapter 5. We measured the time spanned from establishment of barrier-contact until catastrophe of stalling MTs. As expected, we measured that the force speeds up the catastrophe process. More interestingly, under force there is a clear effect of the EBs: in their absence, the catastrophe process consists of more than two steps, while in their presence the catastrophe process seems to become a random reaction. Taking the results from chapter 3, the loss of mal3 with establishment of force, we suggest that the random step in the presence of EBs is connected to the loss of the EB1-competent state. As for the MTs in pure tubulin: we do not have an explanation for the increase of number of steps at the moment.

Previous data suggested that an increase in the catastrophe rate stems from a decrease of the tubulin on-rate [Janson et al., 2003]. Could that be the case in your experiments?

Indeed, that is what we examined in chapter 6. By using optical tweezers, optionally with force-feedback, we could measure both the growth speed and the generated force with high resolution. Surprisingly, the absence or presence of EBs did not cause an obvious difference in the force – growth speed relationship in the force range we measured ($F > 0.5 \text{ pN}$). We assume that this is caused by the loss of EBs upon establishment of force (see chapter 3) and the subsequent growth of the MT in the absence of EB binding.

There are still a few open questions...

Indeed, we examined the effect of *mal3*, *tea2* and *tip1* on the catastrophe process. However, we do not know much about the correlated binding dynamics of the three EBs. Further, there might be a connection between growth speed and the accomplishment of catastrophe-promoting events. For these problems we provide preliminary data. We also do not know the nature of all the steps leading to catastrophe. Connected to this we cannot resolve the puzzle why a force increases the number of steps of force-loaded MTs. We discuss possible, putative scenarios like a third step, non-detected in the free MT data but recovered at the barrier, and further distributions involving fixed-duration or reversible steps. We do not think that the former is the case while both latter scenarios seem realistic.

Samenvatting

(in interviewvorm)

Dit proefschrift gaat over "microtubules" en "catastrofes"? Kunt u in eenvoudige woorden voor een leek uitleggen wat met deze termen bedoeld wordt?

Laten we eerst eens kijken naar een spin. Het is een complex wezen met veel verschillende lichaamsdelen, maar in wezen zijn ze allemaal opgebouwd uit één bouwsteen: de cel. Dat betekent dat cellen bestaan in veel verschillende vormen en maten met veel verschillende functies. Toch hebben deze cellen veel gemeen. Bijna allemaal bevatten ze een kern die de erfelijke informatie bevat en een cytoskelet om de cel vorm te geven en te helpen bij de interne organisatie. Een van de filamenten waaruit deze cytoskelet is opgebouwd zijn "microtubuli" (MT's). Zij zien eruit als lange kabels en kunnen de hele cel omspannen. Een bijzonder kenmerk is dat ze dynamisch zijn: zoals kinderen een toren bouwen van Lego, de bouwstenen voor kinderen, zo worden MT's opgebouwd uit een kleinere subeenheid, tubuline genaamd. Ook vergelijkbaar met het spel van kinderen met Lego, wisselt het MT af tussen perioden van opbouw en afbraak. De plotselinge overgang naar een afbraakperiode wordt catastrofe genoemd.

Waarom wil je MT catastrofes bestuderen?

Zoals ik al zei, heeft de cel veel verschillende functies. Wanneer deze niet naar behoren worden uitgevoerd, kan dit uiteindelijk leiden tot ziekte of zelfs de dood van het organisme. Om dit te voorkomen is het belangrijk dat de taken van de cel naar behoren worden vervuld, wat alleen kan worden bereikt door een strakke regulering. MT's spelen hierbij een cruciale rol. Aangezien zij een kader geven aan een steeds veranderende cel en dienen als leidende structuren voor het afleveren van lading en signalen, moeten zij op het juiste moment en op de juiste plaats worden opgebouwd (wat wij "groeien" noemen). Evenzo moeten hun andere dynamische instabiliteitsparameters: hun afbraak (die wij "krimp" noemen) en de omschakeling van groei naar krimp, catastrofe, of omgekeerd van krimp naar groei, worden gereguleerd.

Kunt u specifieker zijn in wat u wilt weten over catastrofes?

Ja. Lange tijd werd gedacht dat catastrofes plotseling optreden, op een willekeurig moment [Hill, 1984, Mitchison and Kirschner, 1987, Dogterom and Leibler, 1993, Flyvbjerg et al., 1994, Howard, 2001, Phillips R., 2008]. Later is een ander idee in het onderzoek naar voren gekomen, namelijk dat een catastrofe geleidelijk in verschillende stappen plaatsvindt [Odde et al., 1995, Odde et al., 1996, Stepanova et al.,

2010, Gardner et al., 2011b]. Wij willen onderzoeken of dit inderdaad het geval is en wat de oorzaak van een catastrofe is. Uit hoeveel stappen bestaat het catastrofe proces, wat is de aard van de stap(pen). Zoals ik al zei moeten MT's strak gereguleerd worden om goed te kunnen functioneren. Dit proefschrift gaat over twee MT-regulatoren: eiwitten en drukkrachten die ontstaan wanneer MT's op een intracellulair obstakel stuiten. We willen begrijpen hoe deze twee factoren MT catastrofes beïnvloeden.

Wat zijn deze proteïnen?

Cellen bevatten een groot aantal verschillende eiwitten die geassocieerd zijn met microtubuli. Om hun regulerende werking te ontkoppelen doen we *in vitro* experimenten met drie sterk geconserveerde eiwitten waarvan bekend is dat ze de MT dynamica beïnvloeden. Dit maakt ze biologisch zeer relevant. Van onze eiwitten is bekend dat ze met elkaar interageren en ze zijn allemaal afkomstig van fission yeast: mal3, tea2 en tip1 [Busch et al., 2004, Busch and Brunner, 2004]. Zij behoren tot een klasse van microtubule-geassocieerde eiwitten die zich specifiek binden aan de MT uiteinden. Daarom worden ze "end-binding proteins" (EB's) genoemd.

Wat zijn uw methodes om MT catastrofes, EB's en kracht te onderzoeken?

De methoden worden beschreven in hoofdstuk 2 van dit proefschrift. Alle experimenten worden *in vitro* uitgevoerd in stroomkamers met aan de onderzijde stijve, op maat gemaakte groeven. MT's die in deze groeven zijn geassembleerd uit gestabiliseerde MT-zaden groeien tegen de starre barrières waar ze drukkrachten ondervinden. Dit imiteert de interactie tussen MT's en de celwand. In de stroomkamer bevinden zich tubuline en ook de EB's. Met een TIRF-microscoop kunnen we de fluorescent gemerkte EB's en tubuline aan het oppervlak van de kamer tussen de groeven specifiek belichten. We maken ook gebruik van een optisch pincet waarbij we MT's kernen uit een axonoom (dat dient als MT-kiemtemplate) dat aan een gevangen kraal is bevestigd. We richten de MT's tegen een rigide barrière in de aanwezigheid en afwezigheid van EB's. De groei van de MT's tegen de barrière resulteert in verplaatsing van de kraal van het centrum van de val die we kunnen meten met een hoge ruimtelijke en temporele resolutie. Uit deze metingen kunnen we dus MT-groei en krachtontwikkeling afleiden. Bovendien doen we ook experimenten bij constante kracht, waarbij een groei van het MT resulteert in een verplaatsing van de barrière en een constante plaats van de kraal.

Dus wat observeer je met de microscoop? Wat leer je ervan?

We hebben eerst gekeken naar de bindingsdynamica van het eindbindende eiwit mal3 in hoofdstuk 3. We observeerden de fluorescente accumulatie aan het groeiende MT uiteinde en onderzochten hoe deze veranderde voor, tijdens en na catastrofe. Dit deden we voor vrije MT's en voor MT's in contact met een barrière. We zagen, zoals reeds vermeld in [Maurer et al., 2011], dat mal3 begint te ontbinden van het vrije MT, gemiddeld 15 s voor de catastrofe. Deze afname van de mal3 intensiteit stopt ongeveer 5 s na de catastrofe wanneer de roosterintensiteit

wordt bereikt. Wanneer MTs onder kracht staan is het vergelijkbaar, alleen is de afname van de intensiteit nu getimed met het tot stand komen van barrière-contact in plaats van met catastrofe.

Waarom zie je mal3 ontbinden met een vrije catastrofe of vestiging van barrière-contact?

Maurer e.a. stelden een model voor waarbij tubuline aan de top van het MT een andere conformatie heeft dan tubuline verder van de top (de zogenaamde EB1-competente toestand) of tubuline in het rooster. De auteurs suggereren dat mal3 alleen bindt aan de nucleotidetoestand van tubuline in de EB1-competente toestand. De afname van de affiniteit van mal3 voor het MT moet daarom het verlies van zijn bindingsplaatsen betekenen (Maurer 2012). Bijgevolg redeneren we dat catastrofe of een drukkracht (bij barrièrecontact) het wegvallen van de EB1-competente toestand uitlokt.

Wat weet je over het catastrofe proces?

In hoofdstuk 4 hebben we het catastrofe proces van vrije MTs onderzocht. We hebben de catastrofe tijd gemeten, de tijd die verstrijkt tussen de nucleatie en de catastrofe, in drie condities: vrije MTs in de afwezigheid van EBs, in de aanwezigheid van mal3 en in de aanwezigheid van de drie EBs: mal3, tea2, en tip1. Aangezien het experimenteel moeilijk is om de levensduur van zeer korte MT's te bepalen, hebben we echter een onzekerheid in de korte catastrofegebeurtenissen. Om hiermee rekening te houden pasten we onze ongebundelde gegevens aan met verschillende afgeknotte verdelingen. De verdelingen beschrijven meerstapsreacties met onomkeerbare sequentiële en parallelle stappen, waarbij de stappen al dan niet beperkt zijn tot dezelfde tijdschaal (gamma-, (parallelle) tweestaps exponentiële en meerstaps exponentiële verdelingen). Wij hebben vastgesteld dat in al onze drie omstandigheden catastrofe een meerstapsproces is, zoals eerder gesuggereerd. Bovendien stellen we voor dat catastrofe bestaat uit (bijna) twee stappen met ongelijke tijdschalen. Als we de waargenomen tijdschalen vergelijken met de resultaten uit hoofdstuk 3, de tijdschalen van mal3 ontbinding, concluderen we dat de kortste stap van de twee gekenmerkt moet worden door het verlies van mal3. Het kan dus niet de eerste stap zijn. Op dit moment kunnen we niet meer zeggen over de aard van de andere, langere stap, noch kunnen we er zeker van zijn dat de stappen opeenvolgend zijn.

Het bijzondere aan je gegevens is dat je MT's tegen een barrière laat groeien. Hebben drukkrachten invloed op het catastrofe proces?

Dat hebben we onderzocht in hoofdstuk 5. We hebben de tijd gemeten vanaf het tot stand komen van het barrière-contact tot aan de catastrofe van de MT's die vastlopen. Zoals verwacht, hebben we gemeten dat de kracht het catastrofe-proces versnelt. Interessanter is dat er onder kracht een duidelijk effect is van de EB's: in afwezigheid van EB's bestaat het catastrofe-proces uit meer dan twee stappen, terwijl in aanwezigheid van EB's het catastrofe-proces een willekeurige reactie lijkt te

worden. Uitgaande van de resultaten van hoofdstuk 3, het verlies van mal3 met vestiging van kracht, suggereren we dat de willekeurige stap in de aanwezigheid van EB's samenhangt met het verlies van de EB1-competente toestand. Wat betreft de MT's in zuiver tubuline: we hebben op dit moment geen verklaring voor de toename van het aantal stappen.

Eerdere gegevens suggereerden dat een toename van de catastrofesnelheid het gevolg is van een afname van de tubuline aan-snelheid. Zou dat in uw experimenten het geval kunnen zijn?

Dat is inderdaad wat wij in hoofdstuk 6 hebben onderzocht. Door gebruik te maken van een optisch pincet, eventueel met force-feedback, konden we zowel de groeisnelheid als de opgewekte kracht met hoge resolutie meten. Verrassend genoeg veroorzaakte de aan- of afwezigheid van EB's geen duidelijk verschil in de kracht - groeisnelheid relatie in het krachtbereik dat we gemeten hebben ($F > 0.5 \text{ pN}$). We nemen aan dat dit wordt veroorzaakt door het verlies van EB's bij het tot stand komen van de kracht (zie hoofdstuk 3) en de daaropvolgende groei van het MT in afwezigheid van EB-binding.

Er zijn nog een paar open vragen...

Wij hebben inderdaad het effect van mal3, tea2 en tip1 op het catastrofe-proces onderzocht. We weten echter niet veel over de gecorreleerde bindingsdynamiek van de drie EB's. Verder zou er een verband kunnen bestaan tussen de groeisnelheid en het bereiken van catastrofe-bevorderende gebeurtenissen. Voor deze problemen geven wij voorlopige gegevens. Wij kennen ook niet de aard van alle stappen die tot de catastrofe leiden. Hiermee samenhangend kunnen we het raadsel niet oplossen waarom een kracht het aantal stappen van met kracht belaste MTs verhoogt. We bespreken mogelijke, vermeende scenario's zoals een derde stap, niet gedetecteerd in de vrije MT-gegevens maar teruggevonden bij de barrière, en verdere verdelingen met stappen van vaste duur of omkeerbare stappen. Wij denken niet dat het eerste het geval is, terwijl beide laatste scenario's realistisch lijken.

This thesis is partly based on the following publications:

Kalisch SMJ, Laan L, and Dogterom M (2011). Microtubule dynamics : methods and protocols. In *Springer Protocols. Methods in Molecular Biology*, volume **777**, pages Chap. 11: 147–165. Humana; Springer, New York.
(chapter 2)

Baclayon M, **Kalisch SMJ**, Hendel E, Laan L, Husson J, Munteanu EL, Dogterom M. (2017) Optical Tweezers-Based Measurements of Forces and Dynamics at Microtubule Ends. *Methods Mol Biol.* **1486**:411-435.
(chapter 6)

Kok M, Huber F, **Kalisch SMJ**, Dogterom M. *EB3-informed dynamics of the microtubule stabilizing cap during stalled growth.* Published as preprint on www.biorxiv.org/content/10.1101/2021.12.07.471417v1.full#F2. (chapter 7 and part of chapter 4)

Other articles:

van den Broek B, Lomholt MA, **Kalisch SMJ**, Metzler R, and Wuite GJL (2008). How DNA coiling enhances target localization by proteins. *Proc Natl Acad Sci*, **105(41)**:15738–15742.

Lomholt MA, van den Broek B, **Kalisch SMJ**, Wuite GJL, and Metzler R (2009). Facilitated diffusion with dna coiling. *Proc Natl Acad Sci*, **106(20)**:8204–8208.

Acknowledgements

Doing a phd means balancing the responsibility for your own work with high dependence on others. Fortunately, AMOLF is a place with an optimal part of the "others". I have had experienced it as a friendly, helpful and open place to work in. Work discussions are motivating, fellow researchers are open to give advice, spend time and knowledge on each others projects.

It was always possible to reach staff and have an open and interested discussion how to solve a problem commonly, being it the E&I department, the workshop, the designers, the HR people. This is an extremely important and necessary basis for a good phd project. Thank you, guys!

The same applied to the lab technicians. For me help within the bio-lab was very important, coming from a physics background with very little knowledge on even how to pipet. I came with a lot of small questions and learned a great deal. For example protein purification, centrifuges, eppies, pipets, -80s, and other equipment, things inside the clean room! Thank you! Especially thanks to Roland, your valuable knowledge and creativity helped me really a lot in setting up experiments!

Of course, an important "other" is also the supervisor. Marileen, your scientific knowledge, and ability to put new results and ideas quickly into perspective was a very important ingredient for my research. What I found remarkable is your talent of motivating students. A number of times did I leave your office with new input of how to go on with my research and did I wonder, how did she manage to make it seem these ideas came all out of my own head? This ability of yours gave me, as a student, a great feeling of ability and therefore motivation to explore my topic of research further.

Finally, I want to thank my support outside AMOLF: my friends and family! You were and are essential to me and made my life happy, fulfilling and interesting!

Danke! Dank je wel! Köszönöm! Merci! Dziękuję! Obrigada! Gracias!
Спасибо! 蛋壳

Curriculum vitae

- 1980 born in Oldenburg, Germany
- 2000-2007 M.Sc. Engineering Physics
 Universität Oldenburg, Germany
- 2005-2006 Graduate research
 Physics of Life Processes group of Prof. Dr. G. Wuite
 (formerly part of Physics of Complex Systems Group)
 Vrije Universiteit, Amsterdam, The Netherlands
- 2007-2023 Ph.D. research, writing of the thesis manuscript and defense
 Bio-assembly and -organization group of Prof. Dr. Marileen Dogterom
 FOM-Institute AMOLF, Amsterdam, The Netherlands